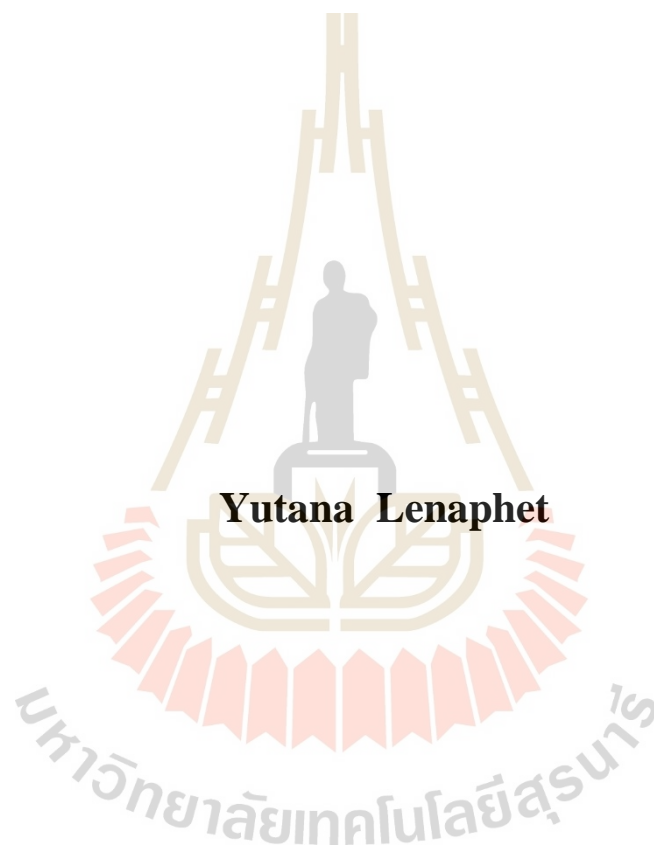


**THE IMPLEMENTATION OF THE SPECTRAL FUSING
TECHNIQUE BY USING FPGA FOR GABOR DOMAIN
OPTICAL COHERENCE MICROSCOPY (GD-OCM)**



Yutana Lenaphet

**A Thesis Submitted in Partial Fulfillment of the Requirements for the
Degree of Doctor of Engineering in Electrical Engineering**

Suranaree University of Technology

Academic Year 2020

การดำเนินการของเทคนิคการรวมสเปกตรัมโดยใช้เอฟพีจีเอ
สำหรับกล้องจุลทรรศน์ชนิดเกเบอร์



วิทยานิพนธ์นี้เป็นส่วนหนึ่งของการศึกษาตามหลักสูตรปริญญาวิศวกรรมศาสตรดุษฎีบัณฑิต
สาขาวิชาวิศวกรรมไฟฟ้า
มหาวิทยาลัยเทคโนโลยีสุรนารี
ปีการศึกษา 2563

**THE IMPLEMENTATION OF THE SPECTRAL FUSING
TECHNIQUE BY USING FPGA FOR GABOR DOMAIN
OPTICAL COHERENCE MICROSCOPY (GD-OCM)**

Suranaree University of Technology has approved this thesis submitted in partial fulfillment of the requirements for the Degree of Doctor of Philosophy.

Thesis Examining Committee



(Dr. Apichart Intarapanich)

Chairperson



(Assoc. Prof. Dr. Panomsak Meemon)

Member (Thesis Advisor)



(Prof. Dr. Joewono Widjaja)

Member



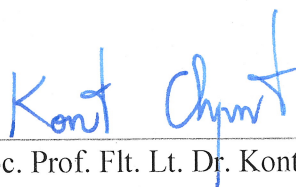
(Asst. Prof. Dr. Paramate Horkaew)

Member



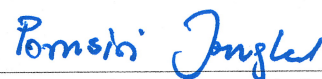
(Asst. Prof. Dr. Boonsong Sutapun)

Member



(Assoc. Prof. Ft. Lt. Dr. Kontorn Chamniprasart)

Vice Rector for Academic Affairs
and Internationalization



(Assoc. Prof. Dr. Pornsiri Jongkol)

Dean of Institute of Engineering

ยุทธนา ลีนาเพชร : การดำเนินการของเทคนิคการรวมสเปกตรัมโดยใช้เอฟพีจีเอ
สำหรับกล้องจุลทรรศน์ชนิดเคเบอร์ (THE IMPLEMENTATION OF THE SPECTRAL
FUSING TECHNIQUE BY USING FPGA FOR GABOR DOMAIN OPTICAL
COHERENCE MICROSCOPY (GD-OCM)) อาจารย์ที่ปรึกษา : รองศาสตราจารย์
ดร.พนมศักดิ์ มีมนต์, 136 หน้า.

เป็นที่ทราบกันดีว่าการถ่ายภาพความละเอียดสูงโดยใช้เลนส์ถ่ายภาพที่มีค่าโคเนรับแสง
กว้างจะทำให้ได้ความกว้างของจุดโฟกัส (Depth of focus) สั้นลง ซึ่งส่งผลให้มุมมองทางความลึก
ของการถ่ายภาพตัดขวางที่ถ่ายโดย Optical coherence tomography (OCT) สั้นลงด้วย เพื่อแก้ปัญหา
นี้ Gabor domain optical coherence microscopy (GD-OCM) หรือกล้องจุลทรรศน์ชนิดเคเบอร์ได้
ถูกพัฒนาขึ้นเพื่อรวมภาพตัดขวางที่มีความละเอียดสูงหลายๆ ภาพที่ตำแหน่งโฟกัสที่ความลึกที่
แตกต่างกันและรวมภาพให้เป็นหนึ่งภาพตัดขวางที่มีความละเอียดสูงและมีมุมมองทางความลึกของ
ภาพที่มากขึ้น แต่อย่างไรก็ตามการถ่ายภาพของกล้องจุลทรรศน์ชนิดเคเบอร์มีขั้นตอนการ
ประมวลผลภาพที่มากขึ้น เช่น การแยกโฟกัสของภาพออกจากสัญญาณรบกวนและการรวมภาพ
ส่งผลให้ใช้เวลาในการประมวลผลภาพมากกว่าการถ่ายภาพตัดขวางแบบดั้งเดิม

วิทยานิพนธ์นี้ศึกษาการดำเนินการของเทคนิคการรวมสเปกตรัมโดยใช้เอฟพีจีเอ (FPGAs)
ซึ่งเป็นหน่วยประมวลผลที่อยู่ในอุปกรณ์รับข้อมูล (Frame grabber) โดยได้ออกแบบกระบวนการ
ประมวลผลภาพทั้งหมดของการถ่ายภาพของกล้องจุลทรรศน์ชนิดเคเบอร์สามารถดำเนินการใน
อุปกรณ์รับข้อมูล เมื่อประมวลผลภาพเรียบร้อยแล้วจึงส่งภาพสุดท้ายกลับเข้าสู่คอมพิวเตอร์ โดย
เทคนิคนี้ช่วยลดปริมาณการถ่ายโอนข้อมูลระหว่างอุปกรณ์รับข้อมูลและคอมพิวเตอร์ลงได้ ซึ่ง
ผลการวิจัยพบว่าเวลาในการประมวลผลของเทคนิคการรวมสเปกตรัมโดยใช้เอฟพีจีเอสำหรับกล้อง
จุลทรรศน์ชนิดเคเบอร์ช่วยลดเวลาในการประมวลผลได้ 35% เมื่อเปรียบเทียบกับการประมวลผล
ภาพแบบดั้งเดิมของกล้องจุลทรรศน์ชนิดเคเบอร์

สาขาวิชาวิศวกรรมอิเล็กทรอนิกส์
ปีการศึกษา 2563

ลายมือชื่อนักศึกษา ยุทธนา ลีนาเพชร
ลายมือชื่ออาจารย์ที่ปรึกษา ดร.พนมศักดิ์ มีมนต์

YUTANA LENAPHET : THE IMPLEMENTATION OF THE SPECTRAL
FUSING TECHNIQUE BY USING FPGA FOR GABOR DOMAIN OPTICAL
COHERENCE MICROSCOPY (GD-OCM). THESIS ADVISOR : ASSOC.
PROF. PANOMSAK MEEMON, Ph.D., 136 PP.

OPTICAL COHERENCE TOMOGRAPHY/ GABOR DOMAIN OPTICAL
COHERENCE MICROSCOPY/ SPECTRAL FUSING / FPGA

High-resolution imaging using high numerical aperture imaging optics is commonly known to cause a narrow depth of focus, which limits the depth of field in optical coherence tomography (OCT). To achieve semi-invariant high resolution in all directions, Gabor domain optical coherence microscopy (GD-OCM) combines the in-focus regions of multiple cross-sectional images that are acquired while shifting the focal plane of the objective lens. As a result, GD-OCM requires additional processes for in-focus extraction and fusion, leading to longer processing times, as compared with conventional frequency-domain OCT (FD-OCT). In this thesis, we present the implementation of the spectral domain Gabor fusion algorithm using field-programmable gate arrays (FPGAs) in a spectral acquisition hardware device. All processes are now performed in an acquisition device as opposed to the post-processing of the original GD-OCM, which reduces the amount of data transfer between the image acquisition device and the processing host. The results showed that the total processing time for the spectral fusing GD-OCM FPGA-based was improved the processing time by 35%.

School of Electronics Engineering

Academic Year 2020

Student's Signature

ยุดานา เลนัพเพต

Advisor's Signature

Assoc. Prof. Panomsak Meemon

ACKNOWLEDGEMENT

I would like to express my sincere gratitude to my advisor, Assoc. Prof. Dr. Panomsak Meemon for the continuous support of my Ph.D. study and research. I am most grateful for his patience, motivation, and knowledge. His guidance helped me in all the time of research and writing of this thesis.

I would like to thank the rest of my thesis committee: Dr. Apichart Intarapanich, Prof. Dr. Joewono Widjaja, Asst. Prof. Dr. Paramate Horkaew, and Asst. Prof. Dr. Boonsong Sutapun, for their insightful comments, encouragement, and hard questions that give me a better understanding of my work.

I would also like to thank members of all LASER Laboratory for suggestions and all their help in many problems throughout this research, especially Jiraporn Sanjae, Jadsada Saetiew, and Kunakorn Palawong.

Finally, I most gratefully acknowledge my parents and my friends for all their support throughout the period of this research. I would not have achieved this far and this thesis would not have been completed without all the support that I have always received from them.

Yutana Lenaphet

TABLE OF CONTENTS

	Page
ABSTRACT (THAI)	I
ABSTRACT (ENGLISH)	II
ACKNOWLEDGEMENT	III
TABLE OF CONTENTS	IV
LIST OF TABLES	VII
LIST OF FIGURES	VIII
CHAPTER	
I INTRODUCTION	1
1.1 Background of GD-OCM	1
1.2 Background of field-programmable gate arrays.....	9
1.3 Significance of the study.....	12
1.4 Research objectives	13
1.5 Scope.....	13
II THEORY	15
2.1 Optical coherence tomography (OCT).....	15
2.2 Mathematical description	16
2.2.1 FD-OCT signal.....	16
2.2.2 GD-OCM signal	23
2.2.3 SF-GD-OCM signal	30

TABLE OF CONTENT (Continued)

	Page
2.3 Digital filters.....	31
2.3.1 Mathematical equation of filters	33
2.3.2 Sampling frequency.....	34
2.3.3 Design methods of IIR filters.....	36
2.4 Implementation of Digital filters on FPGA.....	37
2.4.1 FIR Filter Structure	37
2.4.2 IIR Filter Structure	37
2.5 Fixed-Point Implementation.....	39
III METHODS	43
3.1 SF-GD-OCM System setup.....	43
3.2 Design of the precision scanning system	46
3.3 Linear wavenumber interpolation.....	50
3.3.1 Creating a linear wavenumber (k_i)	52
3.3.2 Implementation of linear wavenumber interpolation.....	53
3.4 Spectral filtering	54
3.4.1 The relation of applied voltage and shifting of the focal planes	55
3.4.2 Finding cut-off frequency for spectral filtering	58

TABLE OF CONTENT (Continued)

	Page
3.4.3 Designing of spectral filter	60
3.4.4 Implementation of spectral filter on FPGA	61
3.5 Spectral fusing	63
3.6 Fast Fourier transform.....	64
3.7 Performance of FPGA-based SF-GD-OCM.....	64
IV RESULTS AND DISCUSSION.....	70
4.1 Calibration of the scanning system.....	70
4.2 Linear wavenumber interpolation.....	75
4.2 Spectral filtering	77
4.3 Spectral fusing	80
4.4 Fast Fourier transform.....	90
4.5 Performance of FPGA-based SF-GD-OCM system	93
V CONCLUSION.....	99
REFERENCES.....	103
APPENDIX I.....	109
BIOGRAPHY	136

LIST OF TABLES

Table		Page
1.1	Comparing the later resolution, DOF, the amount of acquired data, and processing time of OCT, OCM and GD-OCM.	8
3.1	Example of the filter specification for zone 1	60
4.1	Comparison of depth cross-sectional images of a tadpole at five different focus positions after performing different filters order of the digital bandpass filter.	87
4.2	Comparison of an image quality index, throughput, and the resource usage of the FPGA of the fused image obtained by FPGA-based SF-GD-OCM with different filter orders.	88
4.3	Comparison of the processing times between FPGA-based SF-GD-OCM and CPU-based SF-GD-OCM in each process per spectrum.	90
4.4	Summary of the usage of FPGA resources in each process of the FPGA-based SF-GD-OCM.	91
4.5	Comparison of the processing times between FPGA-based SF-GD-OCM and vary number of core processing of CPU-based SF-GD-OCM in each process per spectrum	92
4.6	Comparison of the processing times between FPGA-based SF-GD-OCM and vary the amount of RAM of CPU-based SF-GD-OCM in each process per spectrum.	92
4.7	The measured DOF of each focusing zone.	93

LIST OF FIGURES

Figure		Page
1.1	Schematic shows relation of lateral resolution, axial resolution, and depth of focus with (a) low NA and (b) high NA of the objective lens.	4
1.2	Schematic shows comparison DOF of OCT, OCM and GD-OCM.	7
1.3	Schematic shows non-invasive imaging technologies.	7
1.4	The architectural layout of FPGA; CLB = configurable logic blocks,	11
1.5	Comparison of flow diagrams of (a) CPU-based spectral fusing GD-OCM and (b) FPGA-based spectral fusing GD-OCM.	12
2.1	Schematic of Michelson interferometer.	16
2.2	Illustration of the sample reflectivity along depth.	21
2.3	Schematic shows the even symmetric function of the sample reflectivity. $r_s(l_D)$ is the real reflectivity profile of the sample. $r_s(-l_D)$ is a mirror image caused by complex conjugate of the Fourier transform of a real function.	22
2.4	Schematic shows that an axial point spread function is the inverse Fourier transform of the power spectral density of the light source.	22
2.5	Schematic shows that creating the resolved depth profile is the convolution between an axial point spread function and the sample reflectivity.	23

LIST OF FIGURES (Continued)

Figure	Page
2.6 Schematic shows (a) the sample reflectivity along the depth, (b) a Gabor windows function along the depth centered at ls_0 as a result of DOF, and (c) the sample reflectivity that is governed by Gabor windows function that is the effect of a high NA of objective lens.....	25
2.7 Schematic diagram shows (a) the sample reflectivity of the sample as the homogenous multi-layered materials as the infinite delta function along the sample depth, (b-e) the convolution between an axial point spread function and the sample reflectivity as shifting of the Gabor window, (f-i) the resolved depth profile when $m = 0$ is not shifting and $m = 1,2,3$ are representing the number of shifting, (j) the full depth profile of the sample reflectivity for GD-fusion in spatial domain.....	29
2.8 Shows the ideal frequency response of (a) lowpass filters, (b) highpass filters, (c) bandpass filters, and (d) stopband filters, where f_c = cut-off frequency.....	32
2.9 The practical frequency response of bandpass filters. The vertical represents filter gain in log scale and the horizontal represents frequency in Hz unit.....	33

LIST OF FIGURES (Continued)

Figure	Page
2.10	The interference signal represented by the discrete of samples in (a) time domain and (b) frequency domain. N_{pixel} = the number of pixels of the camera line sensor as known as the number of samples in time domain, FFT = fast Fourier transform, f_s = sampling frequency, N_{FFT} = the number of samples in frequency domain. 36
2.11	FIR Filter representation in simple structure..... 37
2.12	IIR structure of (a) Direct form I and (b)Transpose Direct form I. 38
2.13	IIR structure of (a) Direct form II and (b) Transpose Direct form II..... 39
2.14	A cascaded stage structure of IIR structure..... 39
2.15	Schematic diagram shows the fixed-point representation..... 40
2.16	The range and resolution of (a) unsigned and (b) signed fixed point number by using LabVIEW programming. 41
3.1	A schematic diagram of (a) setup and (b) the photograph of the FPGA -based SF-GD-OCM system; MO=microscope objective, GV= galvanometer mirror, LL=liquid lens, BS=beam splitter, CL=collimator, RTF=retro reflector..... 45
3.2	A schematic shows the trigger and scanning system controlled by NI myRIO. (a) The main clock for camera trigger and x-axis trigger, (b) camera controlling, (c) the x-axis and (d) the y-axis scan controlling of galvanometer mirror, respectively. 47
3.3	A schematic shows 3D scanning system. 49

LIST OF FIGURES (Continued)

Figure	Page
<p>3.4 Illustrates the relation of (a) an unknown point (X, Y) with two known points (X_1, Y_1) and (X_2, Y_2) on the same straight line and (b) an unknown point (ki, Iki) with two known points (kn, Ikn) and $(kn + 1, Ikn + 1)$ which be a part of the spectral interference signal assume as a straight line.....</p>	51
<p>3.5 A flow diagram of the implementation of linear wavenumber interpolation.....</p>	54
<p>3.6 A schematic diagram of shifting focal planes; MO=microscope objective, GV=galvanometer mirror , BS=beam splitter, CL=collimator, RTF=retro reflector.....</p>	55
<p>3.7 Shows superposition of multiple depth profiles obtained at different positions in air of the sample in pixels in range of 350-510 where N_{FFT} is 4096 where covered by (a) Gabor windows 1, (b) Gabor window 2, (c) Gabor windows 3, and (d) represents superposition of (a-c).....</p>	57
<p>3.8 Shows superposition of multiple depth profiles obtained at different positions in air of the sample in MHz which indicate cut-off frequency as (a) f_{c1} and f_{c2} for zone 1, (b) f_{c3} and f_{c4} for zone 2, (c) f_{c5} and f_{c6} for zone 3.....</p>	59

LIST OF FIGURES (Continued)

Figure	Page
3.9	Shows implementation of the 10 th order of bandpass filter of Chebyshev type I with cascaded second order section form II structure. 61
3.10	A flow diagram of the spectral filtering process of GD-OCM FPGA-based. 62
3.11	A flow diagram of the spectral fusing process with parallel summation of filtered spectral. 63
3.12	Shows the relation between the position of amplitude in pixel and the translation distance of the mirror sample measured in micrometer. 65
3.13	An example of the fringe frequency at difference OPD (a-c) that corresponding to applied voltage of liquid lens driver, 30V, 43V, and 45V, respectively. (d) shows the superposition of multiple depth profiles obtained at different focus depth positions with 1 voltage apart in air of the mirror sample measured in micrometers. 66
3.14	Example of (a) the zoom in from the red dashed box in Figure 3.13(d) and (b) <i>en-face</i> view of a standard USAF 1951 target of focus position at 30V. 67

LIST OF FIGURES (Continued)

Figure	Page
3.15	Shows (a) superposition of multiple depth profiles obtained at different positions in air of the sample in micrometer, (b) result of Gaussian fitting plotted over (a), (c) Gabor windows at normal focal plane (43.12V to liquid lens driver) that corresponding to the center and width of DOF of zone 1. 69
4.1	(a) Picture of resolution target from the FPGA-based spectral fusing GD-OCM and (b) table resolution values for standard..... 71
4.2	(a) and (b) are picture of resolution target from the FPGA-based spectral fusing GD-OCM, (c) the intensity profile of x direction, and (d) the intensity profile of y direction..... 72
4.3	A flow diagram of the implementation of the FPGA-based spectral fusing GD-OCM with the seven focus zones; BPF=the digital bandpass filter, BRAM=blocks of random-access memory..... 74
4.4	Shows a cross-sectional image of a stack of polymeric tapes (a) without and (b) with performing linear wavenumber interpolation. (c) and (d) are represent an average depth profile of (a) and (b), respectively..... 76
4.5	Shows a cross-sectional image of a stack of polymeric tapes at different focus position over the same cross-section field-of-view, (a) before and (b) after performing the digital bandpass filter. BPF=the digital bandpass filter. 78

LIST OF FIGURES (Continued)

Figure	Page
4.6 Shows an average depth profile of a stack of polymeric tapes at different focus position in frequencies, (a-g) before and (h-n) after performing the digital bandpass filter. BPF=the digital bandpass filter.....	79
4.7 Shows overlaid plots of the logarithmic-scale average intensity profile along the depth of the seven focus zones, (a) without and (b) with performing the digital bandpass filter. The logarithmic-scale intensity profile obtained by FFT of the fused spectrum (c) without and (d) with performing the digital bandpass filter. Cross-sectional images of the fused image (e) without and (f) with performing the digital bandpass filter.	81
4.8 Shows overlaid plots of the logarithmic-scale average intensity profile along the depth of the seven focus zones, (a) spatial fusing domain and (b) spectral fusing domain. The logarithmic-scale intensity profile obtained by FFT of the fused spectrum in (c) spatial fusing domain and (d) spectral fusing domain. Cross-sectional images of the fused image in (e) spatial fusing domain and (f) spectral fusing domain.	83

LIST OF FIGURES (Continued)

Figure	Page
4.9 Volumetric rendering of the 3D fused data acquired by the developed SF-GD-OCM: (a) without and (b) with the application of the digital bandpass filter. (a1-a3) and (b1-b3) are <i>en face</i> images reconstructed at different depth locations from the 3D data sets in (a) and (b), respectively. (c) Volumetric rendering of the 3D fused data acquired by the spatial fusing GD-OCM. (c1-c3) are <i>en face</i> images reconstructed at different depth locations from the 3D data sets in (c).....	84
4.10 (a-d) An example of depth cross-sectional image of finger's nail fold at different focus positions, (e) the fused image of finger's nail fold from (a-d) that is performed by GD-OCM FPGA-based imaging.....	85
4.11 Shows the quality image index of the fused image of a tadpole with (a) a perfect fused image, (b) the fused image without applying the digital bandpass filter, (c-g) the fused image after applying the digital bandpass filter of the 10 th , 8 th , 6 th , 4 th , and 2 nd , order filter respectively.....	89

LIST OF FIGURES (Continued)

Figure	Page
4.12 Plot of the lateral resolution in (a) the x direction and (b) the y direction, (c) the axial resolution, and, (d) plot of the DOF measured at difference focus depth location by vary of applied voltage to liquid lens driver of the FPGA-based spectral fusing GD-OCM without performing adaptive linear wavenumber interpolation.....	95
4.13 Plot of the lateral resolution in (a) the x direction and (b) the y direction, (c) the axial resolution, and, (d) plot of the DOF measured at difference focus depth location by vary of applied voltage to liquid lens driver of the FPGA-based spectral fusing GD-OCM with performing adaptive linear wavenumber interpolation.....	96
4.14 Comparison of the axial resolution of the FPGA-based spectral fusing GD-OCM without and with performing adaptive linear wavenumber interpolation is shown as the orange triangle and the blue circle, respectively.	97
4.15 Shows the FPGA-based spectral fusing GD-OCM imaging of a cross- sectional image of a stack of polymeric tapes (a) without and (b) with performing adaptive linear wavenumber interpolation.	97
4.16 Example of biological sample at cellular level cell, the field of view is 1 mm x 1 mm of (a) onion cell and (b) trunk cell of Peperomia pellucida by our system.....	98

CHAPTER I

INTRODUCTION

1.1 Background of GD-OCM

Optical imaging technology allows for non-invasive imaging of biological tissues and organs at micrometer level resolution. It is helpful to understand and monitor the internal microstructure of the biological sample *in vivo*. Optical coherence tomography (OCT) is an optical imaging technology for non-aggressive cross-sectional imaging of biological samples (Huang et al., 1991). OCT imaging principle is analogous to ultrasound imaging. However, ultrasound imaging uses ultrasonic waves, while OCT imaging uses infrared light to acquire the sample information. OCT fills the resolution gap between microscopy and ultrasound imaging. OCT can perform high-resolution, high-speed three-dimensional imaging of biological samples in real-time. Time-domain optical coherence tomography (TD-OCT) detects echo time delays of back-reflected and backscattered light by measuring the interference signal as a function of delayed time at each position of a lateral probe beam. Frequency-domain optical coherence tomography (FD-OCT) detects the interference signal as a function of wavelength instead of mechanical scanning (Watanabe, Maeno, Aoshima, Hasegawa, & Koseki, 2010). FD-OCT obtains the entire depth profile by Fourier transform of a spectral interference signal at each position of a lateral scanning. FD-OCT system achieves improvement in sensitivity, imaging speed, and signal-to-noise ratio because there is no scanning of the reference mirror as compared with TD-OCT systems (de Boer et al., 2003; Drexler et al., 2014; Leitgeb, Hitzenberger, & Fercher,

2003). Typically, OCT system uses a broadband light source with a near-infrared wavelength in the range of 800-1300 nm to avoid absorptions of blood and water, which are the main components of most biological samples. Furthermore, the longer wavelengths penetrate deeper into the sample but the axial resolution will be worse than that of the shorter wavelengths with the same spectral bandwidth (Bouma & Tearney, 2002).

The axial resolution and lateral resolution of OCT are independent. Assuming that the spectrum of the light source has Gaussian distribution, the axial resolution is inversely proportional with the width of the power spectrum (Bouma & Tearney, 2002), which can be expressed as

$$\Delta z = \frac{2 \ln 2}{\pi} \left(\frac{\lambda_0^2}{\Delta \lambda} \right), \quad (1.1)$$

where Δz is an axial resolution that can be measured by the full width at half-maximum of the coherence of the light source, λ_0 is the center wavelength of the light source, and $\Delta \lambda$ is the full width at half-maximum of the power spectrum of the light source. The axial resolution can be improved by increase the bandwidth of light sources.

On the other hand, the lateral resolution of OCT is determined by the spot size of the imaging beam. The lateral resolution can be estimated by the Rayleigh resolution criterion (Bouma & Tearney, 2002)

$$\Delta x = 1.22 \frac{\lambda_0}{2NA}, \quad (1.2)$$

where Δx is lateral resolution, NA is a numerical aperture of the objective lens, which can be calculated by half of the lens diameter (D) divided by focal length (f). Substituting NA in terms of diameter and focal length, the lateral resolution can be rewritten as

$$\Delta x = 1.22\lambda_0 \frac{f}{D} . \quad (1.3)$$

Hence, the lateral resolution of OCT can be improved by increasing the numerical aperture (NA) of the objective lens.

Typically, OCT uses a low NA of the objective lens (i.e., ~ 0.04), which provides a lateral resolution of about 10-30 μm over a 2-3 mm depth range under the surface of the biological sample. For cellular and sub-cellular biological samples, confocal microscopy normally uses a high NA of the objective lens (i.e., >0.5). Confocal microscopy obtains a lateral resolution of about 180 nm and imaging depth of about 500 nm (Fouquet et al., 2015). Optical coherence microscopy (OCM) is a combination of confocal microscopy and OCT. OCM was demonstrated to enhance imaging depth when compared with confocal microscopy. OCM used NA of about 0.4, which provides imaging depth up to three times longer than that of confocal microscopy (i.e., several hundred micrometers) (Izatt, Hee, Owen, Swanson, & Fujimoto, 1994). However, OCM provides better lateral imaging resolution at the expense of shorter depth of focus as compared with conventional OCT.

The depth of focus (DOF) of a spherical lens is defined by two times of the Rayleigh range (Δz_R) (Bouma & Tearney, 2002) and can be expressed in terms of lateral resolution (Δx) or the wavelength (λ) and NA of the optics as

$$DOF = 2\Delta z_R, \quad (1.4)$$

$$DOF = \frac{\pi\Delta x^2}{2\lambda}, \quad (1.5)$$

$$DOF = \frac{\lambda_0}{2(NA)^2}. \quad (1.6)$$

As considered from Eq. (1.2) and Eq. (1.6), the lateral resolution is proportional to NA^{-1} , while the DOF is proportional to NA^{-2} (Aguirre, Hsiung, Ko, Hartl, & Fujimoto, 2003). Therefore, increasing NA leads to higher lateral resolution but shorter range of the depth of focus as shown in Figure 1.1. Figure 1.1(a) illustrates the long DOF at a low lateral resolution of a low NA objective lens and Figure 1.1(b) illustrates the short DOF at a high lateral resolution of a high NA objective lens.

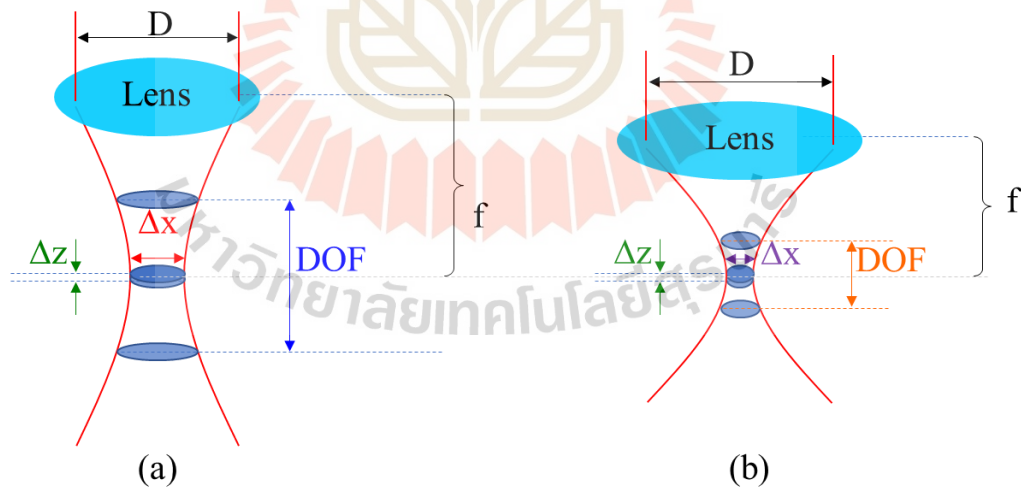


Figure 1.1 Schematic shows the relation of lateral resolution, axial resolution, and depth of focus with (a) low NA and (b) high NA of the objective lens.

To obtain a large three-dimensional OCT at extended imaging depth ranges with high resolution on both axial and lateral directions, C-mode scanning and zone focusing have been demonstrated (Huber, Wojtkowski, Fujimoto, Jiang, & Cable, 2005). C-mode scanning and zone focusing axially translate the focal plane of an objective lens across the depth of the sample. Therefore, a large three-dimensional OCT can be reconstructed from multiple three-dimensional OCT data sets obtained at each focus position. However, this technique required an axial translation of either an objective lens or the sample. To remedy this issue, several techniques of dynamic focus without a moving part were investigated and reported, such as a dynamic focus control system based on a microelectromechanical mirror (Qi et al., 2004), a dynamic focus shifting by using a liquid lens embedded in a custom-designed objective lens (Murali, Lee, & Rolland, 2007), a focus-stacking with automatic focus optimization by inserting a liquid lens in the sample arm (Cua et al., 2016).

Interferometric synthetic aperture microscopy (Ralston, Marks, Carney, & Boppart, 2007) and computational adaptive optics (Adie, Graf, Ahmad, Carney, & Boppart, 2012) have been reported as computational methods to improve the lateral resolution and enhance imaging by reducing aberrations and enhance the signal. However, these computational methods are sensitive to motion noise. Therefore, the achieved imaging depth is not more than 1 mm. Moreover, these computational methods must be adjusted the coefficient manually for each sample to reduce aberration. Therefore, it is inconvenient to analyze a wide variety of samples in real-time.

The trade-off between the lateral resolution and the depth of focus can be solved by dynamically refocusing along the axial direction as previously explained above.

Gabor-domain optical coherence microscopy (GD-OCM) can provide $2\ \mu\text{m}$ invariant lateral resolution across $8\ \text{mm}^3$ cubic volume with no moving part (Canavesi & Rolland, 2019; Meemon, Murali, Lee, & Rolland, 2008; J. Rolland, P. Meemon, S. Murali, K. Thompson, & K. Lee, 2010; Rolland et al., 2009; J. P. Rolland, P. Meemon, S. Murali, K. P. Thompson, & K.-s. Lee, 2010). GD-OCM is a combination of OCM technique and dynamic focus with an automatic data fusion method that can improve lateral resolution and capable of real-time refocusing into the depth of the sample in different depth ranges. Each range or zone is defined by the depth of focus, which is determined by the NA of an imaging lens. GD-OCM is capable of visualizing *in vivo* cellular-level sample (Canavesi et al., 2020; Canavesi & Rolland, 2019; K.-S. Lee, Thompson, Meemon, & Rolland, 2011).

In GD-OCM, Fourier transformation was performed on each zone of interference spectra to obtain a depth cross-sectional image of the zone. Gabor-based filtering was applied to extract only in-focus information of each image zone. The filtered zones were then fused into one depth scan that contains only in-focus information across a long range of imaging depth. This processing algorithm is called the spatial-domain Gabor fusion technique. Nevertheless, GD-OCM requires more Fourier transforms as compared to a conventional FD-OCT, which results in longer processing times. Figure 1.2 shows an example of GD-OCM for three focus shifts to achieve the depth of images equivalent to that of conventional OCT, while the lateral resolution is comparable to that of OCM. However, a conventional OCT and OCM need only one Fourier transform for each depth scan, while GD-OCM requires three times Fourier transform to produce a cross-sectional image. Therefore, the processing time is three times longer than a conventional OCT.

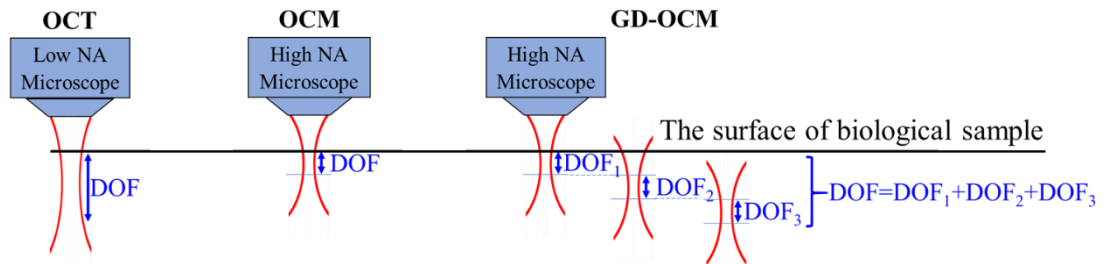


Figure 1.2 Schematic diagram shows a comparison of DOF of OCT, OCM, and GD-OCM (Lenaphet & Meemon, 2020).

All non-invasive imaging technologies face a trade-off between the lateral resolution and an image depth, as shown in Figure 1.3. GD-OCM has filled the resolution gap between OCM and OCT. GD-OCM provides the lateral resolution that is comparable to OCM and an image depth that is comparable to OCT. The main parameters of OCT, OCM, and GD-OCM are shown in Table 1.

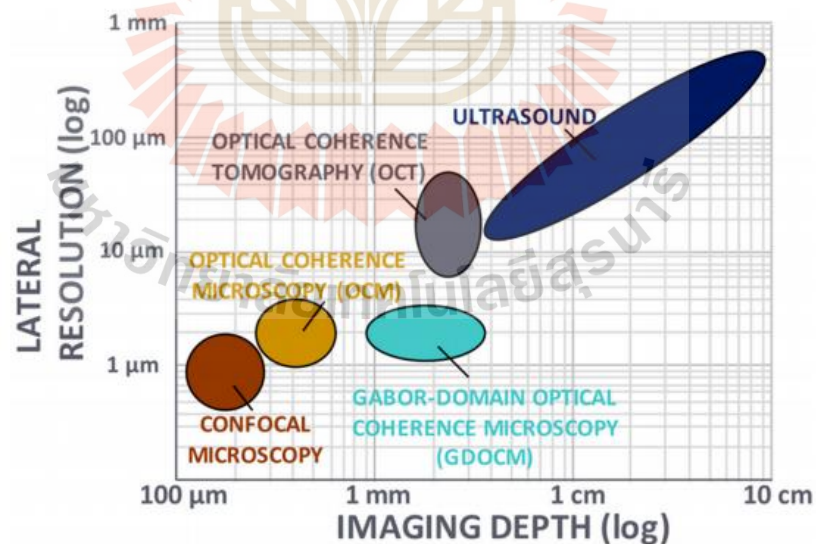


Figure 1.3 Schematic diagram shows a trade-off between lateral resolution and imaging depth of non-invasive imaging technologies. (Canavesi & Rolland, 2019).

Table 1.1 Comparison of the lateral resolution, DOF, the amount of acquired data, and processing time of OCT, OCM, and GD-OCM.

	OCT	OCM	GD-OCM
The lateral resolution (μm)	~10-30	~1-3	~1-3
The depth of focus (DOF)	2-3 mm	$\leq 300 \mu\text{m}$	Up to 2 mm
The amount of acquired data (data set)	1	1	3 or more
Processing time	fast	fast	slow

From Table 1, the original GD-OCM required 3 or more data set to perform Gabor-based filtering, fusion process, and Fourier transformation to obtain a cross-sectional image. Therefore, GD-OCM leads to a longer signal processing time as compared with OCT and OCM.

To improve the signal processing speed of GD-OCM, spectral fusing Gabor domain optical coherence microscopy (SF-GD-OCM) had been demonstrated (Meemon, Widjaja, & Rolland, 2016). SF-GD-OCM performs bandpass filters on spectral interferences of each image zone. Filtered spectra are fused into one spectrum and then Fourier transformation is performed. The main advantage of the spectral-domain fusing technique for GD-OCM over spatial-domain fusion technique is that only one Fourier transformation per one depth scan is required, which improved imaging speed as compared with multiple Fourier transformation per one depth scan in the conventional GD-OCM, while maintaining high lateral resolution. SF-GD-OCM was executed by using multi-core central processing units (CPUs) called CPU-based SF-GD-OCM. CPU-based SF-GD-OCM has improved imaging speed two times faster

as compared with the original GD-OCM. However, the processing time was still much slower than that of the conventional FD-OCT because it still takes time to filter as known as the Gabor-based filtering process that is required on the spectral interferences of each image zone.

One solution to further improve the processing speed of SF-GD-OCM is by utilizing hardware-based signal processing. Graphic processing units (GPUs) have been implemented and reported to accelerate the processing speed of FD-OCT (Borkovkina, Camino, Janpongsri, Sarunic, & Jian, 2020; Cua et al., 2016). Besides, GD-OCM with spatial-domain fusion also accelerated its signal processing by GPUs (Cogliati et al., 2016; Tankam et al., 2015). However, overall processing speeds of these techniques are limited by the speed of data transfer between the CPUs and GPUs.

One possible implementation of hardware-based signal processing in SF-GD-OCM is field-programmable gate arrays (FPGAs). FD-OCT system accelerated processing time by FPGA had been implemented and reported (Li, Sarunic, & Shannon, 2011; Ustun, Iftimia, Ferguson, & Hammer, 2008). As the SF-GD-OCM required three or more datasets of spectral interference signal as captured by the camera line sensor, in-line processing, and parallel processing is demanded. Hence, the FPGA is suited to accelerate for SF-GD-OCM system. In this study, we have investigated the implementation of SF-GD-OCM using an FPGA frame-grabber device.

1.2 Background of field-programmable gate arrays

Field-programmable gate arrays (FPGAs) is a hardware-based processor, which can implement digital signal processing algorithms directly into integrated circuits. The small basic elements are the look-up table (LUT) that performs the logic operation and

flip-flops (FF) that are shift register elements for storing the stage or result of LUT. FPGA consists of a large array of configurable logic blocks (CLBs) or called slices or logic cells, which contain LUT and FF. The modern FPGA contains DSP48s that is prebuilt multiplier-accumulate circuitry that is useful for digital signal processing applications and block random access memory (BRAM) that is useful for storing datasets or passing values between parallel tasks (Mahotra, 2010; Sundararajan, 2010). An example of an architectural layout of the basic elements of an FPGA processor is shown in Figure 1.4. In traditional programming of FPGAs, developers are required to use hardware description languages (HDL), such as VHDL or Verilog, for programming, which are low-level. Therefore, FPGA takes time to develop the program. Recently, high-level synthesis (HLS) has been developed for FPGA programming. For example, NI LabVIEW software can be converted graphical block diagrams into digital hardware circuitry. HLS helps save time and is comfortable for designing and programming.

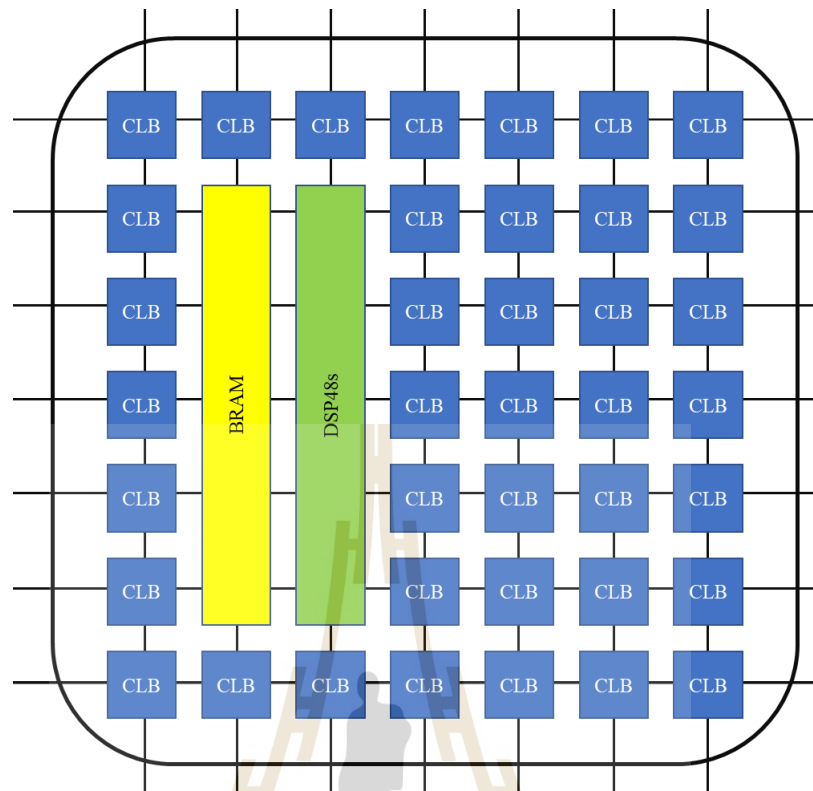


Figure 1.4 The architectural layout of FPGA; CLB = configurable logic blocks, BRAM = block random access memory, DSP48s = multiplier-accumulator circuitry.

The advantage of the FPGA is the capability to implement digital signal processing algorithm logics directly into an integrated circuit. Thus, it provides speed, reliability, and processing better than executing on processor-based systems via application software, which causes more latency between algorithms. Moreover, FPGA can execute both in-line and parallel processing algorithm. Figure 1.5(a) and (b) show a flow diagram of CPU-based SF-GD-OCM and FPGA-based SF-GD-OCM, respectively.

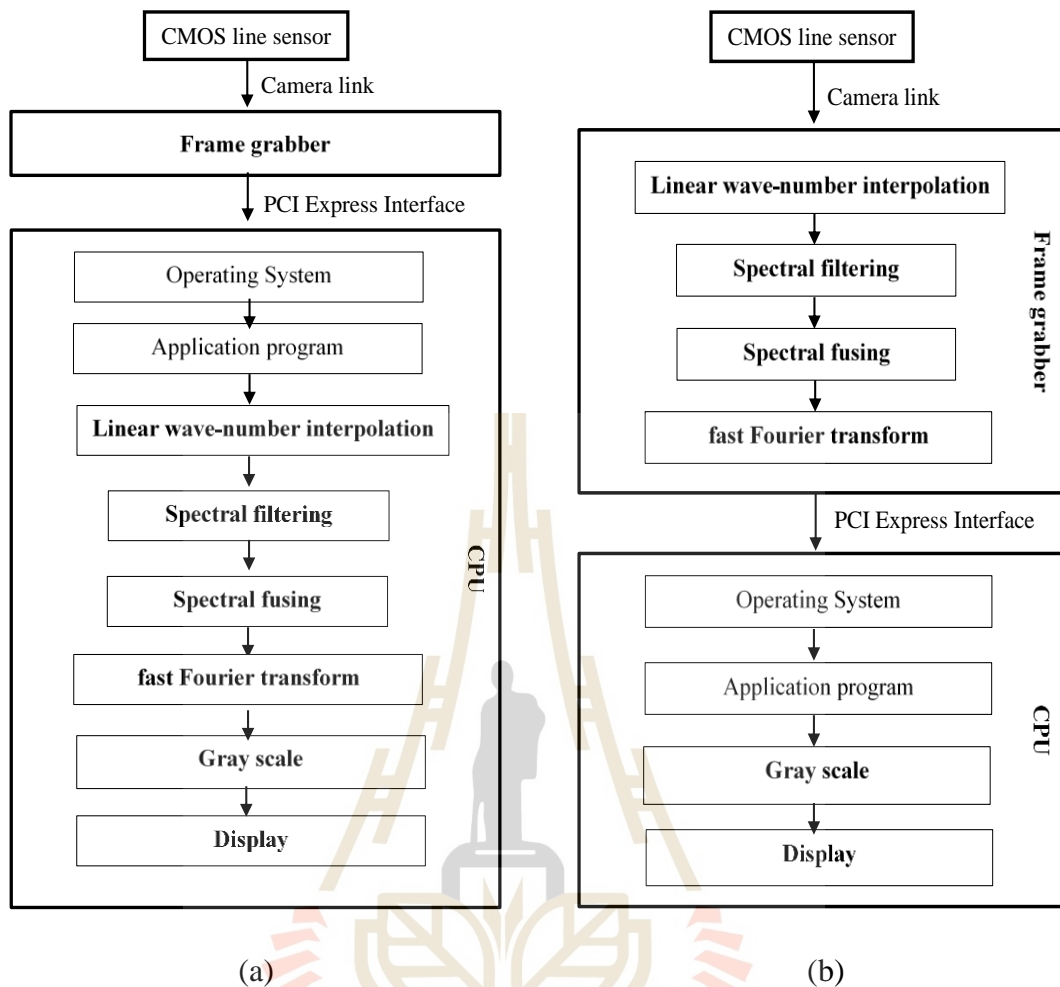


Figure 1.5 Comparison of flow diagrams of (a) CPU-based spectral fusing GD-OCM and (b) FPGA-based spectral fusing GD-OCM (Meemon, Lenaphet, & Saetiew, 2020).

1.3 Significance of the study

CPU-based SF-GD-OCM as shown in Figure 1.5(a) causes more latency between algorithms. CPU-based SF-GD-OCM executes a sequence of signal processing and can not display images in realtime. GPU is suitable for post-processing such as that in the spatial fusing GD-OCM. However, there is an issue of data transfer

speed between CPU and GPU. Therefore, it is not suitable for spectral fusing GD-OCM since all raw spectrum must be transferred to GPU memory. The spectral fusing GD-OCM in the FPGA frame grabber device is expected to address the bottleneck issue of data transferring speed between CPU and GPU, reduce the amount of data transfer between the frame grabber and the host computer, and reduce the amount of data needed to be held by the host computer.

The FPGA-based spectral fusing GD-OCM could open a path for high-speed imaging of SF-GD-OCM, which will be useful for imaging biological samples at cellular level resolution in real-time. Furthermore, this capability will allow the implementation of the FPGA-based spectral fusing GD-OCM with lower specification and cost for the host computer.

1.4 Research objectives

1.4.1 To develop a spectral fusing technique for GD-OCM by using an FPGA frame grabber device to improve the signal processing speed of GD-OCM.

1.4.2 To design and construct the laboratory prototype of GD-OCM to verify the performance and speed of the spectral fusing technique by using an FPGA frame grabber device.

1.5 Scope

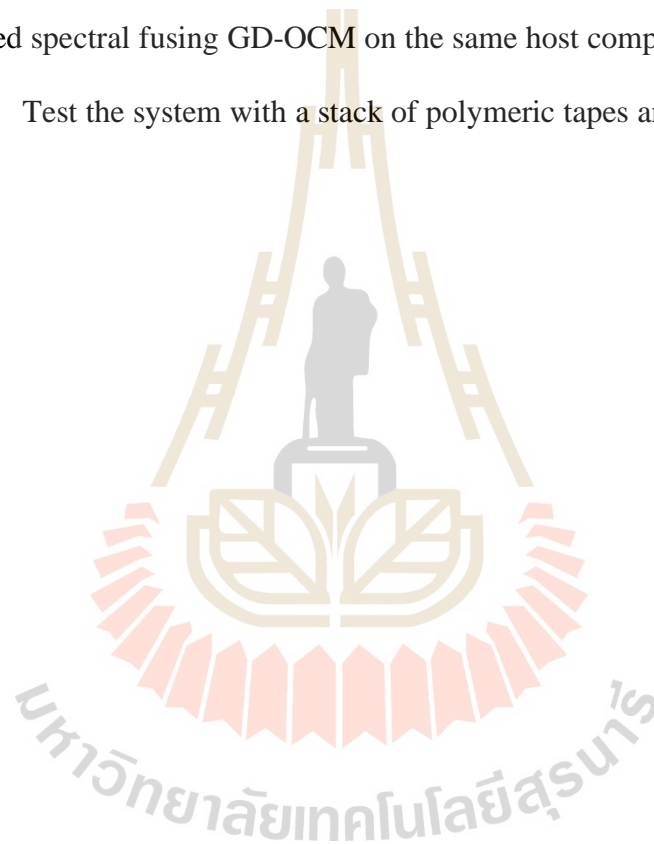
1.5.1 Design and construct the spectral fusing GD-OCM system in laboratory using a broadband light source at around 840 nm central wavelength, and using liquid lens for shifting focal plane.

1.5.2 Develop spectral fusing technique for SF-GD-OCM by using FPGA in NI LabVIEW RIO Evaluation Kit (SB-RIO 9637) for data acquisition, filtering, and signal processing.

1.5.3 Program FPGA frame grabber by LabVIEW programming.

1.5.4 Verify the performance and speed of the FPGA-based spectral fusing GD-OCM by using the FPGA frame grabber device (PCIe-1473R) as compared with the CPU-based spectral fusing GD-OCM on the same host computer.

1.5.5 Test the system with a stack of polymeric tapes and biological samples.



CHAPTER II

THEORY

2.1 Optical coherence tomography (OCT)

OCT system is based on the Michelson interferometer. A broadband light source is split by a beam splitter into the sample and the reference arms as shown in Figure 2.1. The light intensity reflected from the sample and the reference mirror is then captured by a detector. In time-domain OCT (TD-OCT), the interference signal is obtained by scanning the reference mirror to match the optical path length of the reflections from the sample. The interference signal is demodulated to generate a reflectivity depth profile as a function of times. In frequency-domain OCT (FD-OCT), the interference signal is captured as a function of wavelength. FD-OCT can be divided into two main different approaches, which depend on the light source. The first approach is spectrometer-based FD-OCT, in which the sample is illuminated by a broadband light beam and detected by a linear array detector. The second approach is swept-source-based FD-OCT (SS-OCT), in which the sample is illuminated by a broadband frequency-swept light source and a single photodetector is used to record the time-encoded spectral interference signal.

Typically, SS-OCT systems used the high-speed frequency swept light source and required the high-performance analog to digital converter module, which leads to high cost when compared to spectrometer-based FD-OCT systems. The main improvement of FD-OCT over TD-OCT is that a full depth profile can be immediately achieved by an inverse Fourier transformation of a single acquired spectral interference

signal without the scanning of the reference mirror as required in TD-OCT (de Boer et al., 2003; Drexler et al., 2014; Leitgeb et al., 2003). Furthermore, the improvement of the detector, i.e. charge-coupled device (CCD) or complementary metal-oxide-semiconductor (CMOS) cameras, which is a multi-element array detector, leads to the improvement in the imaging speed and the signal to noise ratio.

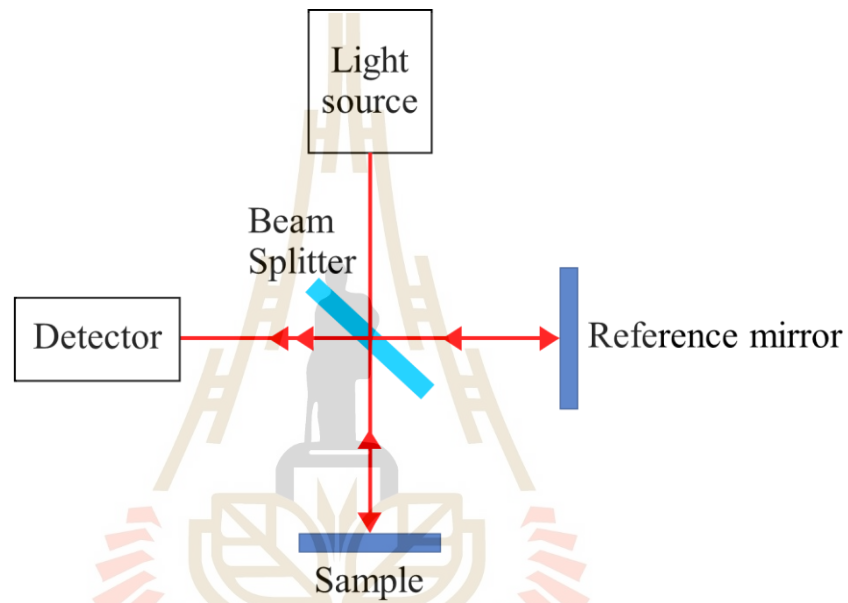


Figure 2.1 Schematic diagram of Michelson interferometer.

2.2 Mathematical description

2.2.1 FD-OCT signal

Considering the spectrometer-based FD-OCT systems, the spectral intensity detected by the camera line sensor of an interferometer can be expressed as

$$\hat{I}_D(k) = |\hat{E}_R(k) + \hat{E}_S(k)|^2, \quad (2.1)$$

where the caret symbol denotes a function in the spectral domain, $\hat{E}_R(k)$ is the spectral electric field propagating through the reference arm, and $\hat{E}_S(k)$ is the spectral electric field that is backscattered from the sample through the sample arm. $\hat{E}_R(k)$ can be defined as

$$\hat{E}_R(k) = K_R r_R \hat{E}_{R0}(k) e^{jk l_R}, \quad (2.2)$$

where $k = \frac{2\pi}{\lambda}$ is the wave propagation number, K_R is a real number of total losses in the reference arm, r_R is the reflectivity of the reference reflecting element, $\hat{E}_{R0}(k)$ is the spectral electric field amplitude in the reference arm after propagating through the beam splitter, and l_R is a round-trip propagation distance along the reference arm. $\hat{E}_S(k)$ is a collection of the reflected electric field at different locations along the beam path and can be defined as

$$\hat{E}_S(k) = K_S \hat{E}_{S0}(k) \int_{-\infty}^{+\infty} r_S(l_S) e^{jkl_S} dl_S, \quad (2.3)$$

where K_S is a real number of total losses along in the sample arm, $\hat{E}_{S0}(k)$ is the spectral electric field amplitude in the sample arm after through the beam splitter, l_S is a round-trip propagation distance along the sample arm, and $r_S(l_S)$ is the sample reflectivity profile along the depth as a function of l_S (L. Wang & Wu, 2007). Hence, the spectral intensity from Eq. (2.1) can be rewritten as

$$\hat{I}_D(k) = \left(\hat{E}_R(k) + \hat{E}_S(k) \right) \left(\hat{E}_R^*(k) + \hat{E}_S^*(k) \right), \quad (2.4)$$

where the asterisk symbol denotes the complex conjugate function of the electric field.

$$\hat{I}_D(k) = \hat{E}_R(k)\hat{E}_R^*(k) + \hat{E}_S(k)\hat{E}_R^*(k) + \hat{E}_R(k)\hat{E}_S^*(k) + \hat{E}_S(k)\hat{E}_S^*(k). \quad (2.5)$$

Plugging Eq. (2.2) and Eq. (2.3) into Eq. (2.5), it can be separately expressed in the desired form as follow. The first term is

$$\hat{E}_R(k)\hat{E}_R^*(k) = [K_R r_R \hat{E}_{R0}(k) e^{jkl_R}] [K_R r_R \hat{E}_{R0}(k) e^{-jkl_R}] = |K_R r_R \hat{E}_{R0}(k)|^2. \quad (2.6)$$

The second term is

$$\begin{aligned} \hat{E}_S(k)\hat{E}_R^*(k) &= [K_S \hat{E}_{S0}(k) \int_{-\infty}^{+\infty} r_S(l_S) e^{jkl_S} dl_S] [K_R r_R \hat{E}_{R0}(k) e^{-jkl_R}] \\ &= K_S K_R r_R |\hat{E}_{S0}(k)\hat{E}_{R0}(k)| \int_{-\infty}^{+\infty} r_S(l_S) e^{jkl_S - jkl_R} dl_S. \end{aligned} \quad (2.7)$$

The third term is

$$\begin{aligned} \hat{E}_R(k)\hat{E}_S^*(k) &= [K_R r_R \hat{E}_{R0}(k) e^{jkl_R}] [K_S \hat{E}_{S0}(k) \int_{-\infty}^{+\infty} r_S(l_S) e^{-jkl_S} dl_S] \\ &= K_S K_R r_R |\hat{E}_{S0}(k)\hat{E}_{R0}(k)| \int_{-\infty}^{+\infty} r_S(l_S) e^{-(jkl_S - jkl_R)} dl_S. \end{aligned} \quad (2.8)$$

The fourth term is

$$\hat{E}_S(k)\hat{E}_S^*(k) = [K_S \hat{E}_{S0}(k) \int_{-\infty}^{+\infty} r_S(l_S) e^{jkl_S} dl_S] [K_S \hat{E}_{S0}(k) \int_{-\infty}^{+\infty} r_S(l_S) e^{-jkl_S} dl_S]$$

$$= \left| K_S \hat{E}_{S0}(k) \int_{-\infty}^{+\infty} r_S(l_S) dl_S \right|^2. \quad (2.9)$$

By plugging Eq. (2.6), (2.7), (2.8) and (2.9) back into Eq. (2.5),

$$\begin{aligned} \hat{I}_D(k) = & \left| K_R r_R \hat{E}_{R0}(k) \right|^2 + K_S K_R r_R \left| \hat{E}_{S0}(k) \hat{E}_{R0}(k) \int_{-\infty}^{+\infty} r_S(l_S) e^{jkl_S - jkl_R} dl_S + \right. \\ & \left. K_S K_R r_R \left| \hat{E}_{S0}(k) \hat{E}_{R0}(k) \int_{-\infty}^{+\infty} r_S(l_S) e^{-(jkl_S - jkl_R)} dl_S + \left| K_S \hat{E}_{S0}(k) \int_{-\infty}^{+\infty} r_S(l_S) dl_S \right|^2 \right. \right. \end{aligned} \quad (2.10)$$

Considering in ideal condition of the beam splitter with 50/50 split ratio, we can define $\hat{E}_{R0}(k) = \hat{E}_{S0}(k) = \hat{E}_0(k)$, where $\hat{E}_0(k)$ is the arbitrary spectral electric field amplitude. Besides, assuming there is no loss in both reference and sample paths ($K_R = K_S = 1$). Therefore, the spectral interference signal in Eq. (2.10) can be rewritten as

$$\begin{aligned} \hat{I}_D(k) = & \left| r_R \hat{E}_0(k) \right|^2 + r_R \left| \hat{E}_0(k) \right|^2 \int_{-\infty}^{+\infty} r_S(l_S) e^{jkl_S - jkl_R} dl_S + \\ & r_R \left| \hat{E}_0(k) \right|^2 \int_{-\infty}^{+\infty} r_S(l_S) e^{-(jkl_S - jkl_R)} dl_S + \left| \hat{E}_0(k) \int_{-\infty}^{+\infty} r_S(l_S) dl_S \right|^2. \end{aligned} \quad (2.11)$$

The first term represents a static signal called the DC-term that can be measured by blocking the signal from the sample arm. In practice, The DC-term can be removed by subtraction between the mean signal of the interference and the interference signal. The fourth term represents the auto-correlation term (AC-term) that is all of the cross interference of backscattering signals from different depths in the sample arm. The AC-term signal is much smaller than other terms in Eq. (2.11) (i.e., $r_S \ll r_R$), which can be ignored. In practice, AC-term can also be removed by blocking the reference arm then taking the subtraction directly from the interference signal. Assuming that the DC-

term and AC-term are removed, the optical path difference is defined as $l_D = l_S - l_R$, the power spectral density of the light source is $\hat{S}(k) = |\hat{E}_0(k)|^2$, and the sample reflectivity profile as a function of the optical path length difference l_D is $r_S(l_D)$, the spectral interference signal at the camera line sensor become

$$\hat{I}_{int}(k) = r_R \hat{S}(k) \int_{-\infty}^{+\infty} r_S(l_D) e^{jkl_D} dl_D + r_R \hat{S}(k) \int_{-\infty}^{+\infty} r_S(l_D) e^{-(jkl_D)} dl_D. \quad (2.12)$$

By using the definition of the Fourier transform of the space variable as

$$\hat{F}(k) = \mathfrak{F}\{f(x)\} = \int_{-\infty}^{+\infty} f(x) e^{-jkx} dx, \quad (2.13)$$

and using the property $f(-x) \xleftrightarrow{\mathfrak{F}} \hat{F}(-k)$, Eq. (2.12) can be further expressed as

$$\hat{I}_{int}(k) = r_R \hat{S}(k) \mathfrak{F}\{r_S(-l_D)\} + r_R \hat{S}(k) \mathfrak{F}\{r_S(l_D)\}, \quad (2.14)$$

$$\hat{I}_{int}(k) = r_R \hat{S}(k) [\mathfrak{F}\{r_S(-l_D)\} + \mathfrak{F}\{r_S(l_D)\}]. \quad (2.15)$$

Therefore, the inverse Fourier transform of the product of two functions in Eq. (2.15) is considered as the convolution of the two transformed functions as

$$I_{OCT}(l_D) = r_R \mathfrak{F}^{-1}\{\hat{S}(k)\} * [r_S(l_D) + r_S(-l_D)]. \quad (2.16)$$

The OCT signal or a depth-resolved reflectivity profile can be achieved by the inverse Fourier transform of the measured spectral interference signal. We defined $\gamma(l_D) = \mathfrak{F}^{-1}\{\hat{S}(k)\}$. Then Eq. (2.16) can be rewritten as

$$I_{OCT}(l_D) = r_R[\gamma(l_D)] * [r_S(l_D) + r_S(-l_D)], \quad (2.17)$$

where $\gamma(l_D)$ is an axial point spread function (PSF) of the system and $r_S(l_D)$ and $r_S(-l_D)$ is the even symmetric function of the sample reflectivity. For demonstration, assuming that the homogenous 3 layered materials is a sample, where the reflectivity is represented by the delta function at the different depth as shown in Figure 2.2.

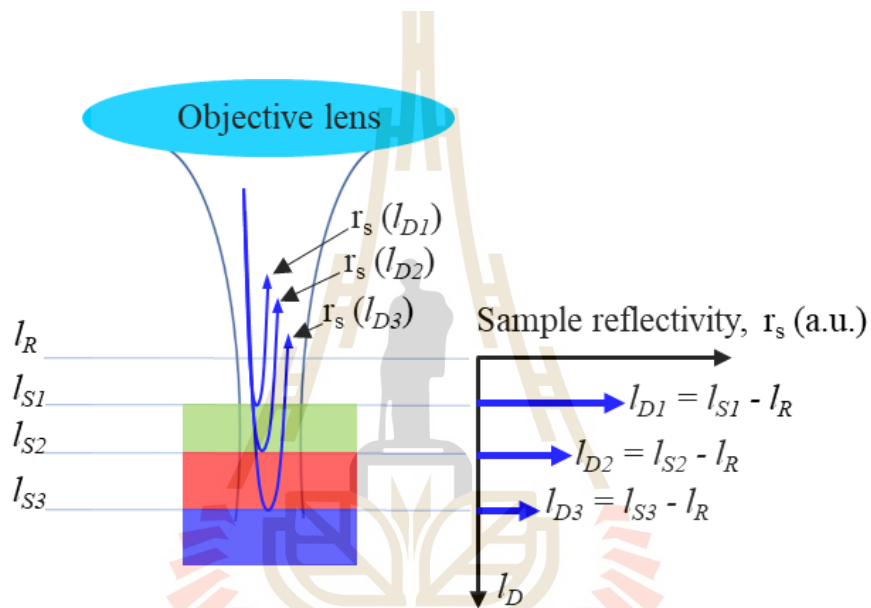


Figure 2.2 Illustration of the sample reflectivity along the depth.

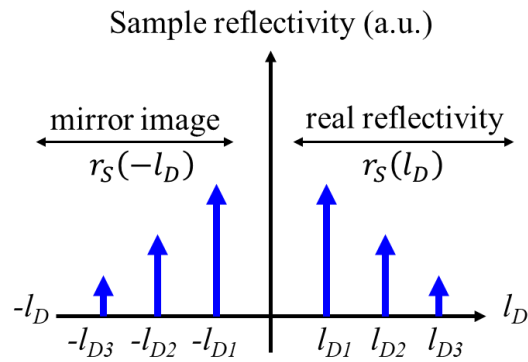


Figure 2.3 Schematic diagram shows the even symmetric function of the sample reflectivity. $r_S(l_D)$ is the real reflectivity profile of the sample. $r_S(-l_D)$ is a mirror image caused by a complex conjugate of the Fourier transform of a real function.

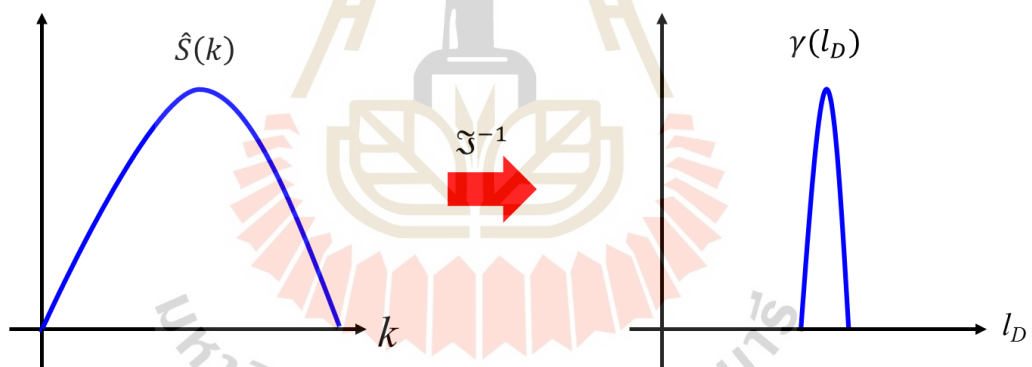


Figure 2.4 Schematic diagram shows that an axial point spread function is the inverse Fourier transform of the power spectral density of the light source.

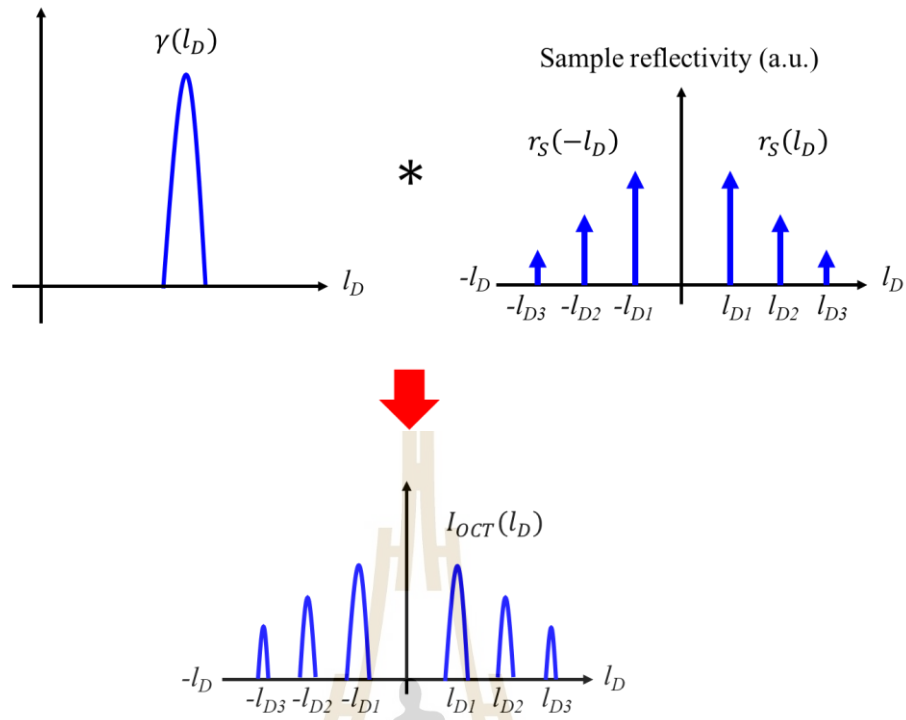


Figure 2.5 Schematic diagram shows that the resolved depth profile is a convolution between an axial point spread function and the sample reflectivity.

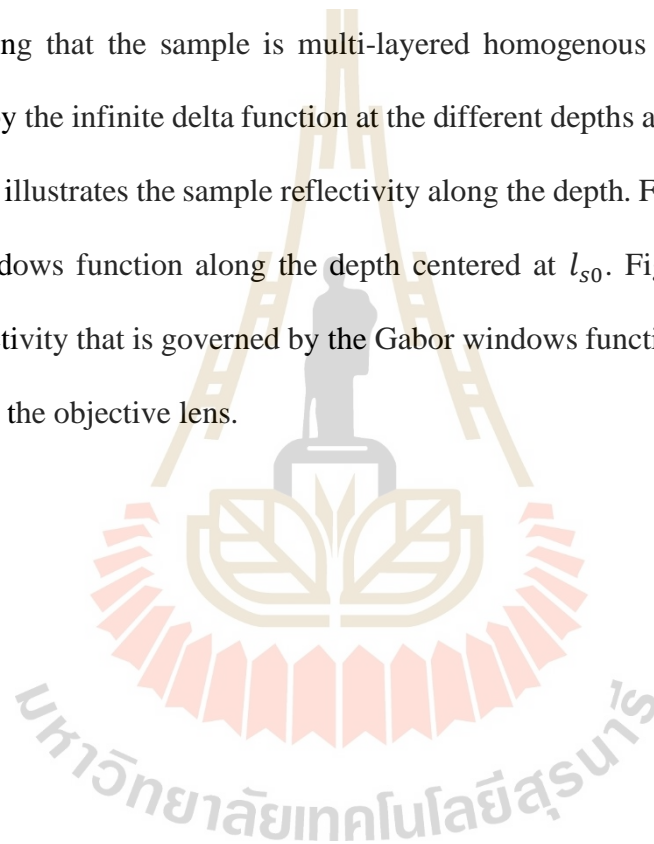
2.2.2 GD-OCM signal

Eq. (2.17) expresses the FD-OCT signal, which typically uses a low NA of the objective lens (e.g., $NA < 0.1$). To obtain both long imaging depth and high lateral resolution, GD-OCM uses a high NA of the objective lens and tunable focus techniques. With the combination of FD-OCT imaging and a high NA of the objective lens, the spectral electric field that is backscattered from the sample as given by Eq. (2.3) can be modified as

$$\hat{E}_S(k; l_{s0}) = K_S \hat{E}_{S0}(k) \int_{-\infty}^{+\infty} g(l_S - l_{s0}) \cdot r_S(l_S) e^{jkl_S} dl_S, \quad (2.18)$$

where $g(l_s - l_{s0})$ denotes a window function called Gabor window whose shape can be approximated by a function that concentrates around the position l_s equals to l_{s0} and has a finite width, which is much narrower than the function $r_s(l_s)$. In GD-OCM, where a high NA of the objective lens is used to collect reflected light from the sample, the DOF of the objective lens serves as a window function along the depth centered at the focal plane of the imaging optics located at l_{s0} .

Assuming that the sample is multi-layered homogenous materials that can be represented by the infinite delta function at the different depths as shown in Figure 2.6. Figure 2.6(a) illustrates the sample reflectivity along the depth. Figure 2.6(b) illustrates a Gabor windows function along the depth centered at l_{s0} . Figure 2.6(c) shows the sample reflectivity that is governed by the Gabor windows function that is the effect of a high NA of the objective lens.



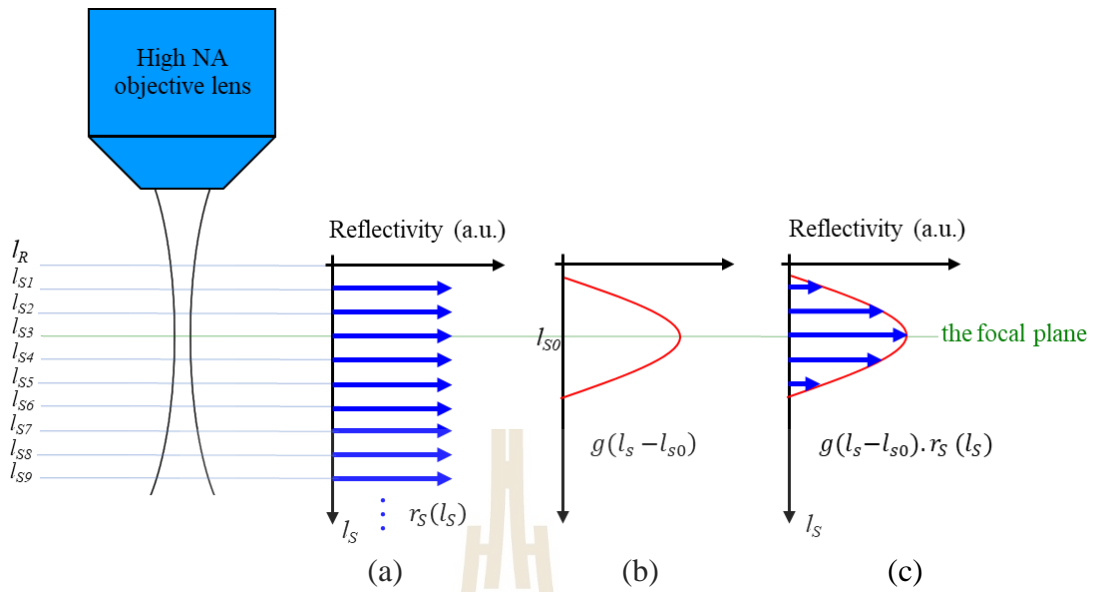


Figure 2.6 Schematic diagram shows (a) the sample reflectivity along the depth, (b) a Gabor windows function along the depth centered at l_{s0} as a result of DOF, and (c) the sample reflectivity that is governed by Gabor windows function that is the effect of a high NA of the objective lens.

Let's assume that there is no loss in both parts ($K_R = K_S = 1$) and follow in a similar way to the case of FD-OCT, the spectral interference signal obtained in GD-OCM can be expressed as

$$\hat{I}_{int}(k; l_{D0}) = r_R \hat{S}(k) \cdot \left[\int_{-\infty}^{+\infty} g(l_D - l_{D0}) \cdot r_S(l_D) e^{jk l_D} dl_D + \int_{-\infty}^{+\infty} g(l_D - l_{D0}) \cdot r_S(l_D) e^{-jk l_D} dl_D \right], \quad (2.19)$$

according to the sample reflectivity is the even symmetric function. By analyzing only the positive values of the z-axis, we obtain

$$\hat{I}_{int}(k; l_{D0}) = r_R \hat{S}(k) \cdot \left[\int_{-\infty}^{+\infty} g(l_D - l_{D0}) \cdot r_S(l_D) e^{jkl_D} dl_D \right]. \quad (2.20)$$

Eq. (2.20) shows the integration term in the form of a Gabor transform, where the DOF serves as a weighting window whose center may be shifted by varying the focal length of the dynamic focus objective lens. The term $r_R \hat{S}(k)$ in Eq. (2.20) is related to the spectral shape of the light source that can be removed by subtraction technique. Therefore, the oscillation part of the interference spectrum can be deducted as (J. P. Rolland et al., 2010)

$$\hat{F}(k; l_{D0}) = \int_{-\infty}^{+\infty} g(l_D - l_{D0}) \cdot r_S(l_D) e^{jkl_D} dl_D. \quad (2.21)$$

From Eq. (2.21), the depth profile can be reconstructed by means of an inversion of the Gabor transform or the local Fourier transform defined by (Barrett & Myers, 2004)

$$r_S(l_D) = \int_{-\infty}^{+\infty} \int_{-\infty}^{+\infty} \hat{F}(k; l_{D0}) \cdot \frac{g(l_D - l_{D0})}{\|g\|^2} e^{-jkl_D} dl_{D0} dk, \quad (2.22)$$

where $\|g\| = \left[\int_{-\infty}^{+\infty} |g(l_D)|^2 dl_D \right]^{\frac{1}{2}}$ is for normalization of the window. As a result of the normalization of the window, the production between the window and the sample reflectivity is not amplifier or change information of sample reflectivity. Using the concept of Gabor's signal expansion, the sampled version of Eq. (2.22) can be expressed as

$$r_S(l_D) = \sum_{m=-\infty}^{\infty} \sum_{n=-\infty}^{\infty} \hat{F}(k_n; m\delta l_{D0}) \cdot \frac{g(l_D - m\delta l_{D0})}{\|g\|^2} e^{-jk_n l_D}, \quad (2.23)$$

$$r_S(l_D) = \sum_{m=-\infty}^{\infty} \frac{g(l_D - m\delta l_{D0})}{\|g\|^2} \sum_{n=-\infty}^{\infty} \hat{F}(k_n; m\delta l_{D0}) \cdot e^{-jk_n l_D}, \quad (2.24)$$

where the signal $\hat{F}(k_n; m\delta l_{D0})$ corresponds to an interference fringe of the detected spectral interference signal acquired at every shift of the focal plane of the dynamic focus objective by an amount of $m\delta l_{D0}$. The number of shifting focal plane defined as m and the distance between two focusing points defined as δl_D . The term $\sum_{n=-\infty}^{\infty} \hat{F}(k_n; m\delta l_{D0}) \cdot e^{-jk_n l_D}$ in Eq. (2.24) was defined as $r_{S,m}(l_D, m\delta l_{D0})$, which represents a backscattering event that occurs within the optical path length difference l_D and within the DOF of the dynamic focusing objective when the focal plane is shifted by an amount $m\delta l_{D0}$. Eq. (2.24) can be rewritten as

$$r_S(l_D) = \sum_{m=-\infty}^{\infty} \frac{g(l_D - m\delta l_{D0})}{\|g\|^2} \cdot r_{S,m}(l_D, m\delta l_{D0}). \quad (2.25)$$

Eq. (2.25) expresses the reflectivity profile $r_S(l_D)$ in GD-OCM. By inserting Eq. (2.25) into Eq. (2.17) and considering only the positive values of the z-axis, the final GD-OCM image can be reconstructed from multiple collected GD-samples as

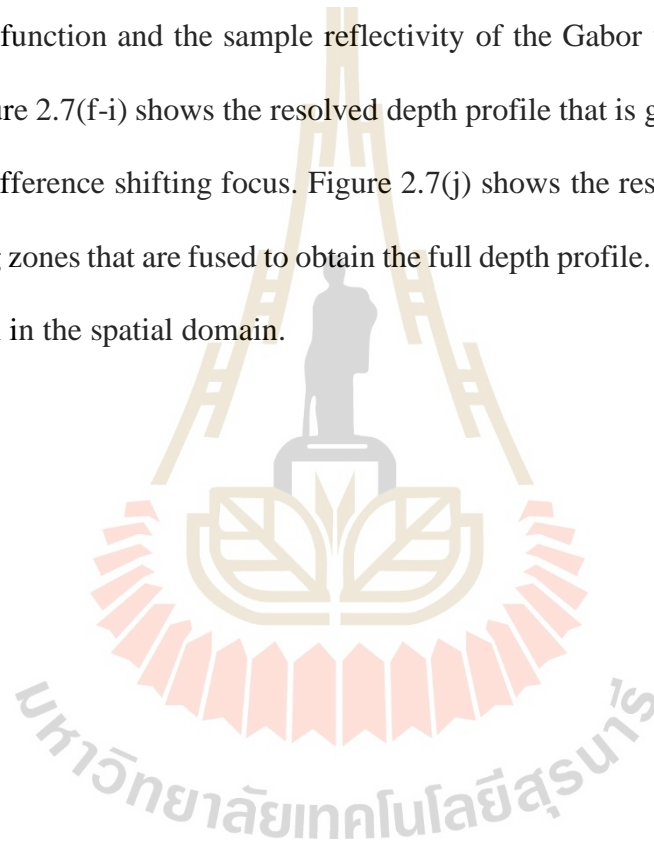
$$I_{OCT}(l_D) = r_R[\gamma(l_D)] * \left[\sum_{m=-\infty}^{\infty} \frac{g(l_D - m\delta l_{D0})}{\|g\|^2} \cdot r_{S,m}(l_D, m\delta l_D) \right], \quad (2.26)$$

$$I_{OCT}(l_D) = \sum_{m=-\infty}^{\infty} \frac{g(l_D - m\delta l_{D0})}{\|g\|^2} r_R \gamma(l_D) * r_{S,m}(l_D, m\delta l_D). \quad (2.27)$$

By defining the $I_{OCT,m}(l_D, m\delta l_D) = r_R[\gamma(l_D)] * r_{S,m}(l_D, m\delta l_D)$ as the OCT signal acquired at focus position shifted by an amount $m\delta l_{D0}$. The full depth profile of the sample reflectivity for GD-OCM or GD-fusion in the spatial domain can be written as

$$I_{GDOCM}(l_D) = \sum_{m=-\infty}^{\infty} \frac{g(l_D - m\delta l_{D0})}{\|g\|^2} \cdot I_{OCT,m}(l_D, m\delta l_{D0}). \quad (2.28)$$

For demonstration, consider the sample as the homogenous multi-layered materials as the infinite delta function as shown in Figure 2.7(a) and 4 focusing zones are determined. Figure 2.7(b) is representing the sample reflectivity at the normal focal plane or not shifting the focus. Figure 2.7(b-d) shows the convolution between an axial point spread function and the sample reflectivity of the Gabor window at each focus shifting. Figure 2.7(f-i) shows the resolved depth profile that is governed by the Gabor window at difference shifting focus. Figure 2.7(j) shows the resolved depth profile of all 4 focusing zones that are fused to obtain the full depth profile. This method is known as GD-fusion in the spatial domain.



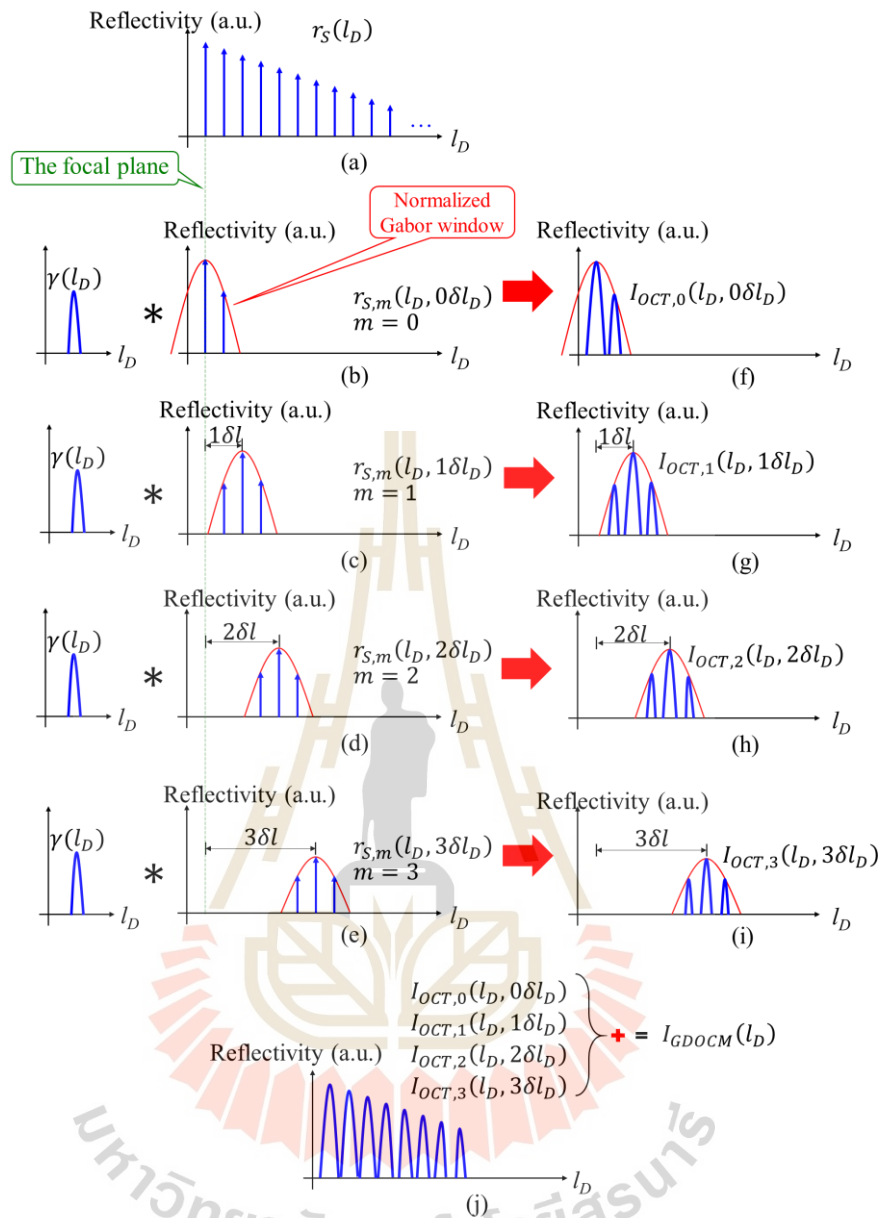


Figure 2.7 Schematic diagram shows (a) the sample reflectivity of the sample as the homogenous multi-layered materials as the infinite delta function along with the sample's depth, (b-e) the convolution between an axial point spread function and the sample reflectivity as dominated by the DOF, (f-i) the resolved depth profile where $m = 0$ represents no focus shift and $m = 1, 2, 3$ represents the shift of focus, (j) the full depth profile of the sample reflectivity as obtained by GD-fusion in the spatial domain.

2.2.3 SF-GD-OCM signal

The inverse Fourier transformation of Eq. (2.28) back to the spectral domain can be written as

$$\hat{I}_{int}(k) = \sum_{m=-\infty}^{\infty} \mathfrak{F}^{-1} \left\{ \frac{g(l_D - m\delta l_{D0})}{\|g\|^2} \right\} * \hat{I}_{int}(k, m\delta l_D). \quad (2.29)$$

The GD-fusion can be performed in the spectral domain as shown in Eq. (2.29) by the convolution of the inverse Fourier transformation of the sliding Gabor windows that is $\mathfrak{F}^{-1} \left\{ \frac{g(l_D - m\delta l_{D0})}{\|g\|^2} \right\}$ with the spectral interference signal acquired at different focus positions of the objective lens. In practice, the convolution in Eq. (2.29) is equivalent to performing a bandpass filter on a spectral interference signal (Van de Vegte, 2008). The filtered spectral interference signal are summed to one spectral interference signal, which contains only an in-focus signal. Therefore only one Fourier transform is needed to obtain the full depth profile. Eq. (2.29) expresses as spectral-domain GD-OCM or called the spectral fusing GD-OCM (SF-GD-OCM).

2.3 Digital filters

A system that can modify or change the frequency characteristic of a spectrum is known as a filter. The filters can be achieved in either an analog filter or a digital filter (Van de Vegte, 2008). A digital filter is implemented in an integrated circuit chip that is flexible for programming, while an analog filter is implemented in electrical circuit components (i.e., resistor, capacitor, and inductor). However, the main advantage of a digital filter over an analog filter is software programmable, which is convenient for redesigning or modifying the behavior of the filter (i.e., update the list of numerical coefficients). On the other hand, an analog filter needs to rebuild an electrical circuit. Furthermore, the performance of a digital filter is not significantly affected by temperature or humidity while an analog filter does. The two main types of digital filters including finite impulse response (FIR) and infinite impulse response (IIR) filters. Each type separates into four categories, including lowpass filter, highpass filter, bandpass filter, and stopband filter. The frequency between a pass frequency range or block frequency range is defined as the cut-off frequency (f_c). The lowpass filters allow lower frequency than cut-off frequency passes through to the output. The highpass filters allow higher frequency than cut-off frequency passes through to the output. The bandpass filters allow only frequency within a range of cut-off frequency 1 (f_{c1}) and cut-off frequency 2 (f_{c2}) to pass to the output. The stopband filter works oppositely to the bandpass filter. An ideal filter will give the filter gain equals to one in the passband region or equals to zero in the bandstop region. The gain of the filter is calculated by the ratio of the amplitude output and the input amplitude.

The ideal frequency response of lowpass filter, highpass filter, bandpass filter, and stopband filter, is shown in Figure 2.8(a-d), respectively.

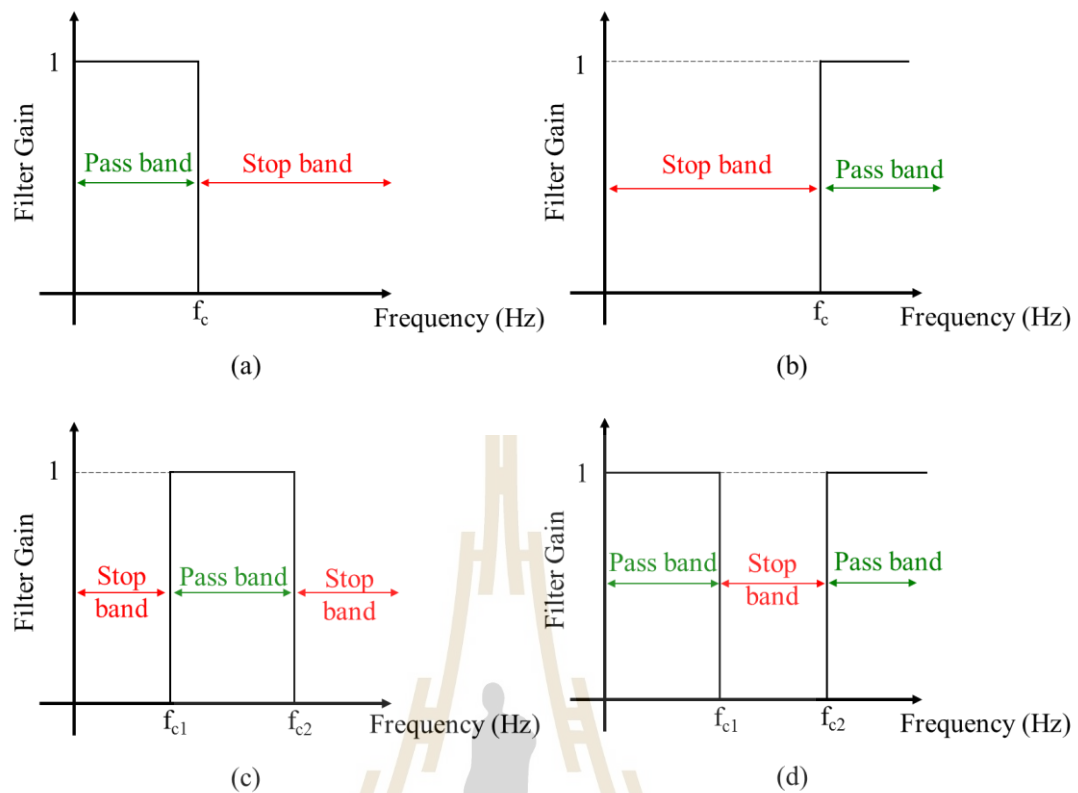


Figure 2.8 Shows the ideal frequency response of (a) lowpass filters, (b) highpass filters, (c) bandpass filters, and (d) stopband filters, where f_c = cut-off frequency.

Ideally, filter gain in passband region equals 1 in linear scale and equals 0 dB in log scale. In practice, filter gain in the passband region is not constant, which is known as the ripple (δ_p). The ripples can occur in both of passband region and stopband region. The boundary region between the passband region and stopband region is called the transition band. Typically, the width of the transition band is bounded by the cut-off frequency (i.e., defined by filter gain equals to $20\log(1 - \delta_p)$ or 0.707 in linear scale) and stop frequency (i.e., defined by filter gain equals to $20\log(\delta_p)$). In our experiment, we used a digital filter design toolkit, which is the filter designing program

from National Instrument. Considering Eq. (2.29), the Gabor window shape is a bell curve that approximates the frequency response of a bandpass filter. The practical frequency response of bandpass is shown in Figure 2.9.

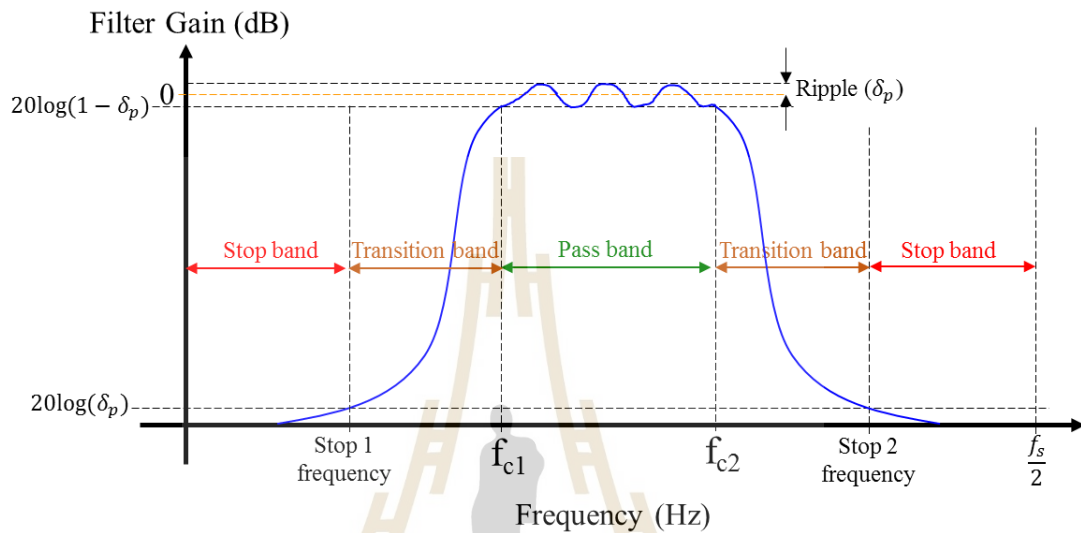


Figure 2.9 The practical frequency response of bandpass filters. The vertical axis represents filter gain in log scale and the horizontal axis represents frequency in Hz unit.

2.3.1 Mathematical equation of filters

The equation of finite impulse response (FIR) filter is given by

$$y[n] = \sum_{r=0}^M b_r x[n-r], \quad (2.30)$$

and the equation of infinite impulse response (IIR) filter is given by

$$y[n] = -\sum_{k=1}^N a_k y[n-k] + \sum_{r=0}^M b_r x[n-r], \quad (2.31)$$

where $x[n]$ is an input, $y[n]$ is an output, $y[n - k]$ is the previous output, a and b are the feedback coefficients and the forward coefficients, respectively, N and M are the total number of feedback coefficients and forward coefficients, respectively. We usually called M as order. The equation of an IIR filter has feedback. An IIR filter required a lower order than an FIR filter. Therefore, IIR filters can perform filtering faster and provide higher precision than the FIR filter (Mahotra, 2010). FIR filters require the multiplication and accumulate sum with the current input $x[n]$ that is normally implemented with the DSP module to generate the current output $y[n]$. However, IIR filters are more challenging to implement at the hardware processing level because the output current $y[n]$ depends on both the current input $x[n]$ and the previous output $y[n-k]$.

2.3.2 Sampling frequency

The interference signal as captured by the camera line sensor is equivalent to converting the interference signal into its digital representation. The beam scanning along to axial direction is taking time as the exposure time of the camera line sensor. The discrete values of the interference signal is known as a sample. The total number of samples is determined by the pixels of the camera line sensor called N_{pixel} . Therefore, time interval Δt is known as time sampling or sampling period or sampling interval as shown in Figure 2.10(a), which is defined as (Chugani, Samant, & Cerna, 1998)

$$\Delta t = \frac{\text{Exposure time}}{N_{pixel}}, \quad (2.32)$$

where Δt denotes the sampling interval in seconds per sample and N_{pixel} denotes the number of pixels of the camera line sensor. The inversion of sampling interval is known as sampling frequency that can be expressed as

$$f_s = \frac{1}{\Delta t} , \quad (2.33)$$

where f_s denotes sampling frequency in samples per second. Therefore, frequency interval or the frequency spacing as shown in Figure 2.10(b) can be calculated as

$$\Delta f = \frac{f_s}{N_{FFT}} , \quad (2.34)$$

where N_{FFT} is the number of samples in the frequency domain. From this equation, the result of multiplication of Δf and N_{FFT} is given the maximum frequency which equals the sampling frequency. Hence, the Nyquist frequency is one-half of the maximum frequency. We can express the Nyquist frequency in different terms as

$$\text{Nyquist frequency} = \frac{f_s}{2} = \frac{1}{2\Delta t} = \frac{N_{pixel}}{2(\text{Exposure time})} , \quad (2.35)$$

The sampling of the interference signal can be represented in the time domain as shown in Figure 2.10(a). Moreover, it can be represented in the frequency domain by using a fast Fourier transform as shown in Figure 2.10(b).

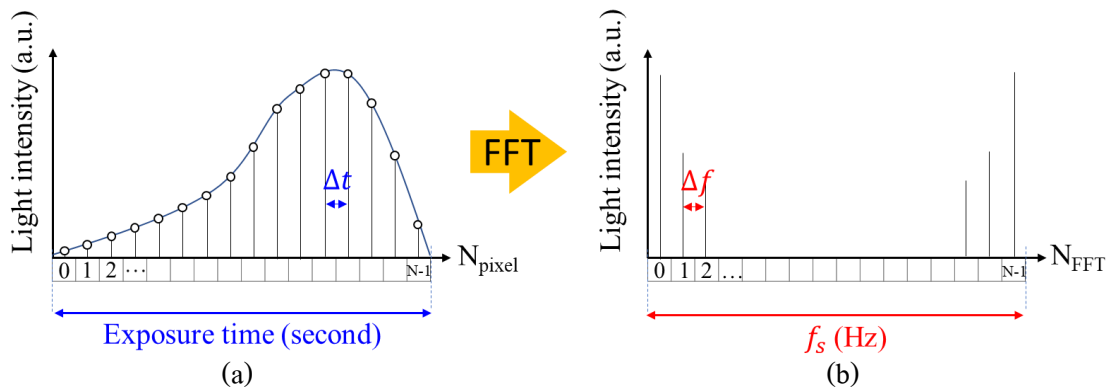


Figure 2.10 The interference signal represented by the discrete of samples in (a) time domain and (b) frequency domain. N_{pixel} = the number of pixels of the camera line sensor as known as the number of samples in the time domain, FFT = fast Fourier transform, f_s = sampling frequency, N_{FFT} = the number of samples in the frequency domain.

2.3.3 Design methods of IIR filters

There are several methods for IIR filter design. Each method provides different characteristics of frequency response, depending on the distribution of the ripple that occurs in either the passband region or the stopband region. These methods include the Butterworth method that are the smoothest frequency response with no ripple both in the passband region and stopband region. However, this method requires the highest order for designing, which leads to longer processing time. Chebyshev Type I method provides no ripple in the stopband region but allows ripple in the passband region. Chebyshev Type II method works contrariwise with Chebyshev Type I that provides no ripple in passband region and allows ripple in stopband region. Both Chebyshev Type I and Type II methods give faster frequency responses in the transition region than the Butterworth method. The Elliptic method provides ripple both of

passband region and stopband region. Normally, the Elliptic method requires the lowest order for designing. Thus, this method allows for the fastest processing time.

2.4 Implementation of digital filters on FPGA

2.4.1 FIR filter structure

Eq. (2.30) can be implemented on FPGA in simple structure as shown in Figure 2.11. FIR structure consists of multiplication, addition, and delay element used for shifting input signals. In practice, the FIR filter is commonly implemented by using the DSP module that is included in modern FPGA chips. DSP modules are pre-built logic blocks based on multiplication and addition.

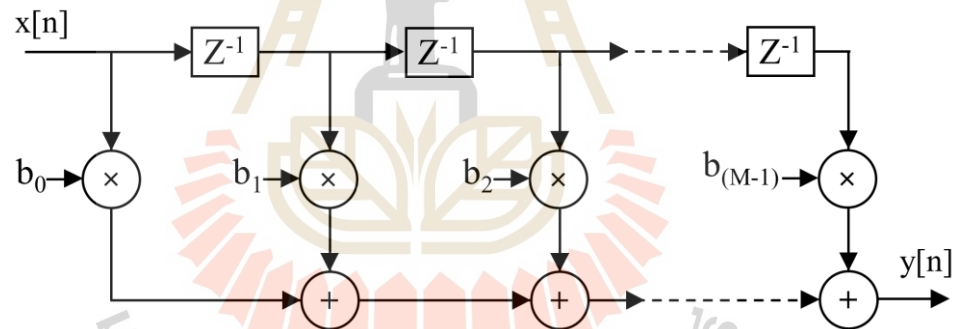


Figure 2.11 FIR filter representation in a simple structure.

2.4.2 IIR Filter Structure

From Eq. (2.31), we can implement IIR filter in different structures as follows.

2.4.2.1 Direct form I structures

The direct form I was implemented by a forward FIR filter part and a reverse FIR filter part (Francis, 2009). This structure consists of two columns as shown in Figure 2.12(a) called direct form I. On the left of the direct form I structure is

a forward FIR filter part and on the right is a reverse FIR filter part. The advantage of this structure is that it is easy to understand and implement. However, this structure is not suitable for FPGA implementation because it takes too many resources. The direct form I can be rearranged operation by taking delay element after multiplication and addition. This structure is called transpose direct form I. This could save delay element resources of FPGA as shown in Figure 2.12(b). However, the forward FIR filter part is normally more delay element required that could be a factor limit.

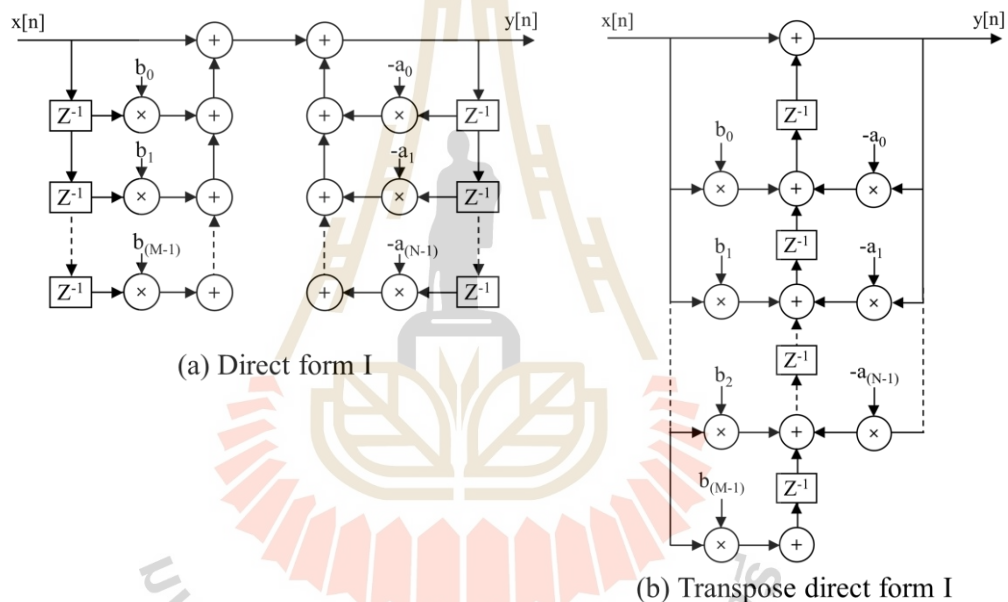


Figure 2.12 IIR structure of (a) direct form I and (b) transpose direct form I.

2.4.2.2 Direct form II structures

Direct form II can be performed by swapping the direct form I from two columns into one column as shown in Figure 2.13(a). Figure 2.13(b) shows the structure of transposed direct form II. Direct form II structure use delay less element than transposed direct form I. It provides an advantage over direct form I that requires less memory storage and handles overflow by creating the larger adder. However, these

structures provide a worse SNR if they are implemented more than 2 orders. This issue can be solved by implementing a cascaded structure, where each cascaded is handled by 2 orders. Thus, the number of cascaded stages is determined by orders divided by three. This can be formulated as $M/3$ as shown in Figure 2.14.

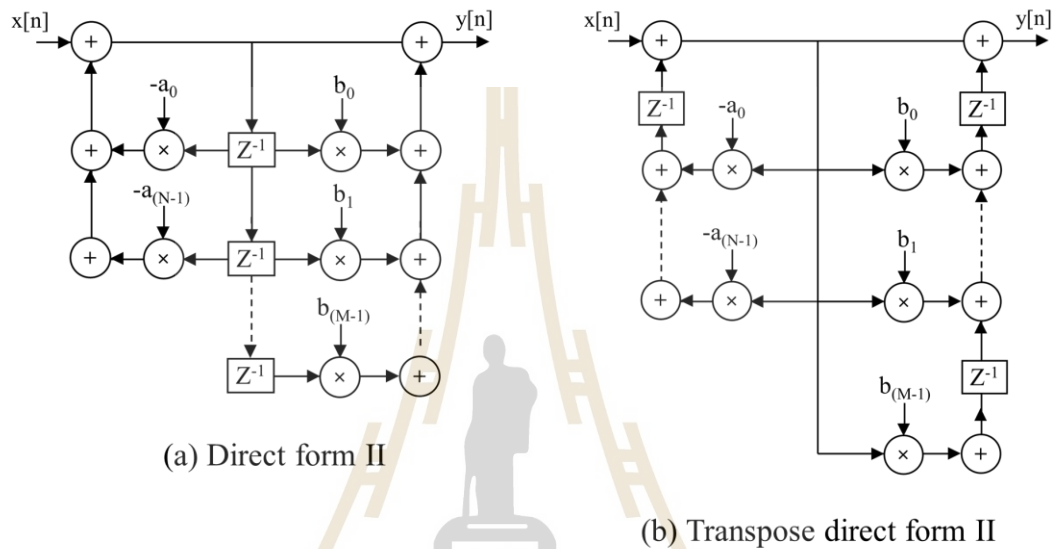


Figure 2.13 IIR structure of (a) direct form II and (b) transpose direct form II.



Figure 2.14 A cascaded structure of IIR structure.

2.5 Fixed-point implementation

FPGAs use a fixed-point data type for signal processing. The calculation speed of the fixed-point data type is faster than that of the floating-point data type. The fixed-point data type requires lower logic resources, which increase clock speed and less power consumption as compared with the floating-point numbers (Kehtarnavaz &

Mahotra, 2010). However, the disadvantage of fixed-point data type is that it is more complicated to design and lower accuracy as compared with the floating-point data type.

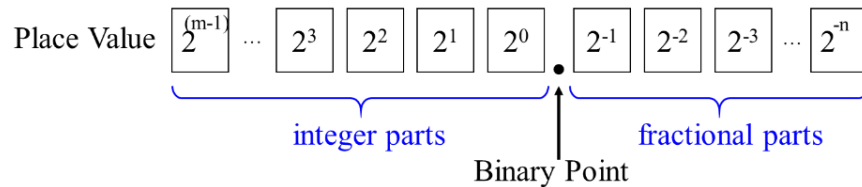


Figure 2.15 Schematic diagram shows the fixed-point representation.

The fixed-point consists of an integer part and fractional part with m and n bit, respectively, as shown in Figure 2.15. We will use a Q -point for a fixed-point number represented as $Q\ m.n$, where m is the number of integer bits and n is the number of fractional bits. The total number of integer bits and the number of fractional bits is called word length for unsigned. Plus 1 bit into m then word length for signed fixed-point is $m+n+1$. The word length normally corresponds with a processor (i.e., FPGA in LabVIEW program is allowed 64-bit maximum length on the fixed-point data type). A fixed-point number is a binary number that can represent in different Q -point formats. The fixed-point number can be designed and considered as the range and resolution of data according to archived maximum clock rate of the algorithm. The range of fixed-point can be expressed as $0 \leq \alpha \leq (2^m-1)$ for unsigned or $-(2^{m-1}) \leq \alpha \leq (2^{m-1})$ for signed. The resolution or known as a delta of the fixed-point is considered as 2^{-n} . For example, $Q3.5$ would have a word length of 8 bits as shown in Figure 2.16(a) for unsigned and Figure 2.16(b) for signed.

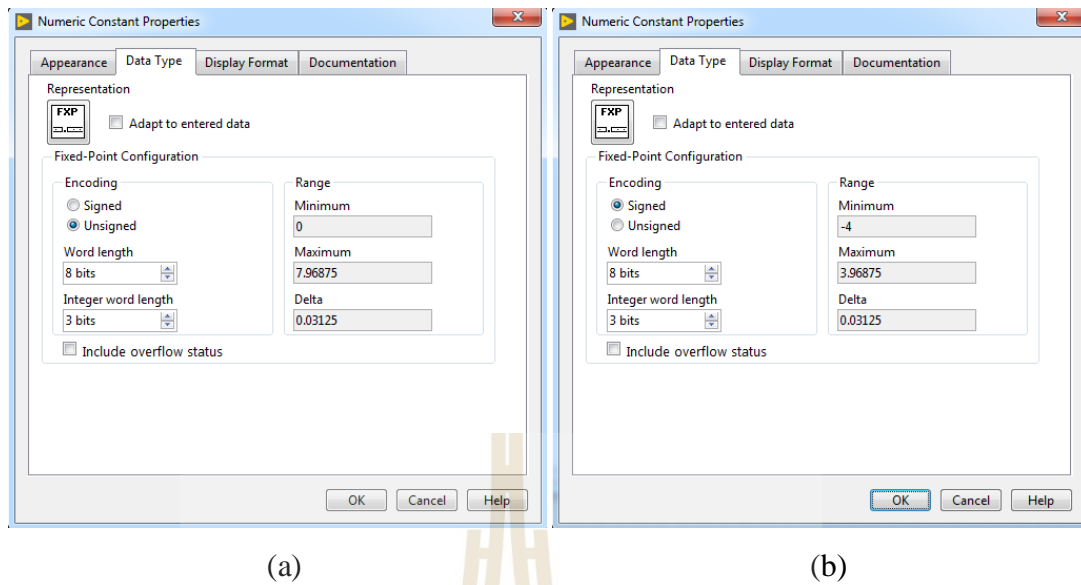
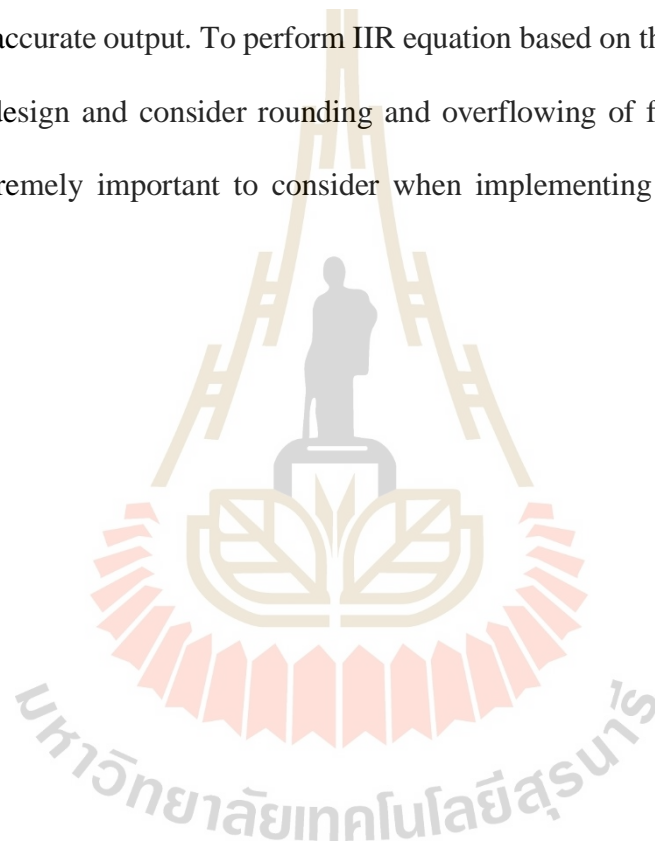


Figure 2.16 The range and resolution of (a) unsigned and (b) signed fixed-point number by using LabVIEW programming.

In the case of summation, the result of $Q_{m_1.n_1} + Q_{m_2.n_2}$ in Q format is $Q_{m_3.n_3}$, when m_3 is which m bits value is greater, then add 1 bit to prevent overflow problem, n_3 is which n bits value is greater, then select that value. For example, $Q_{3.5} + Q_{4.6}$ is $Q_{5.6}$. Moreover, in the case of multiplication, the result of $Q_{m_1.n_1}$ multiplies by $Q_{m_2.n_2}$ in Q format is $Q_{m_3.n_3}$, when $m_3 = m_1 + m_2$ and $n_3 = n_1 + n_2$. For example, $Q_{3.5} \times Q_{4.6}$ yields $Q_{7.11}$.

According to the IIR equation, multiple multiplications and summations must be performed continuously. The Q format result will become larger and larger. As a result, the speed clock of FPGA will slow down. Therefore, the output calculation of fixed-point numbers needs quantization. First, overflow mode was divided into saturate and wrap. In saturate mode, if the value is less than the minimum value, the value is set to the minimum of the output type. If the value is greater than the maximum value, the

value is set to the maximum of the output type. In wrap mode, the last bit of the value will be discarded until the value is in the range of the output type. Second, rounding mode was divided into round half to even, round half up, and truncate. Round half to even is rounding the least significant bit to zero. This rounding mode is the most accurate output. Round half up is rounding the value up. Truncate is rounding the value down by discarding the least significant bit. This rounding mode provides the best performance but the least accurate output. To perform IIR equation based on the fixed-point number, we need to design and consider rounding and overflowing of fixed-point data types, which is extremely important to consider when implementing an algorithm into an FPGA.



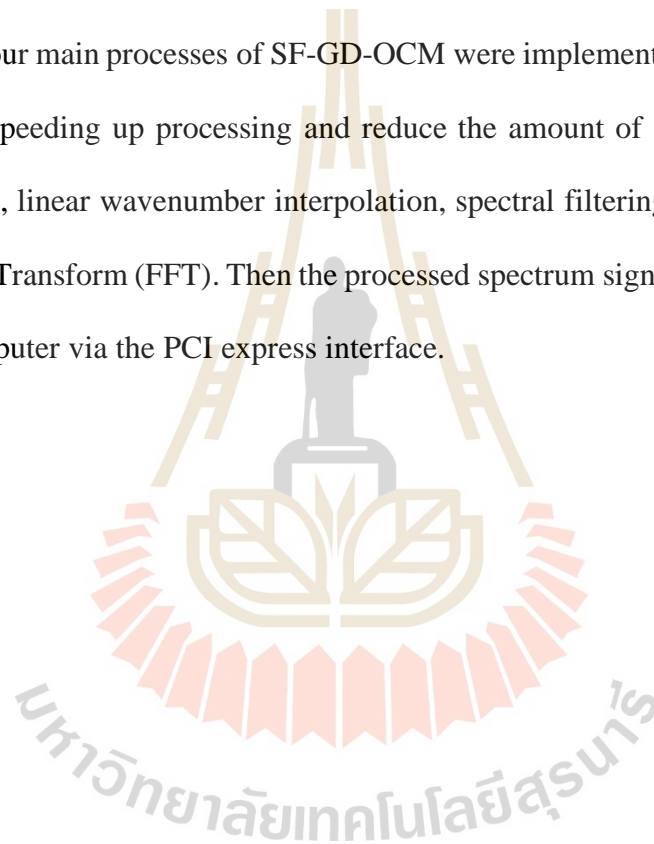
CHAPTER III

METHODS

3.1 SF-GD-OCM system setup

The interferometer was based on a free-space Michelson interferometer setup. A schematic diagram of the setup of the FPGA-based SF-GD-OCM system is illustrated in Figure 3.1(a) and the photograph of the system is shown in Figure 3.1(b). The light source was a superluminescent diode (EXS210090, Exalos AG, Switzerland) with a central wavelength (λ_0) of 840 nm and spectral width ($\Delta\lambda$) of about 70 nm. The light source was coupled to fiber and delivered to a collimator (CL₁) and then was split by a beam splitter cube (CCM1-BS014, Thorlabs Inc., USA) into two beam paths. Light in a reference beam path was reflected by a retro-reflector prism (PS975M-B, Thorlabs Inc., USA). Light in a sample beam was passed through a liquid lens (3.9 mm CA, A-39N0 Corning® Varioptic®, Edmund Optics, Singapore) for tuning of the focal plane. Then a sample beam was incident on a 2D galvanometer mirror (JD2203, Sino-Galvo Technology, China) and redirected to an objective lens that is a microscope objective (RMS10X-PF, Thorlabs Inc., USA) with 0.3 NA. Finally, the sample beam was reflected from the sample, collected by a collimator (CL₂), and delivered to a custom-built spectrometer (Meemon, Palawong, & Pongchalee, 2014). The interference signals were captured by a CMOS camera line sensor (raL6144-80km, Basler Vision Technologies, Germany). The pixel size of CMOS was 7 μm x 7 μm . The resolution of the line sensor was 6144 pixels per line and the maximum line rate was 80,000 lines

per second. The interference signals were transferred to an FPGA frame grabber (PCIe-14 73, National instruments corp., USA) through the camera link interface. We created a precision scanning system by using NI myRIO (myRIO-1900, National instruments corp., USA). NI myRIO is reconfigurable input/output (RIO) device that can be used to control a 2D galvanometer mirror and generate a pulse signal for a trigger. NI myRIO is composed of an FPGA chip and dual-core ARM cortex A9 processor. Four main processes of SF-GD-OCM were implemented in the FPGA frame grabber for speeding up processing and reduce the amount of data to transfer to the computer i.e., linear wavenumber interpolation, spectral filtering, spectral fusing, and Fast Fourier Transform (FFT). Then the processed spectrum signals were transferred to the host computer via the PCI express interface.



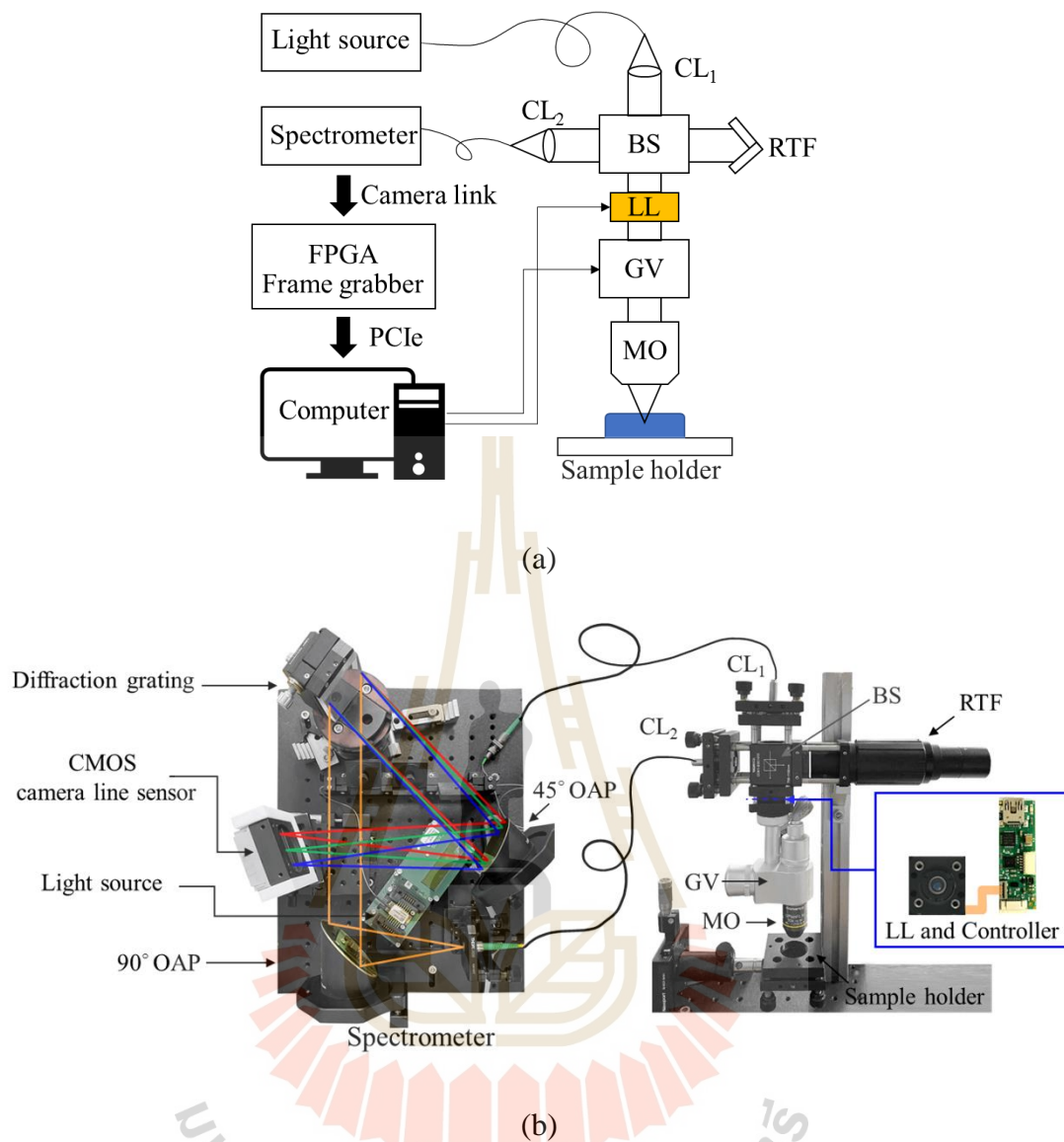


Figure 3.1 A schematic diagram of (a) setup and (b) the photograph of the FPGA-based SF-GD-OCM system; MO=microscope objective, GV=galvanometer mirror, LL=liquid lens, BS=beam splitter, CL=collimator, RTF=retro reflector.

3.2 Design of the precision scanning system

The basis for SF-GD-OCM imaging is one interference signal representing one A-scan. To get a two-dimensional and three-dimensional cross-section of a sample, we have designed the SF-GD-COM scanning system. We defined the number of A-scan as N_{x1} to represent the number of scanning on the x-axis. The exposure time is the length of time when the camera is reading data per A-scan. We designed the triangle waveform for controlling the galvanometer mirror on the x-axis as shown in Figure 3.2(c), where the rising path of the triangle waveform started from the minimum voltage (V_{min}) to the maximum voltage (V_{max}) that corresponds with the length of scanning on the x-axis in the millimeter unit. The rising period (T_1) of the triangle waveform can be calculated by the multiplication of N_{x1} and exposure time. This period also corresponds with the frame period, when the CMOS camera is reading data in as shown in Figure 3.2(b). The falling period (T_2) of the triangle waveform was set to 10% of the rising period. The falling period was designed to match the time of reading data out of the CMOS camera. The falling period also was designed to correspond with moving back of the galvanometer mirror to the minimum voltage before the next frame scanning.

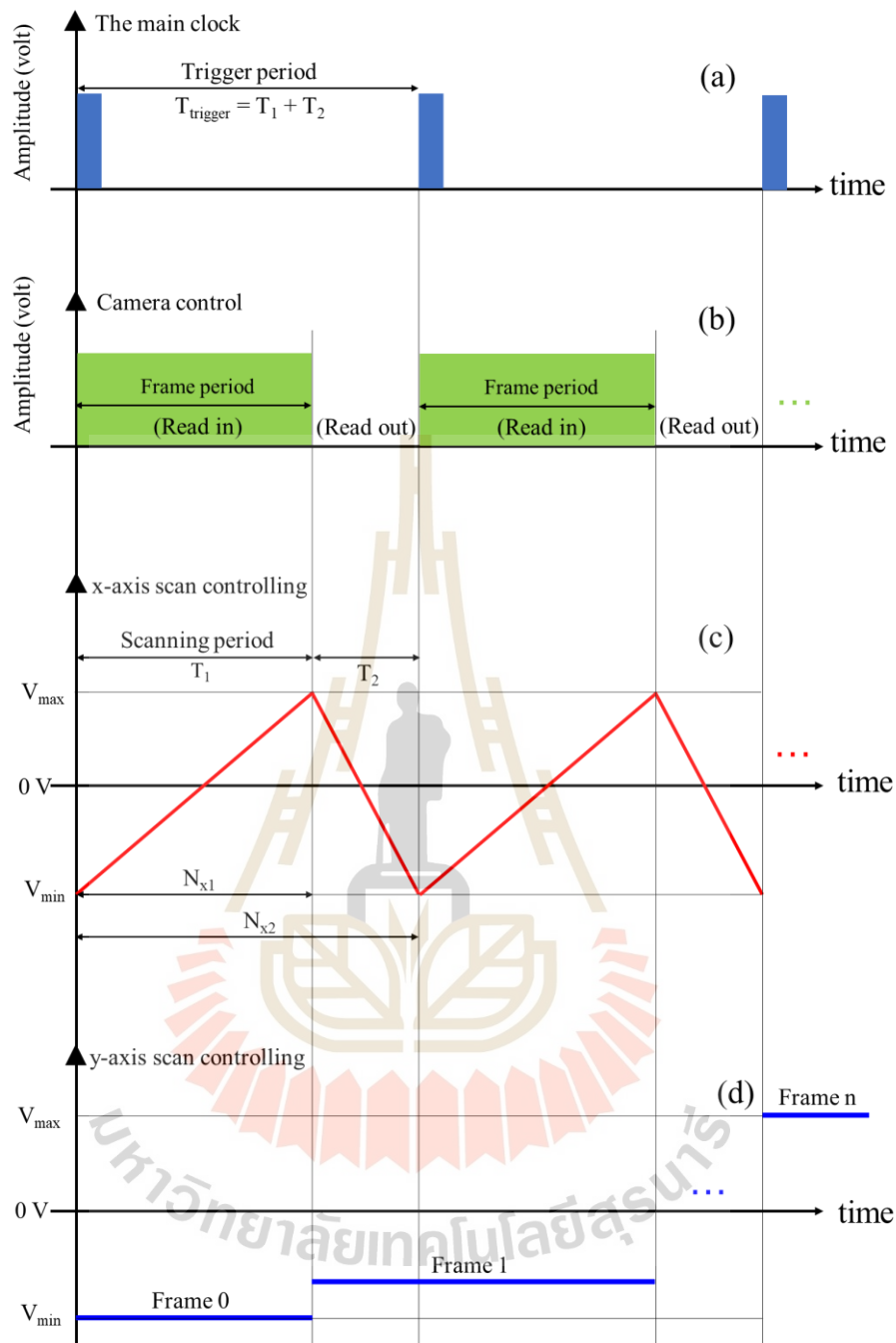


Figure 3.2 A schematic diagram shows the trigger and scanning system controlled by NI myRIO, where (a) the main clock for camera trigger and scanner trigger, (b) camera exposure control, (c) the applied voltage waveform on the galvanometer mirror for x-scan, and (d) the applied voltage on the galvanometer mirror for y-scan.

The summation of the rising period and falling period was used to define the period of pulse width modulated signal (PWM). The PWM period (T_{trigger}) can be calculated by $T_{\text{trigger}} = T_1 + T_2$. The PWM signal was used to be the main trigger called “The main clock” as shown in Figure 3.2(a). We designed a program to detect the rising edge of the main clock for the camera trigger and the x-axis scan controlling. The duty cycle of the main clock was set to 10%. For the y-axis scan controlling as shown in Figure 3.2(d), when the x-axis scan (B-scan) was finished, we increased the voltage level for moving the galvanometer mirror in the y-axis (C-scan). The range of the voltage value of the y-axis scan controlling corresponded with the length of scanning in the y-axis in the millimeter unit. The relation of all three scans is shown in Figure 3.3. The analog output channels of NI myRIO-1900 offers a digital-to-analog converter (DAC) in 12 bits resolution. These DAC can generate voltage values from -10V to +10V with 4096 different voltage levels (2^{12}). The DAC encodes 12 bits as -2047 to 2048 (a signed integer) to represent -10V and 10V, respectively.

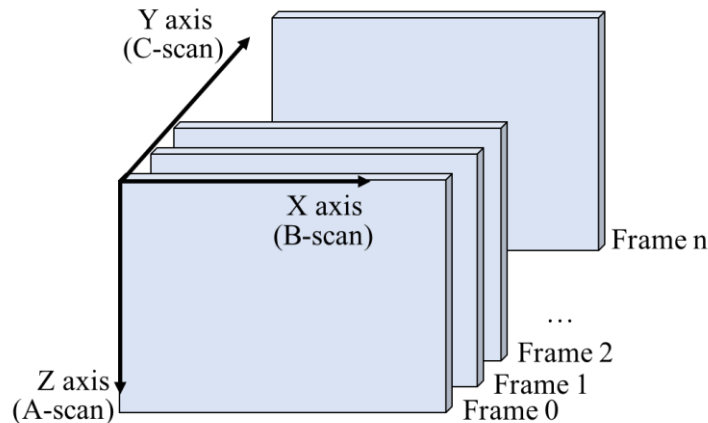


Figure 3.3 A schematic diagram shows a 3D scanning system of the SF-GD-OCM.

For demonstration, we start by specifying one cycle of the reference waveform as a triangle waveform into a look-up table as a 12-bits signed integer that contains N_{x2} sample points. In our experiment, we designed the number of A-scan to be 1000 (i.e., $N_{x1} = 1000$). Then N_{x2} is 10% more than N_{x1} , which is 1100. Besides, loop time on LabVIEW FPGA-based is normally driven by a clock rate of 40 MHz. Therefore, the loop time interval is 25 ns to produce one output voltage value. Thus, the triangle waveform period is 27.5 μs (i.e., N_{x2} multiply by loop time interval) and the frame period or the scanning period should be 25 μs (i.e., N_{x1} multiply by loop time interval). The frame acquisition on speed is about 40 kHz that is too fast for the galvanometer mirror (i.e., frequency $\leq 1000\text{Hz}$). In practice, the frame period is governed by the exposure time. For example, if we set the exposure time to 50 μs , we have to set the frame period or the scanning period to 50 ms (T_1) that is 20 frame per second. Then, the trigger period (T_{trigger}) will be 55 ms with 10% duty cycle. In practice, we added an optional delay called “trigger time delay” to expand the main trigger period in case of

galvanometer mirror cannot return back to its original position in time or solving a read-out problem of the camera.

3.3 Linear wavenumber interpolation

Because the setup of the FPGA-based SF-GD-OCM system was spectrometer-based as shown in Figure 3.1(b), the spectral interference signal as reflected from diffraction grating is linearly sampled in wavelength (λ). An equation of angular wavenumber, $k = \frac{2\pi}{\lambda}$, shows that the spectral interference signal is nonlinear in wavenumber (k) space, which causes broadening of the axial PSF after taking the Fourier transformation. Thus, all the spectral interference signals as captured by the CMOS sensor need to be recalibrated to obtain linearity in the wavenumber space. The process is called “linear wavenumber interpolation”.

From identical straight lines, the same straight line gives the same slopes. From Figure 3.4 (a), two known points (X_1, Y_1) and (X_2, Y_2) have related to an unknown point (X, Y) as

$$\text{slopes} = \frac{(Y_2 - Y_1)}{(X_2 - X_1)} = \frac{(Y_2 - Y)}{(X_2 - X)} = \frac{(Y - Y_1)}{(X - X_1)}. \quad (3.1)$$

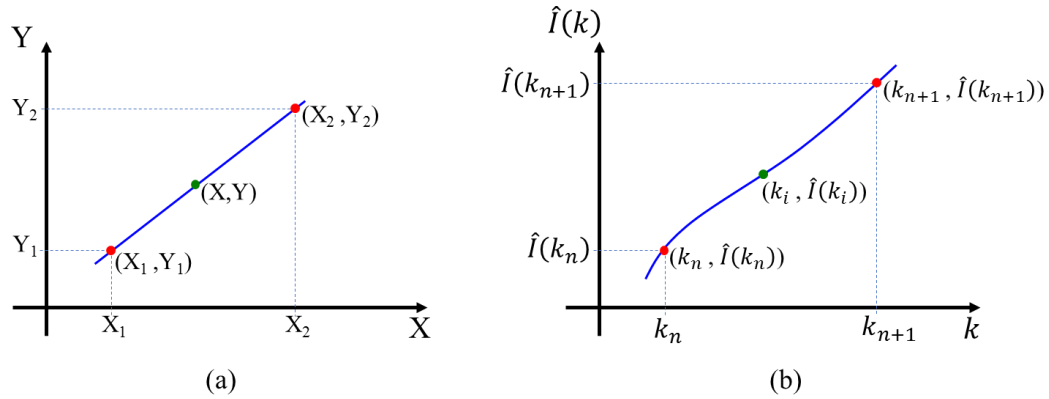


Figure 3.4 Illustrates the relation of (a) an unknown point (X, Y) with two known points (X_1, Y_1) and (X_2, Y_2) on the same straight line and (b) an unknown point $(k_i, \hat{I}(k_i))$ with two known points $(k_n, \hat{I}(k_n))$ and $(k_{n+1}, \hat{I}(k_{n+1}))$, which is a part of the spectral interference signal assume as a straight line.

We can get an unknown value (Y) at arbitrary the X value and two known points. We can rearrange Eq. (3.1) as the linear interpolation as following

$$Y = \frac{(X-X_1)}{(X_2-X_1)} (Y_2 - Y_1) + Y_1 . \quad (3.2)$$

According to Figure 3.4(b), the y-axis represents the intensity of the spectral interference signal $\hat{I}(k_n)$ as a function of k_n and the x-axis represents wavenumber (k_n). We can rewrite Eq. (3.2) as

$$\hat{I}(k_i) = \left[\frac{(k_i-k_n)}{(k_{n+1}-k_n)} \{ \hat{I}(k_{n+1}) - \hat{I}(k_n) \} \right] + \hat{I}(k_n), \quad (3.3)$$

where n is pixel number on the acquired spectral interference signal, k_n is a wavenumber at pixel number n , $\hat{I}(k_n)$ is the intensity of the spectral interference value

at pixel number n , k_i is a linear wavenumber at position i , where $n \leq i \leq n+1$. A linear wavenumber (k_i) can be created to correspond with the wavelength of the light source, $\hat{I}(k_i)$ is the linear intensity of the spectral interference value at a position of i .

Linear wavenumber interpolation from Eq. (3.3) can be easily implemented on the host computer. However, FPGA implementation of linear wavenumber interpolation is not straightforward as in the host computer because FPGA works as point-by-point processing with the fixed-point data type. Moreover, the memory block interface in FPGA is also limited by one clock cycle to retrieve one data. The steps for performing linear wavenumber on an FPGA processor can be described as follows.

3.3.1 Creating a linear wavenumber (k_i)

1. Creating linear wavelength (λ) by determining maximum and minimum of wavelength according to the light source with array size equal to total pixel number of the acquired spectral interference signal.

2. Creating a wavenumber array by taking the inverse of a linear wavelength.

3. Resampling and rescaling a wavenumber array to a linear wavenumber (k_i) by subtracting by the minimum value of the wavenumber array, and dividing by subtraction of maximum and minimum value of the wavenumber array, then multiplying by the total pixel number of the acquired spectral interference signal. As a result, a linear wavelength (k_i) was created to identify the position of i that stays between n and $n+1$. Here, $k_{n+1} - k_n = 1$, and $\frac{(k_i - k_n)}{(k_{n+1} - k_n)} = (k_i - k_n)$ can be pre-calculated.

3.3.2 Implementation of linear wavenumber interpolation

A flow diagram of the implementation of linear wavenumber interpolation on FPGA is shown in Figure 3.5. Initializing of pre-calculated coefficients of linear wavenumber interpolation were completed on the host computer as described in section 3.3.1, where the coefficient $(k_i - k_n)$ was stored as Q0.20 and the wavenumber (k_n) was stored as an unsigned 16 bits. These pre-calculated coefficients and wavenumber position were stored in a look-up table in FPGA. We used FIFO to transfer spectrum data from CMOS to FPGA. We utilized 2 memory blocks for holding and addressing an incoming spectrum amplitude $\hat{I}(k_n)$, which was stored as a signed Q12.18. In the process of interpolation, coefficients and wavenumber positions in a look-up table were called by an index of loop. The interpolation process was performed point-by-point. $\hat{I}(k_{n+1})$ and $\hat{I}(k_n)$ were called by wavenumber position for subtraction. A result of the subtraction, in Q13.18, was then multiplied by the coefficients corresponding with the wavenumber position. A result of the multiplication was quantized to Q12.18 and was added with $\hat{I}(k_n)$ and quantized to Q13.17. Repeated the process for all samples and the spectrum was linearly sampled in wavenumber $\hat{I}(k_i)$. All rounding calculations were set to truncation mode and overflow was set to wrap mode.

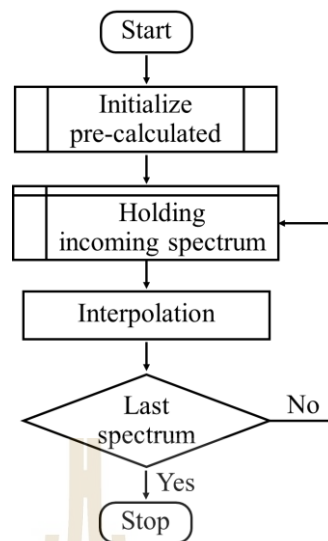


Figure 3.5 A flow diagram of the implementation of linear wavenumber interpolation.

3.4 Spectral filtering

A sliding transmission window in Gabor transformation along the axial direction (z-axis) can be considered as the translation of the DOF of an objective lens as shown in Figure 3.6. The sliding of the DOF was accomplished by using liquid lens technology. The focal plane or focus position was shifted by applying a voltage to the liquid lens. Each focus position has a Gabor window governed by the DOF. In this work, the width of the Gabor window was considered as FWHM of DOF. The multiple cross-sectional images were captured at different focus positions corresponded with the center position of each Gabor window. A GD-OCM dataset consisted of multiple cross-section images obtained from the same cross-sectional field of view. The number of the zone or the number of shifting focal planes was determined by the desired depth of the image divided by the DOF. It was defined as “zone” to represent the position of the DOF. For demonstration, a schematic diagram of 3 shifting focal planes is illustrated in Figure 3.6.

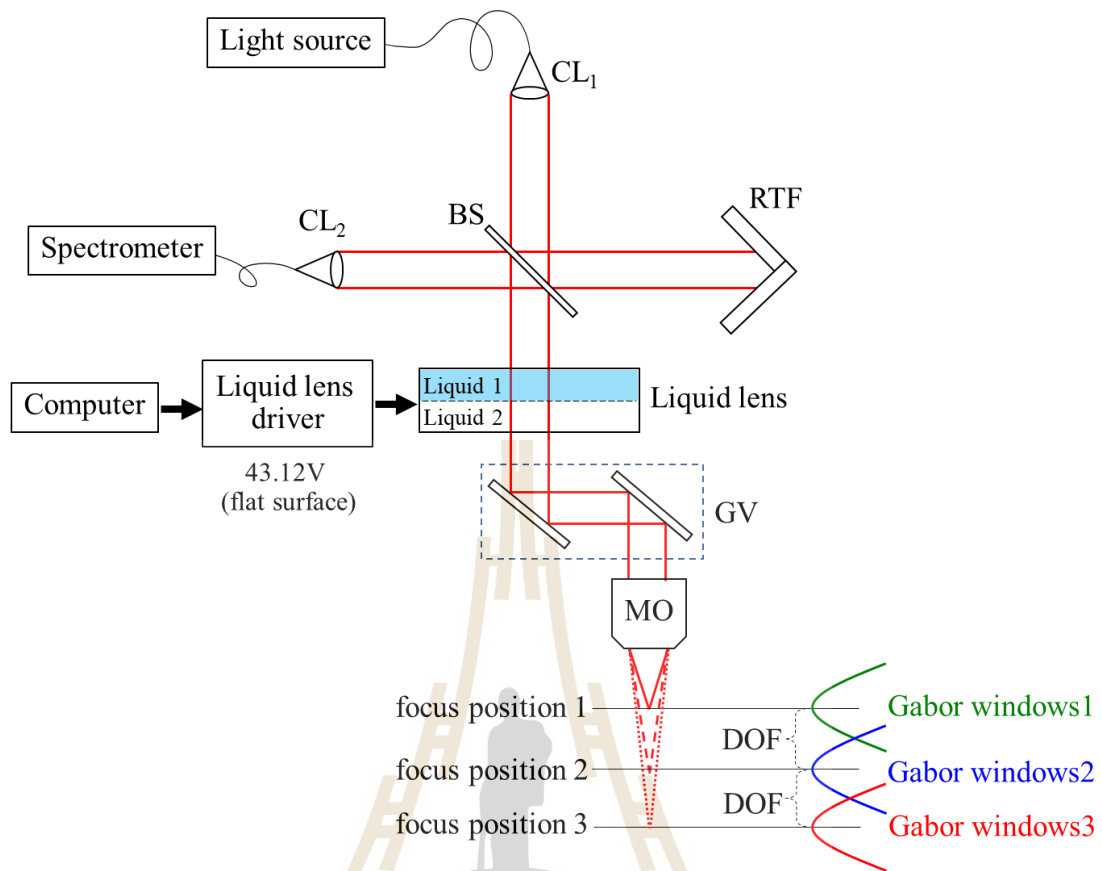


Figure 3.6 A schematic diagram of shifting focal planes; MO=microscope objective, GV=galvanometer mirror, BS=beam splitter, CL=collimator, RTF=retro reflector.

3.4.1 The relation of applied voltage and shifting of the focal planes

Ideally, the shifting interval of the focus position should be a distance equals to the DOF. In our experiment, to find the relationship between the applied voltage to the liquid lens and the actual shift of the focus, we started at the flat curvature of the liquid lens, which was considered as the normal focal plane for the system (i.e., by adjusting the voltage to the applied liquid lens to 43.12V). In this experiment, a mirror was used as the sample to obtain only one surface reflection, which represented a delta function. Therefore, only one peak of an axial point spread function (PSF)

appeared in a depth profile. To verify the effect of the DOF, we measured the amplitude of axial PSFs at 10 different depth positions with 20 μm apart and performed an overlay plot in pixels as shown in Figure 3.7(a). The y-axis represents normalized amplitude and the x-axis represents the depth profile in pixels, i.e., $N_{FFT} = 4096$. The different color in Figure 3.7(a) represents each PSF at different depth positions. These PSFs were enveloped by the DOF around the focus position. In our experiment, we considered the focal plane when the optical power of the liquid lens is zero as zone 1, where the Gabor window is located at the depth location as shown in Figure 3.7(a). For the sliding of the Gabor window, we considered a shift distance that caused the right side of the FWHM of the first Gabor window was at the same pixel position with the left side of the FWHM of the next Gabor windows. Therefore, we adjusted the applied voltage of the liquid lens until we obtained the left side of the FWHM of the second Gabor window was at the targeted position. At zone 2, we recorded the voltage and repeated the measurement of the amplitude of an axial PSFs as previously done in Figure 3.7(a) and obtained overlaid plots as shown in Figure 3.7(b). Moreover, Figure 3.7(c) shows overlaid plots of zone 3. The crossing of the FWHM of each Gabor window as shown in Figure 3.7(d) was used to verify the appropriate shift of sliding Gabor windows. The process was repeated until the desired image depth range was achieved.

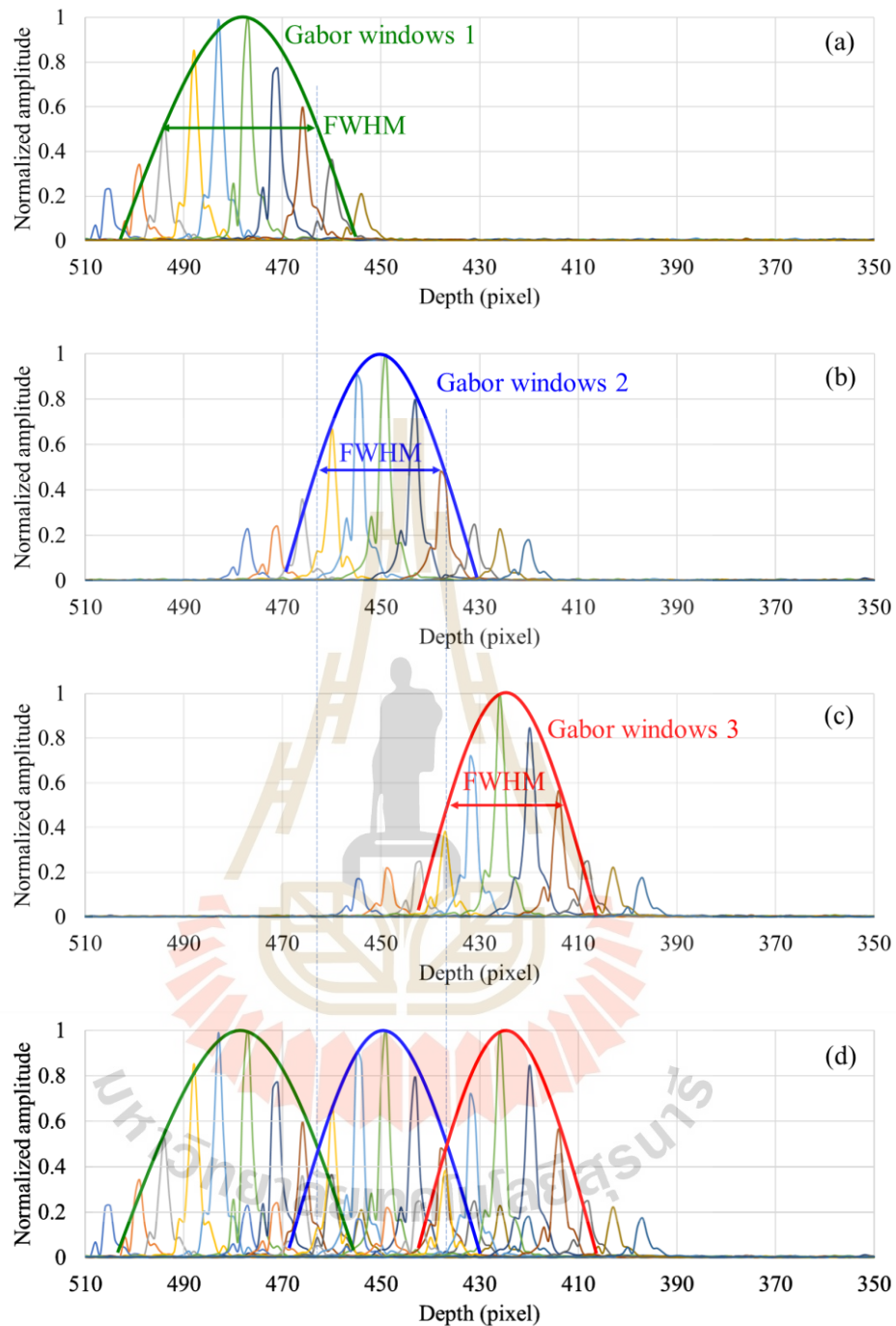


Figure 3.7 The overlaid plot of multiple depth profiles measured at different positions (in the air) of the sample in the range of 350-510 (i.e., $N_{\text{FFT}} = 4096$), showing the effect of (a) Gabor window 1, (b) Gabor window 2, and (c) Gabor window 3, and (d) A superposition of (a-c).

3.4.2 Finding cut-off frequency for spectral filtering

As clearly observed from Figure 3.7(d), if we directly fuse the multiple focus positions to one cross-sectional field of view, out-focus information of each zone will disturb in-focus information of other zones, causing ghost images. Furthermore, the convolution of Gabor windows and linear spectral interference signal in Eq. (2.29) is equivalent to the digital filter process. Therefore, digital filters were designed to keep in-focus and suppress out-of-focus information of the cross-sectional image. As explained in section 2.3, the digital bandpass filter (BPF) of Chebyshev type I filter was chosen because it provided a fast response in the transition region, no ripple in the stopband region, and low ripple in the passband region. BPF removed DC signal, AC signal, and noise that were out-of-focus. Each zone required a different bandpass filter to match the shifted Gabor window. Each bandpass filter was designed passband region to approximately match the DOF at different focus positions. The depth profile plotted in pixels can be plotted in frequencies by using the relation of Eq. 2.31, Eq. 2.32, Eq. 2.33, and Eq 2.34. Therefore, we can determine the cut-off frequencies from the plot of depth profile versus frequencies. In our experiment, We set exposur time to 50 μ s and the interference signal was captured by 3500 pixels on the sensor. The sampling frequency (f_s) was calculated to be 70 MHz. By using N_{FFT} of 4096 points, we calculated Δf to be 17089.84 Hz and hence we can display the overlaid plot of data in zone 1, zone 2, and zone 3 in MHz as shown in Figure 3.8(a), Figure 3.8(b), and Figure 3.8(c), respectively.

Considering the depth profile versus frequencies as shown in Figure 3.8(a), the passband region of zone 1 is bounded by f_{Hc1} and f_{Lc1} , corresponding with the width of the DOF at that position. We measured the cut-off frequency to be approximately, $f_{Hc1} = 8.44$ MHz (at pixel 494) and $f_{Lc1} = 7.91$ MHz (at pixel 463). In

similar manner, $f_{Hc2} = 7.91$ MHz (at pixel 463) and $f_{Lc2} = 7.46$ MHz (at pixel 437) for zone 2 as shown in Figure 3.8(b), and $f_{Hc3} = 7.46$ MHz (at pixel 437) and $f_{Lc3} = 7.02$ MHz (at pixel 411) for zone 3 as shown in Figure 3.8(c). The result of other zones will be reported in chapter 4.

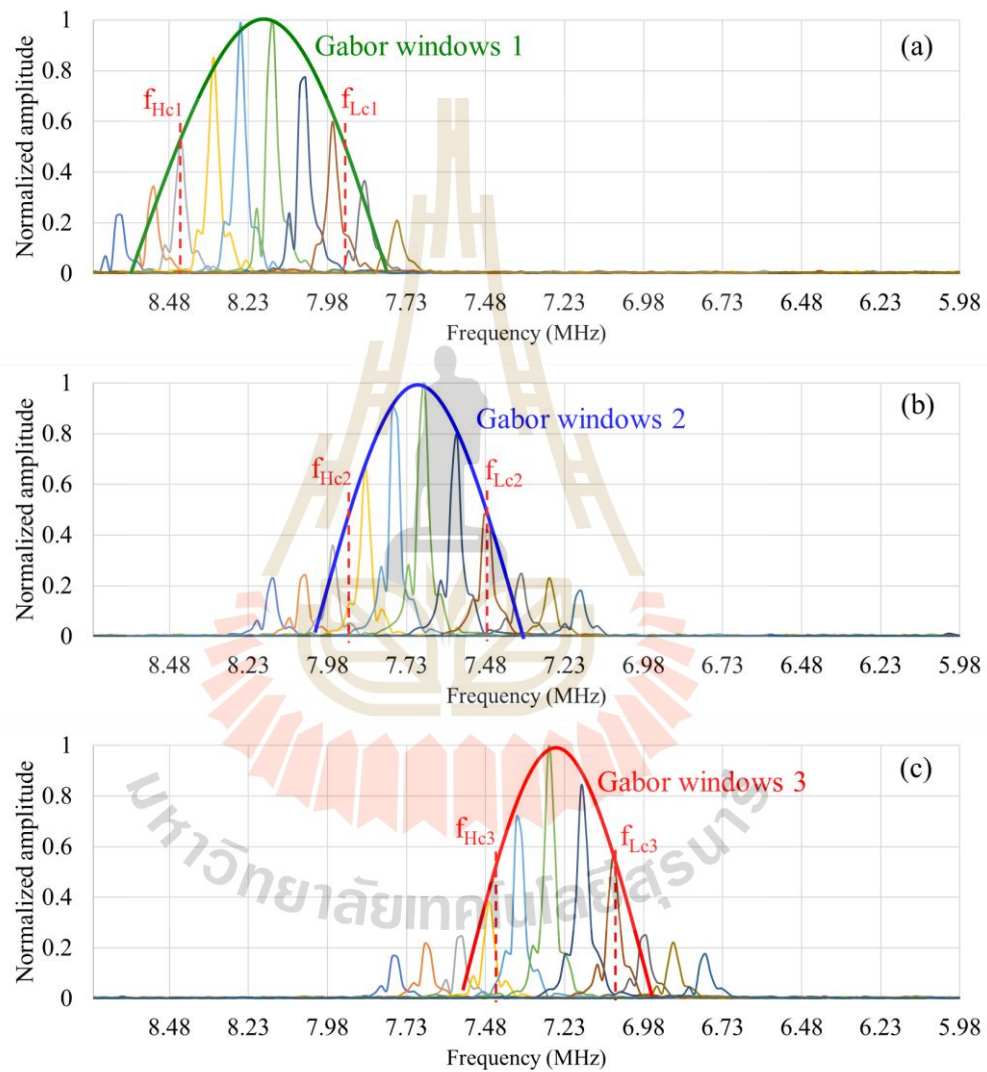


Figure 3.8 The superposition of multiple depth profiles obtained at different positions (in the air) of the sample in MHz, which allows for determination of cut-off frequencies as (a) f_{Hc1} and f_{Lc1} for zone 1, (b) f_{Hc2} , and f_{Lc2} for zone 2, (c) f_{Hc3} and f_{Lc3} for zone 3.

3.4.3. Designing of spectral filter

The digital filter design (DFD) toolkit was chosen for the design and characterization of the frequency response of the filter. We implemented and compared the performance of spectral filtering by varying the order of the filter as previously reported (Lenaphet & Meemon, 2020). According to the experiment result, the sixth order of Chebyshev Type I was the lowest order to be able to suppress the out-of-focus. However, the 10th order of Chebyshev Type I gave a better quality of the fused image. Each bandpass filter was pre-determined a cut-off frequency to approximately match with a difference DOF of each zone. Moreover, we did an extra experiment to verify the affected of the phase response of filter reported in appendix I. Resulted, the phase alteration of the spectral interference signal after performing FFT has not affected the structural image of FPGA-based SF-GD-OCM. For demonstration of designing of spectral filter of Figure 3.8(a) that was defined as zone 1, we designed the bandpass filter 1 (BPF1), corresponding to zone 1, by defining the filter specification as following

Table 3.1 Example of the filter specification for zone 1.

Filter type	Bandpass filter
Design method	IIR with Chebyshev Type I
Sampling frequency	70 MHz
High cut-off frequency (f_{Hc1})	8.44 MHz
Low cut-off frequency (f_{Lc2})	7.91 MHz
Order	10
Bandpass ripple	0.1 dB
Filter structure	Cascaded second-order section form II

3.4.4 Implementation of spectral filter on FPGA

The implementation of each bandpass filter on FPGA, Chebyshev type I with cascaded second-order section form II structure, was implemented as shown in Figure 3.9.

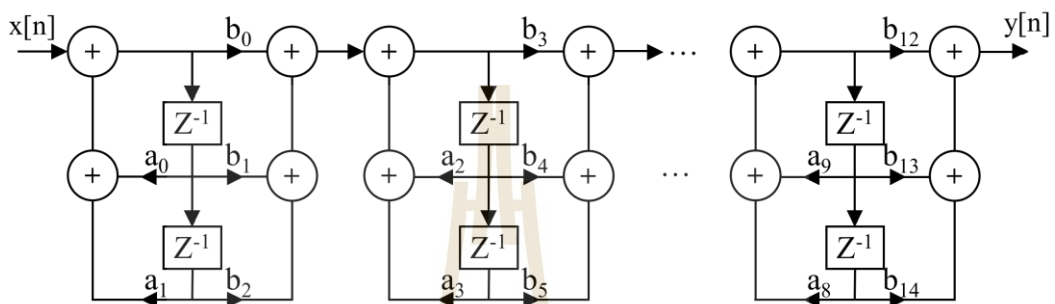


Figure 3.9 Implementation of the 10th order of bandpass filter of Chebyshev type I with cascaded second-order section form II structure.

Each bandpass filter was pre-built and implemented as intellectual property integration node (IP Integration Node), where the throughput was maximized. The fixed-point number was considered to be the smallest number while maintaining the performance of the filter. The input of the filter was the output from linear wavenumber interpolation. All calculations of the filter were quantized to Q9.15. The spectral filtering system of FPGA-based GD-OCM is presented by a flow diagram as shown in Figure 3.10.

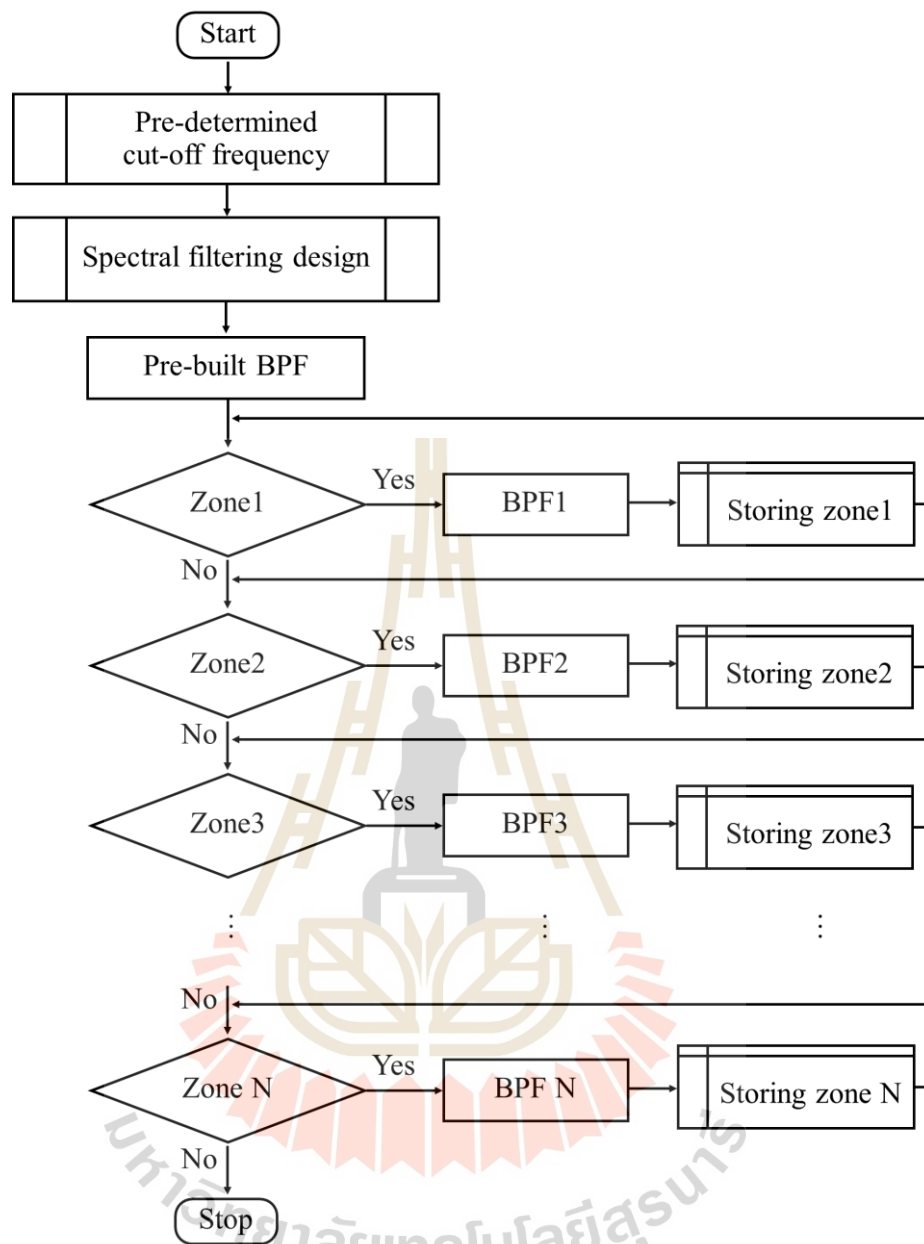


Figure 3.10 A flow diagram of the spectral filtering process of FPGA-based SF-GD-OCM. BPF = the digital bandpass filter.

Figure 3.10 shows the spectral filtering process based on the point-by-point operation. Therefore, the counter was used for making zoning decisions. For example, in two-dimension scanning, if the spectrum was sampled as 3500 samples per spectrum, each

frame of the GD-OCM dataset contains 500 spectra, and use “ i ” as a counter. Zone 1, the loop running between $1 \leq i \leq 1,750,000$ will be performed BPF1. For three-dimension scanning, if we need 500 frames, a loop running between $1 \leq i \leq 875,000,000$ will be needed to process BPF1. Sequentially, each filtered spectrum was stored in a memory block of FPGA, corresponding with their zone as shown in Figure 3.10. These filtered spectra will be fused in the next process.

3.5 Spectral fusing

The sigma symbol in Eq. 2.29 is known as the Gabor fusing in the spectral domain. The spectral fusing process can be achieved by a linear summation of filtered spectra that are matched with the actual DOF in each focusing position of the GD-OCM dataset. In practice, the implementation of Gabor fusing in spectral-domain on FPGA-based was a point-by-point basis. All filtered spectra were called at the same wavenumber position for summation that led to the parallel summation of all zone to one fused spectral signal. A flow diagram of the spectral fusion is shown in Figure 3.11.

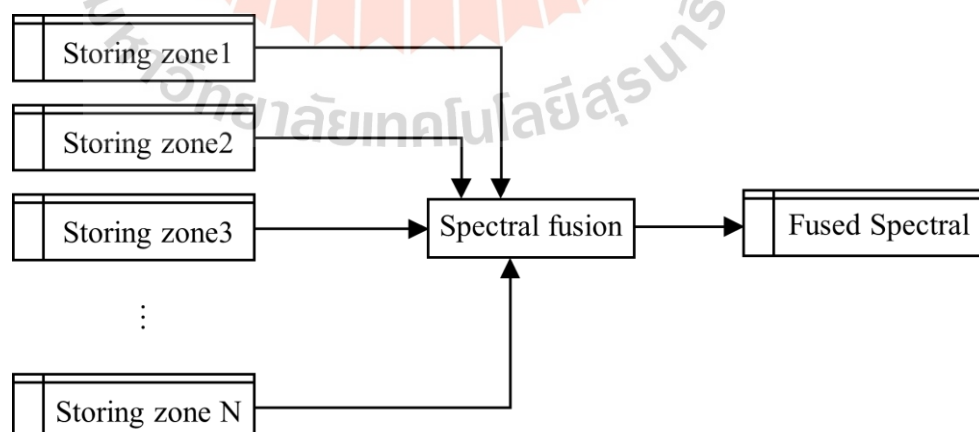


Figure 3.11 A flow diagram of the spectral fusing process with the parallel summation of filtered spectral.

3.6 Fast Fourier transform

In this study, it is possible to perform a Fast Fourier Transform (FFT) directly on the fused spectra in the FPGA device in real-time. FFT in FPGA was performed by pre-built DSP blocks as part of FFT express VI. Each fused spectrum was performed FFT to obtain the depth profile then transferred to the host computer memory using direct access memory through the PCI express bus. To achieve the highest throughput, FFT should be directly programmed and configured by the Xilinx core which could be future work.

3.7 Performance of FPGA-based SF-GD-OCM

The optical design and alignment of all optical components of the custom-built spectrometer are key to determine the optical resolution of the system. The digital resolution is defined by the number of sensor pixels per line scan. These two resolutions affect the spectral resolution. The effective spectral resolution of the spectrometer can be measured by the modulation depth of spectral fringes at different depth positions. In our calibration of the depth scale of the depth scan, a mirror was used as a sample because it has only one surface reflection, which represents a delta function. Therefore, only one peak of an axial PSF represents a depth profile after performing the FFT of the spectral interference signal. We adjusted the micrometer of a sample holder (i.e., changing of a sample path length) to change the position of PSFs. We measured the amplitude of PSFs at 50 different depth positions with 20 μm apart as shown in Figure 3.12.

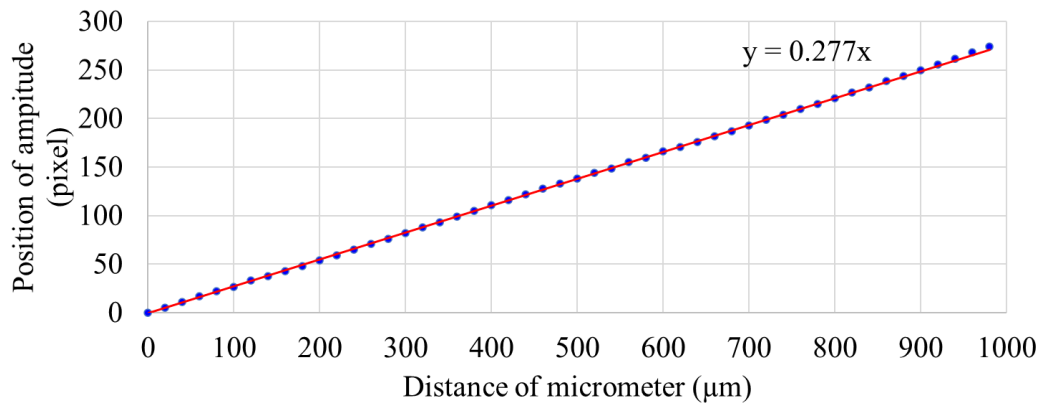


Figure 3.12 The relation between the position of the peak amplitude of the PSF in pixel and the translation distance of the mirror sample measured in micrometer.

Figure 3.12 shows the relationship of the peak location of the depth profile in pixels and the translation distance of the mirror sample in micrometer as blue point, which exhibits linear relation. Therefore, we took linear fitting (red line). We got $y=0.277x$. The linear equation of the plot was used for calibration of the depth scale of the depth scan. We found that one pixel equals the actual depth distance in the air of $3.61 \mu\text{m}$.

The axial position and amplitude of an axial point spread function (PSF) are related with the fringe frequency. The fringe frequency can be changed by changing the optical path difference (OPD). Typically, the maximum imaging depth (Z_{max}) of OCT imaging can be determined by the dropping of the amplitude of an axial point spread function (PSF) by about ten times as compared with the maximum amplitude. The dropping in the amplitude of the PSF is caused by the increase of fringe frequency when the optical path difference increases as shown in Figure 3.13(a-c). For GD-OCM imaging, the amplitude of the PSFs is also governed by the Gabor windows at each focus positions. Therefore, we measured the amplitude of PSFs at 19 different focus positions with 1 voltage apart on the liquid lens as shown in Figure 3.13(d), i.e., 30V -

48V to the liquid lens. Hence, the maximum imaging depth of this system was measured to be about 2.25 mm in the air.

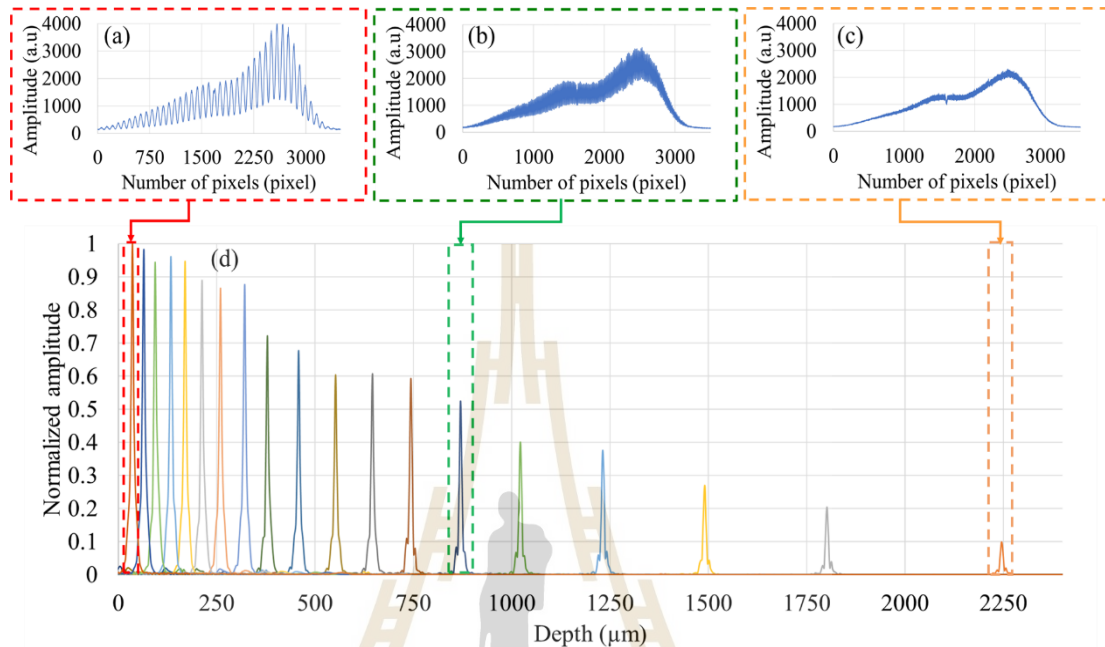


Figure 3.13 An example of the fringe frequency at difference OPD (a-c) that corresponding to the applied voltage of liquid lens, 30V, 43V, and 45V, respectively. (d) The superposition of multiple depth profiles obtained at different focus depth positions with 1 voltage apart in the air of the mirror sample measured in micrometers.

In general, the axial resolution (Δz) is determined by the FWHM of the depth profile in micrometers at a focus position. For example, the axial resolution at the focus position of 30V applied voltage on the liquid lens, the zoom-in from the red dashed box dash in Figure 3.13(d), is shown in Figure 3.14(a). The axial resolution (Δz) at the focus position of 30V was measured to be 8 μm in air. Furthermore, the lateral resolution both of x-axis and y-axis was determined by three-dimension scanning of a standard

USAF 1951 target, and reconstructed an *en-face* view. For example, the lateral resolution of focus position at 30V in *en-face* view at the focal plane is shown in Figure 3.14(b). The FPGA-based SF-GD-OCM system can resolve down to the 6th element of group +7, which is marked in the red solid box, which corresponds with the lateral resolution of 2.2 μm in the air. The axial resolution and lateral resolution of other focus positions will be reported in chapter 4.

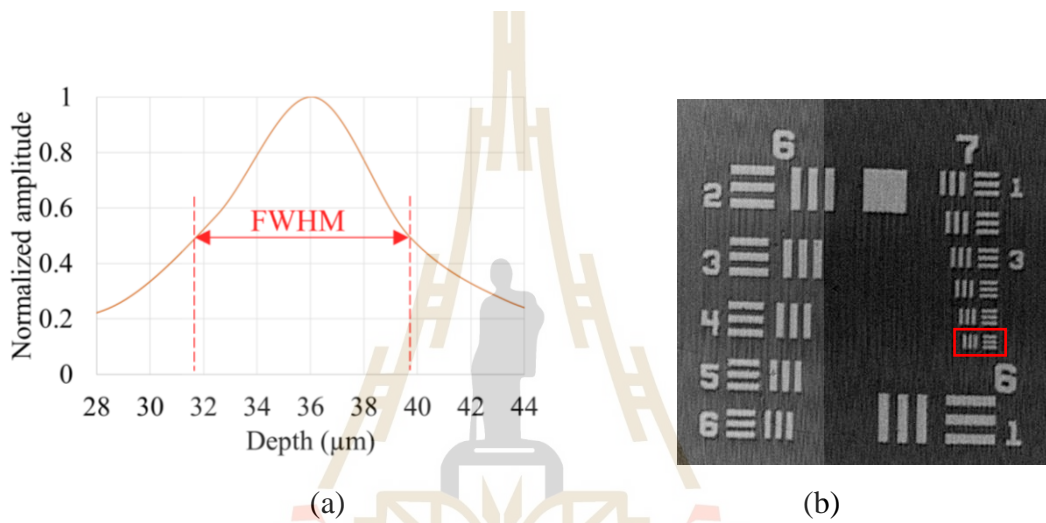


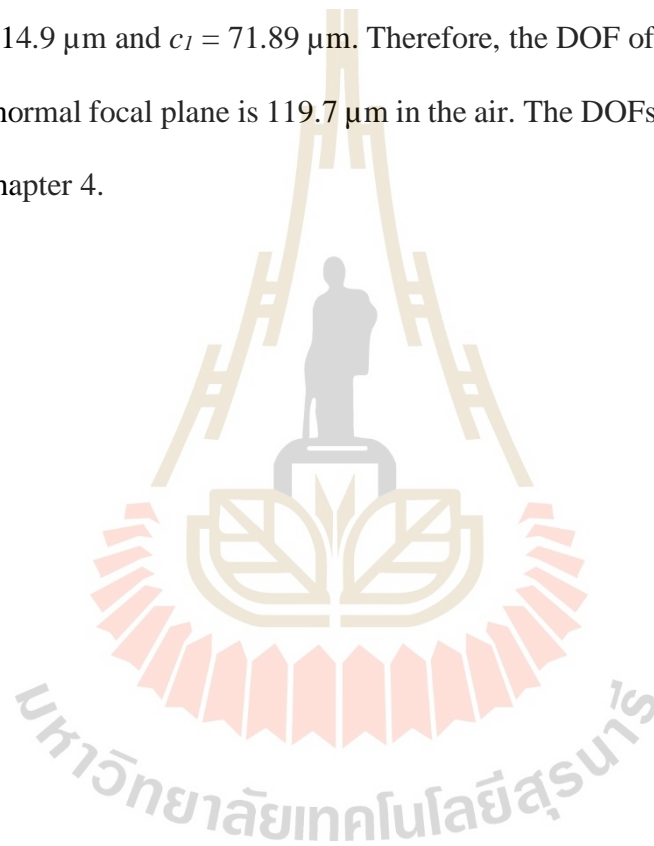
Figure 3.14 Example of (a) the zoom in from the red dashed box in Figure 3.13(d) and (b) *en-face* view of a standard USAF 1951 target of focus position at 30V.

Furthermore, we defined the DOF of FPGA-based SF-GD-OCM as the FWHM of Gabor windows. To estimate the Gabor window for each zone, we plotted an axial PSFs over depth in micrometers. Then, we used MATLAB program for Gaussian fitting, which determined Gaussian equation as

$$f(x) = a_1 e^{\left(\frac{x-b_1}{c_1}\right)^2}, \quad (3.4)$$

$$FWHM = 2c_1 \sqrt{\ln 2}, \quad (3.5)$$

where $f(x)$ represents Gaussian function, a_l represents amplitude, b_l represents the center location, c_l represents the peak width, and FWHM is full-width half maximum of Gaussian function (Mathworks, 2016). For demonstration, we plotted the amplitude of axial PSFs at 10 different depth positions with $20\ \mu\text{m}$ apart as shown in Figure 3.15(a). The result of the Gaussian fitting of the normal focal plane is shown as a red line in Figure 3.15(b). The Gabor window of zone 1 is shown in Figure 3.15(c). We got $a_l = 1$, $b_l = 114.9\ \mu\text{m}$ and $c_l = 71.89\ \mu\text{m}$. Therefore, the DOF of FPGA-based SF-GD-OCM of the normal focal plane is $119.7\ \mu\text{m}$ in the air. The DOFs of other zones will be reported in chapter 4.



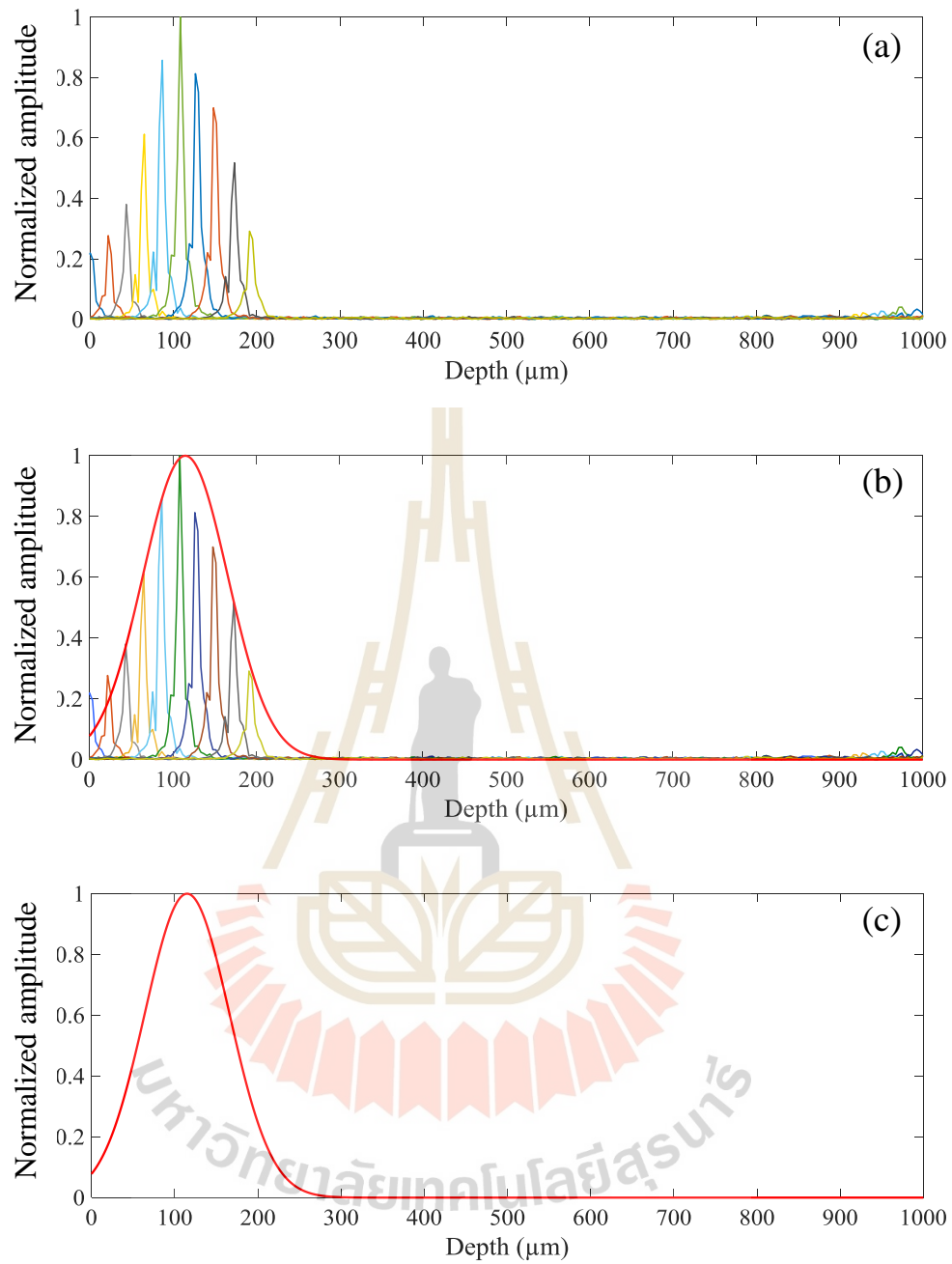


Figure 3.15 (a) Superposition of multiple depth profiles obtained at different positions in the air of the sample in micrometer. (b) Result of Gaussian fitting plotted over (a). (c) Gabor windows at the normal focal plane (43.12V to liquid lens driver) that corresponding to the center and width of DOF of zone 1.

CHAPTER IV

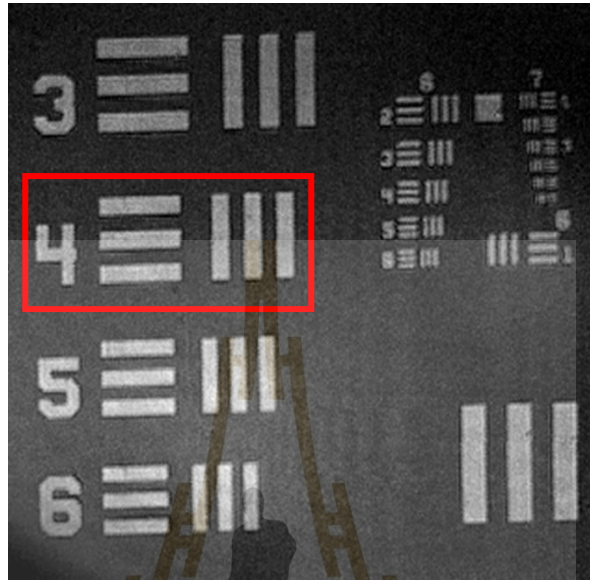
RESULTS AND DISCUSSION

4.1 Calibration of the scanning system

The calibration of the scanning system of FPGA-based SF-GD-OCM can be accomplished by taking a 3D image of a USAF1951 resolution target as shown in Figure 4.1(a). In our calibration, we applied a small voltage of 0.4V to the galvanometer mirror both on the x-axis and y-axis and determined the number of sampling points as a number of A-scans and B-scans of 500x500 pixels. To measure the response of the scanning length, we selected the 4th element of group +4 as marked by a red solid line box as shown in Figure 4.1(a). The spatial frequency of this group is 22.62 line pairs per millimeter as shown in Figure 4.1(b), which corresponds with one line pair in $\frac{1}{22.62}$ mm.

Besides, we measured the number of pixels per one line pair by plotting the intensity profile as shown in Figure 4.2(c) and Figure 4.2(d) for the x and y direction, respectively, as marked by a green solid line in Figure 4.2(a) and Figure 4.2(b), respectively. As a result, one line pair of the x-axis scanning was about 18 pixels and the y-axis scanning was about 17 pixels. Therefore, the pixel size in x and y directions were about 0.0025 mm and 0.0026 mm, respectively. Thus, the actual scanning distance for 500 pixels along the x and y directions is about 1.23 and 1.30 millimeters, respectively. Hence, we obtained the relation between voltage and scanning distance of

our scanning system. The scanning length of x and y directions were 0.325V per millimeter and 0.308V per millimeter, respectively.



(a)

Number of Line Pairs / mm in USAF Resolving Power Test Target 1951										
Element	Group Number									
	-2	-1	0	1	2	3	4	5	6	7
1	0.250	0.500	1.00	2.00	4.00	8.00	16.00	32.0	64.0	128.0
2	0.280	0.561	1.12	2.24	4.49	8.98	17.95	36.0	71.8	144.0
3	0.315	0.630	1.26	2.52	5.04	10.10	20.16	40.3	80.6	161.0
4	0.353	0.707	1.41	2.83	5.66	11.30	22.62	45.3	90.5	181.0
5	0.397	0.793	1.59	3.17	6.35	12.70	25.39	50.8	102.0	203.0
6	0.445	0.891	1.78	3.56	7.13	14.30	28.50	57.0	114.0	228.0

(b)

Figure 4.1 (a) *En face* image of resolution target acquired by the FPGA-based SF-GD-OCM and (b) the number of line-pairs per millimeter for each group. (Table source: <https://www.edmundoptics.com/f/1951-usaf-glass-slide-resolution-targets/12064/>)

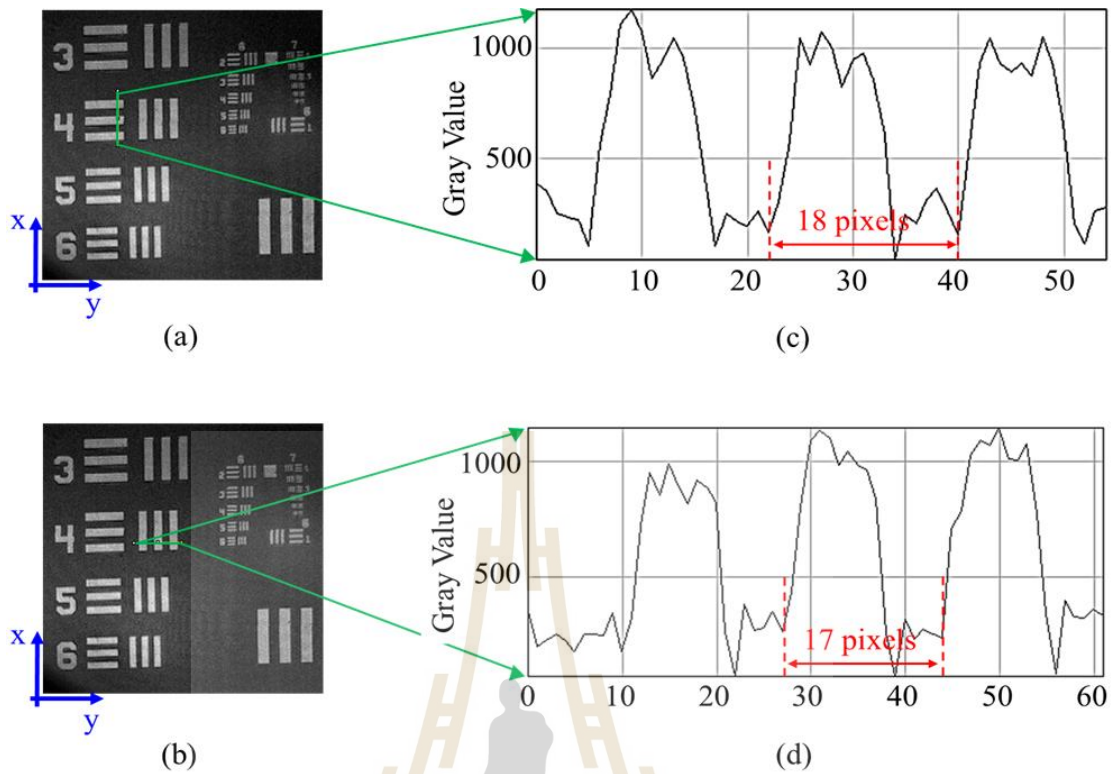


Figure 4.2 (a) and (b) are *en face* images of the resolution target acquired by the FPGA-based SF-GD-OCM, (c) the intensity profile along the x-direction, and (d) the intensity profile along the y-direction.

Four main tasks that are linear wavenumber interpolation, spectral filtering, spectral fusing, and fast Fourier transform (FFT) were implemented in the FPGA frame grabber device. For demonstration, A flow diagram of FPGA-based SF-GD-OCM imaging of seven focus zones is shown in Figure 4.3, i.e., seven datasets of raw spectra were acquired while the focal plane of the imaging lens was shifted for seven different depth locations by using the liquid lens.

The result of each task was measured as a throughput and FPGA resource usage. Throughput was computed by clock rate multiplied by the number of samples per clock cycle then divided by initiation interval,

$$\text{Throughput} = \frac{(\text{clock rate}) \times (\text{sample per clock cycle})}{(\text{initiation interval})}, \quad (4.1)$$

where the unit of throughput is samples per second, *clock rate* is the number of cycles per second, *sample per clock cycle* is the number of samples that the algorithm accepts per call, and *initiation interval* is the number of cycles before the algorithm can be called again.

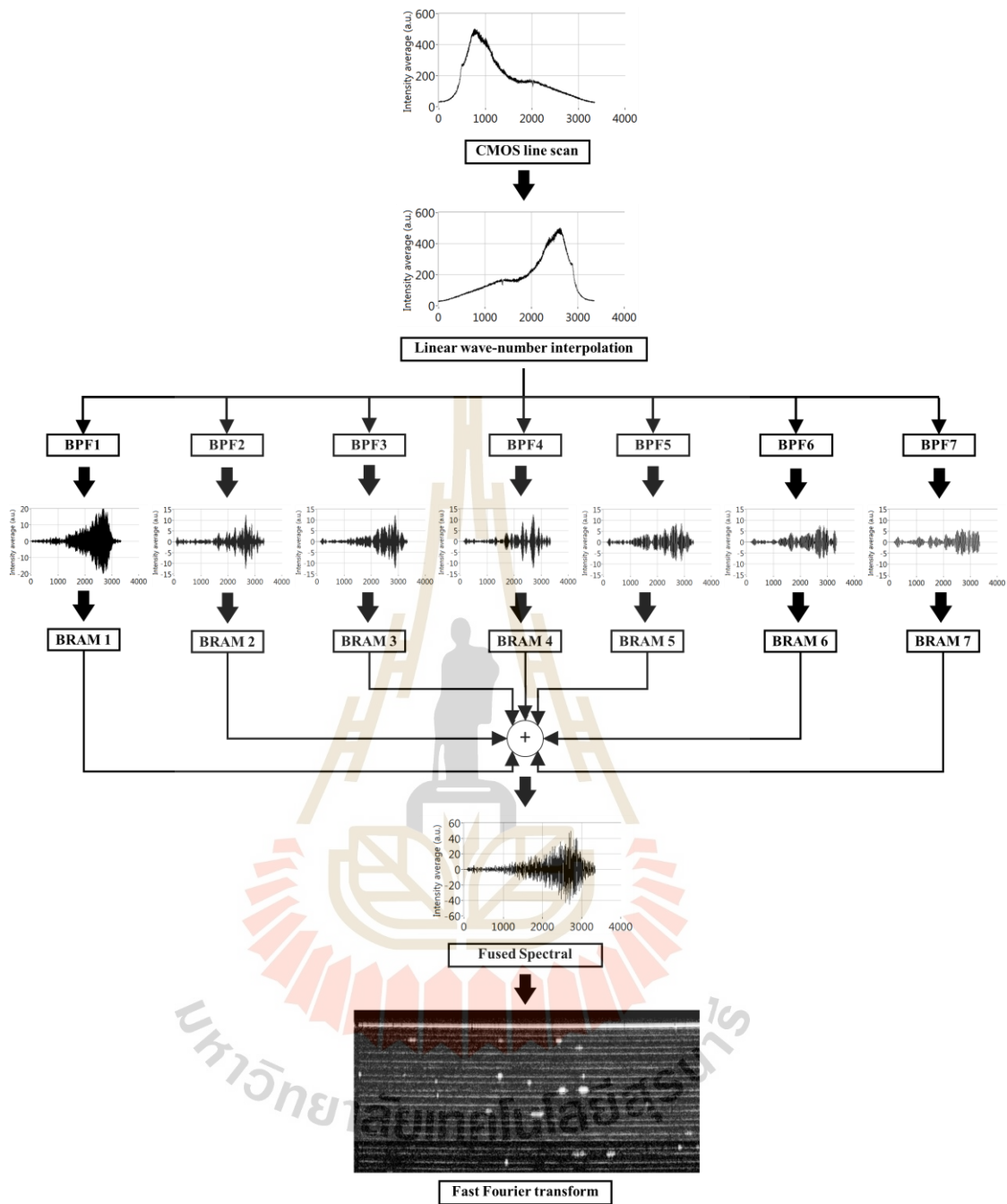


Figure 4.3 A flow diagram of the implementation of the FPGA-based SF-GD-OCM with the seven focus zones; BPF=the digital bandpass filter, BRAM=blocks of random-access memory.

4.2 Linear wavenumber interpolation

Linear wavenumber interpolation was implemented for the resampling of the interference signal from linear in wavelength to linear in wavenumber. We utilized the memory blocks for holding an incoming interference signal. A coefficient and an index position of linear wavenumber were pre-calculated and stored in look-up tables (LUTs). Linear wavenumber interpolation on LABVIEW FPGA was translated to HDL code. Then, HDL code was transformed into a logic element by the compiler. CLBs, look-up tables, flip-flops, and DSP were synthesized and mapped to an algorithm. The throughput of linear wavenumber interpolation was achieved at 160 Msamples per second with the usage of FPGA resources of 4610 CLBs, 11836 flip-flops, 12985 LUTs, 2 DSP slices, and 23 block RAMs. To verify the accuracy and the efficiency of linear wavenumber interpolation on the FPGA frame grabber, we used a stack of polymeric tapes as a sample and tuned the liquid lens to a flat surface, which was no power on the liquid lens (43.12V of liquid lens driver). Cross-sectional images of the same stack of polymeric tapes without and with performing linear wavenumber interpolation are shown in Figure 4.4(a) and Figure 4.4(b), respectively. The performance of linear wavenumber interpolation can be observed from the sharpness of the cross-sectional image of Figure 4.4(b), while Figure 4.4(a) is a blur cross-sectional image. Moreover, average depth profiles of Figure 4.4(a) and Figure 4.4(b) are shown in Figure 4.4(c) and Figure 4.4(d), respectively. The PSFs of transparent tape without performing linear wavenumber interpolation as shown in Figure 4.4(c) is broader as compared with that of without performing linear wavenumber interpolation as shown in Figure 4.4(d).

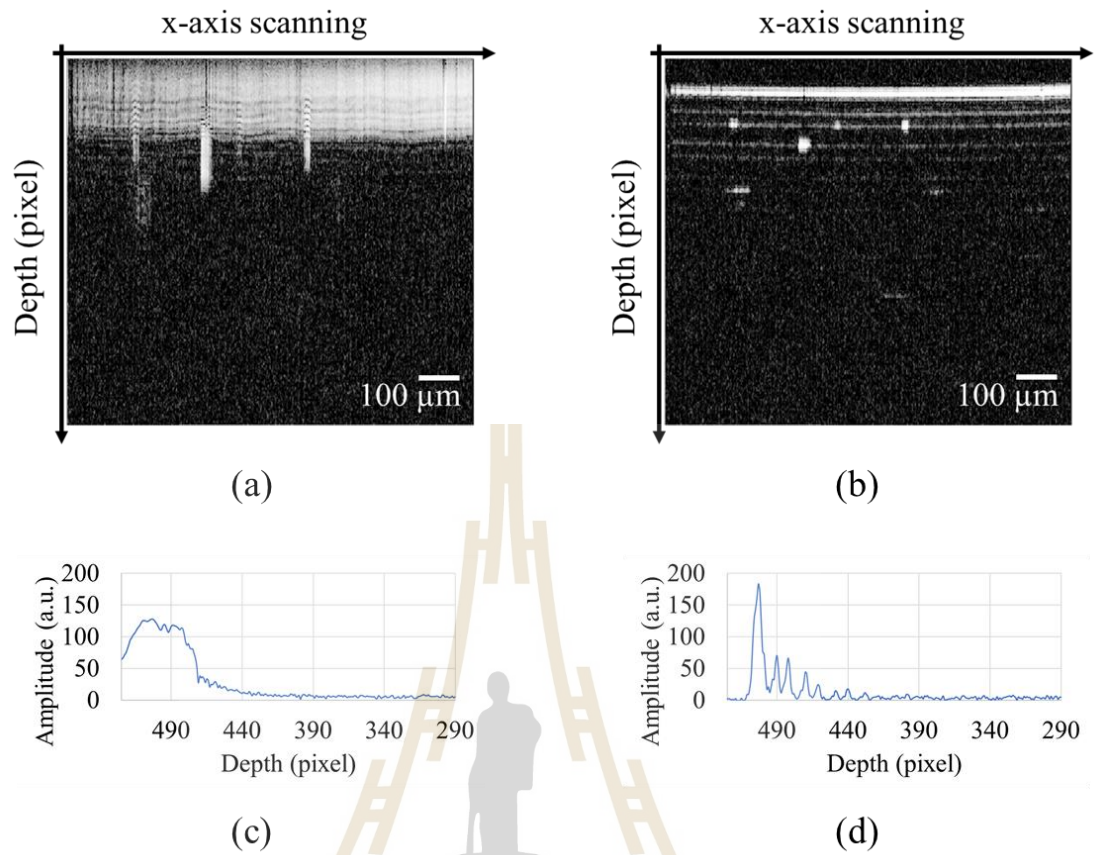


Figure 4.4 A cross-sectional image of a stack of polymeric tapes (a) without and (b) with performing linear wavenumber interpolation. (c) and (d) are represent an average depth profile of (a) and (b), respectively.

4.2 Spectral filtering

In our experiment, we translated the Gabor windows for 7 zones along the axial direction of a stacked of 10 layers of polymeric tapes, which was used as a sample. Therefore, the GD-OCM dataset consisted of 7 cross-sectional images were acquired over the same cross-section field-of-view as shown in Figure 4.5(a). Each bandpass filter was pre-determined to fit the actual DOF of each focusing of the GD-OCM dataset, corresponding with the center locations and widths of the Gabor windows. Moreover, each bandpass filter design i.e., magnitude response, phase response, and z-plane were reported in appendix II. The DC noise, and out-of-focus signal were removed after performing the bandpass filter as shown in Figure 4.5(b). To verify the performance of the digital bandpass filter in each focusing zone, we plotted an average depth profile of 7 zones without and with performing the digital bandpass filter as shown in Figure 4.6(a) and Figure 4.6(b), respectively. The amplitude of the vertical axis of the plot is normalized amplitude and the lateral axis is shown in frequencies. As a result, Figure 4.6(b) contains only in-focus spectra of the interference signal that is corresponding to the position of the Gabor window. The DC noise, and out-of-focus signal were removed as compared to Figure 4.6(a). The throughput of spectral filtering has been achieved at 80 Msamples per second with the usage of FPGA resources of 7900 CLBs, 15829 flip-flops, 24137 LUTs, 70 DSP slices, and 15 block RAMs.

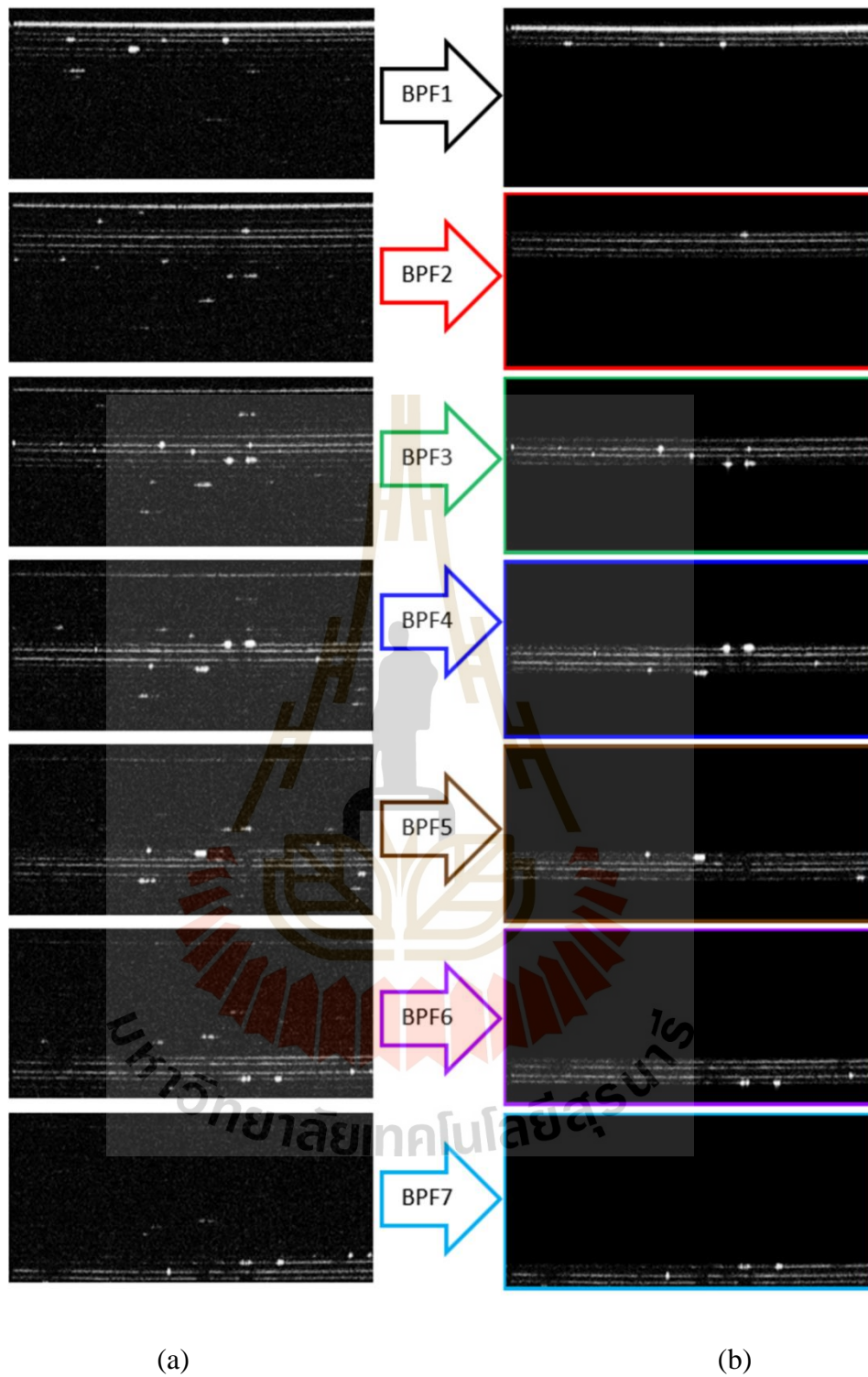


Figure 4.5 Cross-sectional images of a stack of polymeric tapes at different focus positions over the same cross-section field-of-view (a) before and (b) after performing the digital bandpass filter. BPF=the digital bandpass filter.

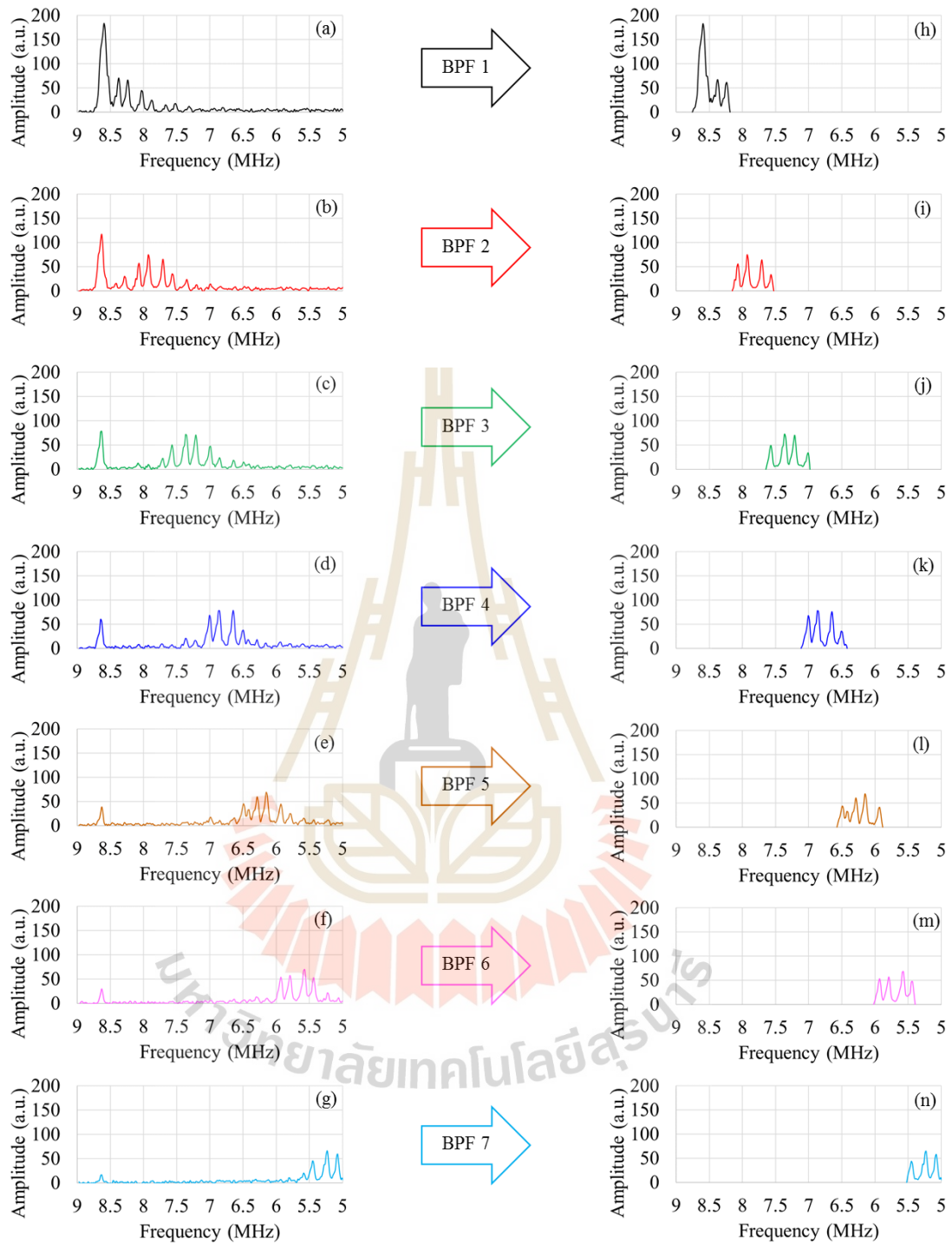


Figure 4.6 An average depth profiles versus frequency of a stack of polymeric tapes at different focus positions, (a-g) before and (h-n) after performing the digital bandpass filter. BPF=the digital bandpass filter.

4.3 Spectral fusing

Since the spectral filtering was designed to exactly fit the actual DOF of each focusing position, the spectral fusing of each GD-OCM dataset can be obtained by linear summation of all filtered spectra to obtain a final fused spectra. We performed overlaid plot of each depth profile of 7 zones without and with performing the digital bandpass filter as shown in Figure 4.7(a) and Figure 4.7(b), respectively. The fused depth cross-sectional image without and with performing digital bandpass filter is shown in Figure 4.7(e) and Figure 4.7(f), respectively. There are two ways to verify the accuracy of the fused image. The first way is by naked eyes, i.e., there is no overlap of each zone or missing of some information of each zone. For the second way, an average depth profile of the fused image can be used to check the unevenness of the intensity profile, i.e., abnormal rise or collapse of amplitude. Average depth profiles of Figure 4.7(e) and Figure 4.7(f) are shown in Figure 4.7(c) and Figure 4.7(d), respectively. Figure 4.7(d) shows the approximate flat top of amplitude on the transition region while Figure 4.7(c) shows the collapse of amplitude on some zones.

Figure 4.7(f) is a result of the performance of the digital bandpass filter that perfectly fits the actual DOF of each focusing position. Furthermore, it improves the quality and the sharpness of the fused depth cross-sectional image. The quality of the image in Figure 4.7(e) is poor because in-focus information was disturbed by out-of-focus information. In other words, the DOF effect alone is insufficient for suppressing out-of-focus spectral when displaying the final fused image on a logarithmic scale.

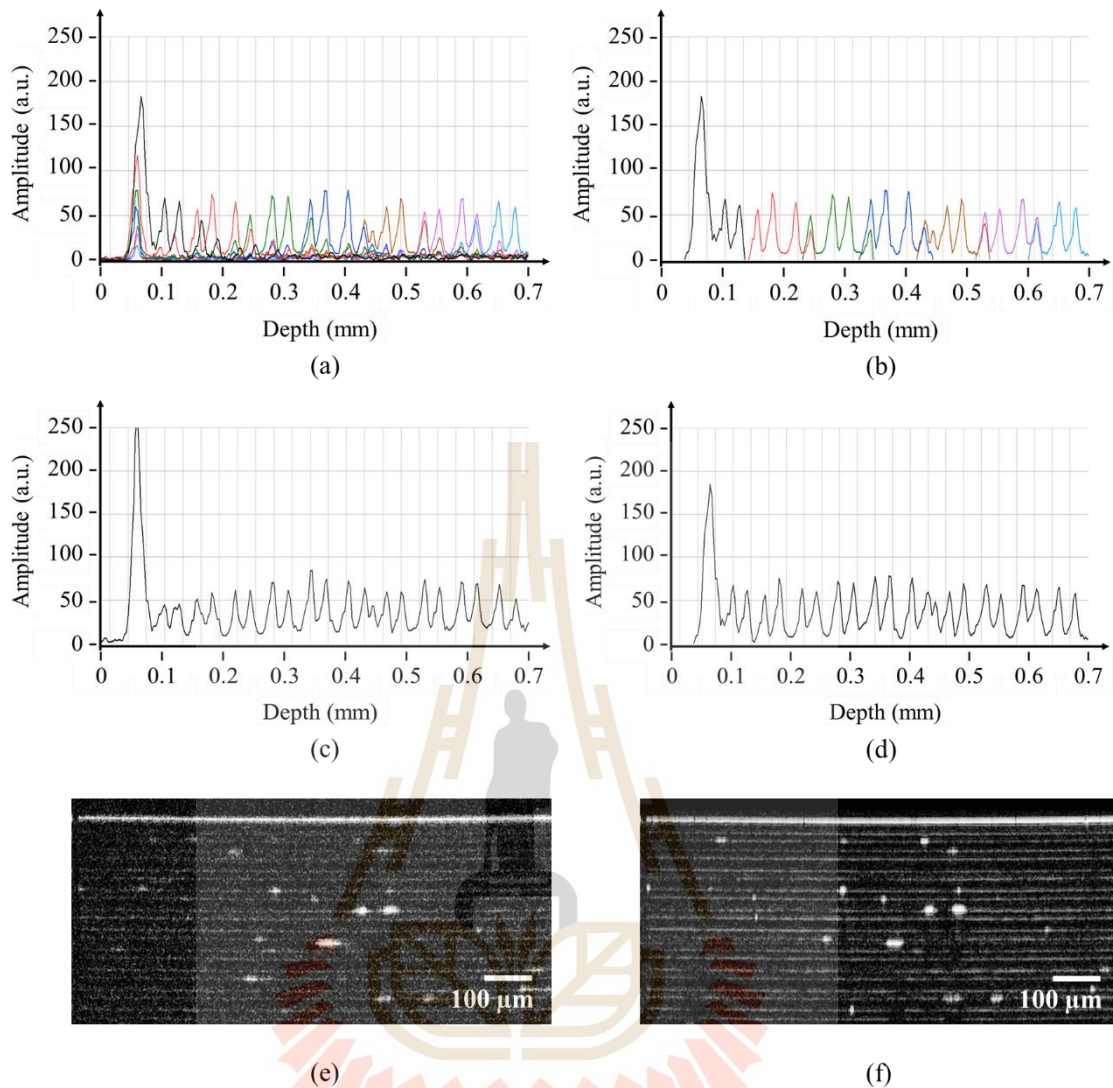


Figure 4.7 (a) and (b) are overlaid plots of the logarithmic-scale average intensity profiles along with the depth of the seven focus zones without and with performing the digital bandpass filter, respectively. (c) and (d) are the logarithmic-scale intensity profile obtained by FFT of the fused spectrum without and with performing the digital bandpass filter, respectively. (e) and (f) are cross-sectional images of the fused image without and with performing the digital bandpass filter, respectively.

Also, we compared the fused image of the spectral domain fusing with the conventional spatial domain fusing as shown in Figure 4.8. Figure 4.8(a) and Figure 4.8(b) show overlaid plots of the logarithmic-scale average intensity profile along with the depth of the seven focus zones of the spatial domain fusing and spectral domain fusing, respectively. Figure 4.8(c) and Figure 4.8(d) show the logarithmic-scale average intensity profile of the fused image obtained by the spatial domain fusing and spectral domain fusing, respectively. We found that the quality of the fused image in the spatial domain and spectral domain is approximately the same as shown in Figure 4.8(e) and Figure 4.8(f), respectively.

Moreover, the volumetric renderings of the three-dimensional fused image obtained by without performing the digital bandpass filter, FPGA-based SF-GD-OCM, and CPU-based spatial fusing GD-OCM, are shown in Figure 4.9(a), Figure 4.9(b), and Figure 4.9(c), respectively. Figure 4.9(a1-a3), Figure 4.9(b1-b3), and Figure 4.9(c1-c3) are *en face* images reconstructed from different depth positions of the three-dimensional data in Figure 4.9(a), Figure 4.9(b), and Figure 4.9(c), respectively. The effect of imperfect suppression of the Gabor window caused the ghost image as indicated by white arrows in Figure 4.9(a1-a3) when compared to Figure 4.9(b1-b2) and Figure 4.9(c1-c3). Furthermore, an example of cross-sectional images of the finger's nail fold at different focus positions over the same cross-section field-of-view are shown in Figure 10(a-d). Figure 10(e) is the fused image after performing FPGA-based SF-GD-OCM imaging.

The throughput of spectral fusing was achieved at 510 Msamples per second with the usage of FPGA resources of 3464 CLBs, 9870 flip-flops, 9702 LUTs, and 52 block RAMs.

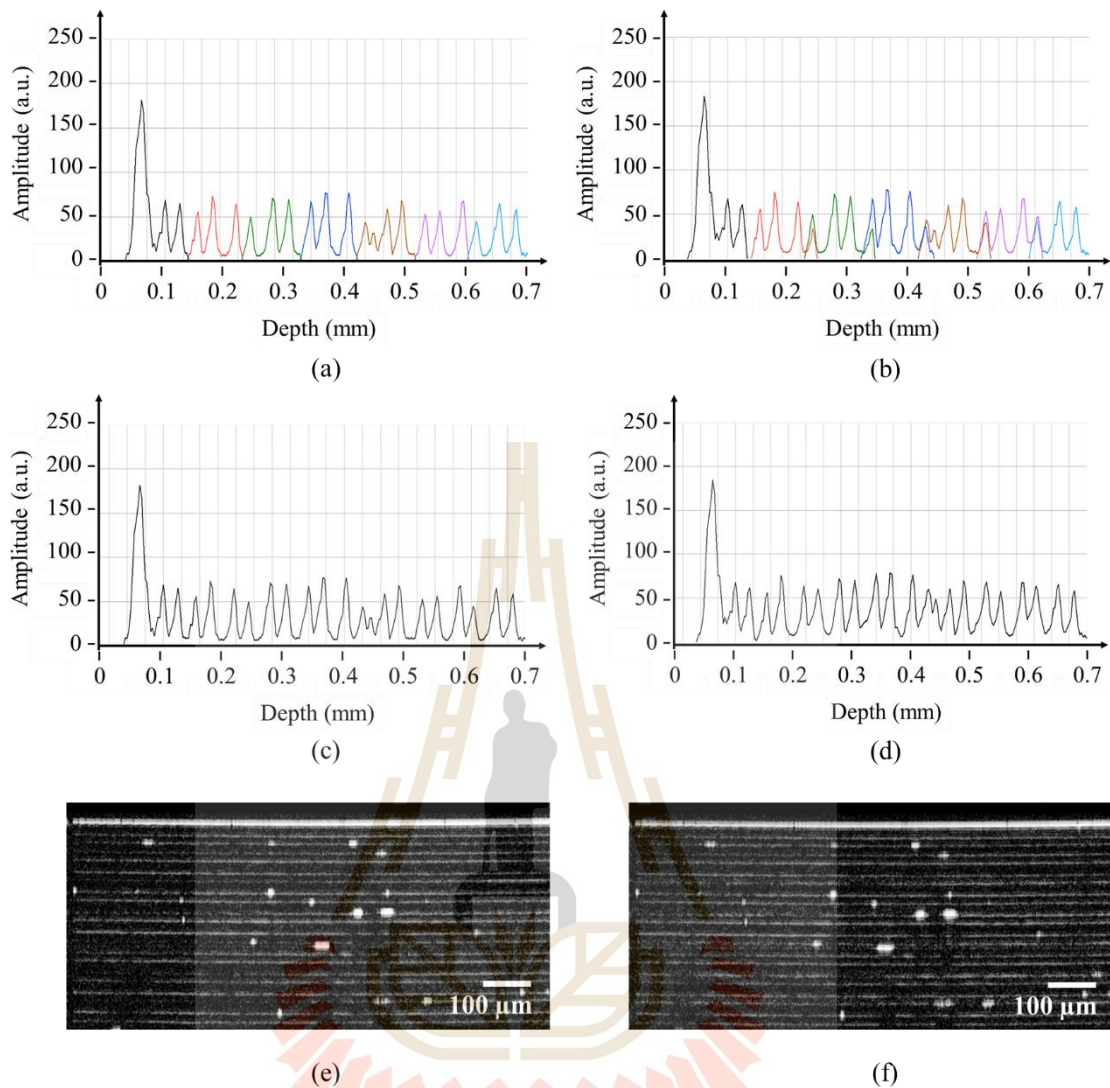


Figure 4.8 (a) and (b) are overlaid plots of the logarithmic-scale average intensity profile along with the depth of the seven focus zones obtained by spatial domain fusing and spectral domain fusing, respectively. (c) and (d) are the logarithmic-scale intensity profile obtained by FFT of the fused spectrum of the spatial domain fusing and spectral domain fusing, respectively. (e) and (f) are cross-sectional images of the fused image of spatial domain fusing and (f) spectral domain fusing, respectively.

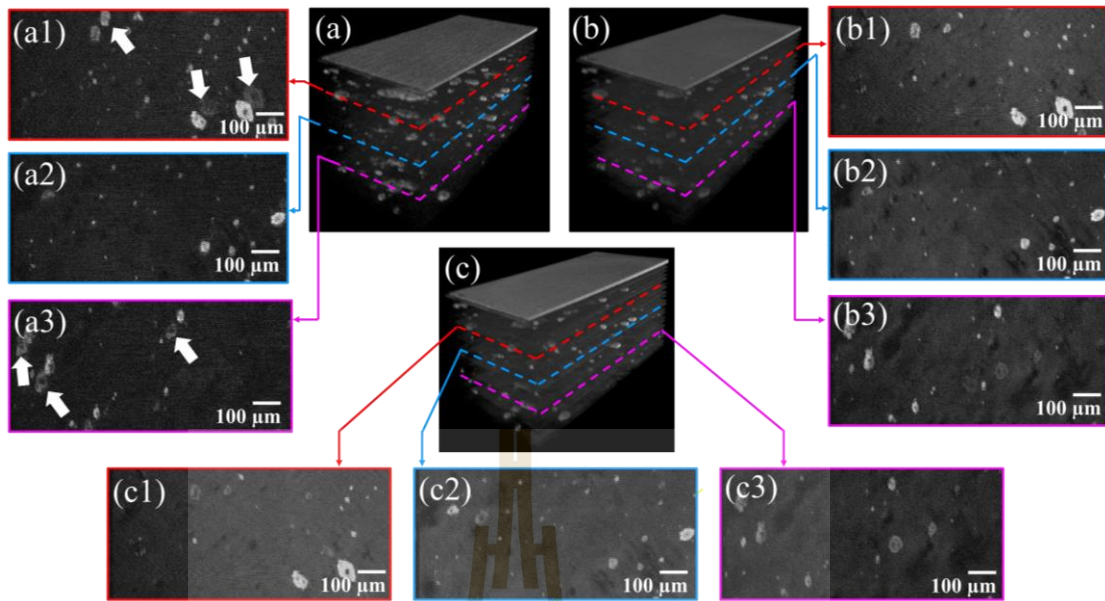


Figure 4.9 Volumetric rendering of the 3D fused data acquired by the developed SF-GD-OCM: (a) without and (b) with the application of the digital bandpass filter. (a1-a3) and (b1-b3) are *en face* images reconstructed at different depth locations from the 3D data sets in (a) and (b), respectively. (c) Volumetric rendering of the 3D fused data acquired by the spatial fusing GD-OCM. (c1-c3) are *en face* images reconstructed at different depth locations from the 3D data sets in (c).

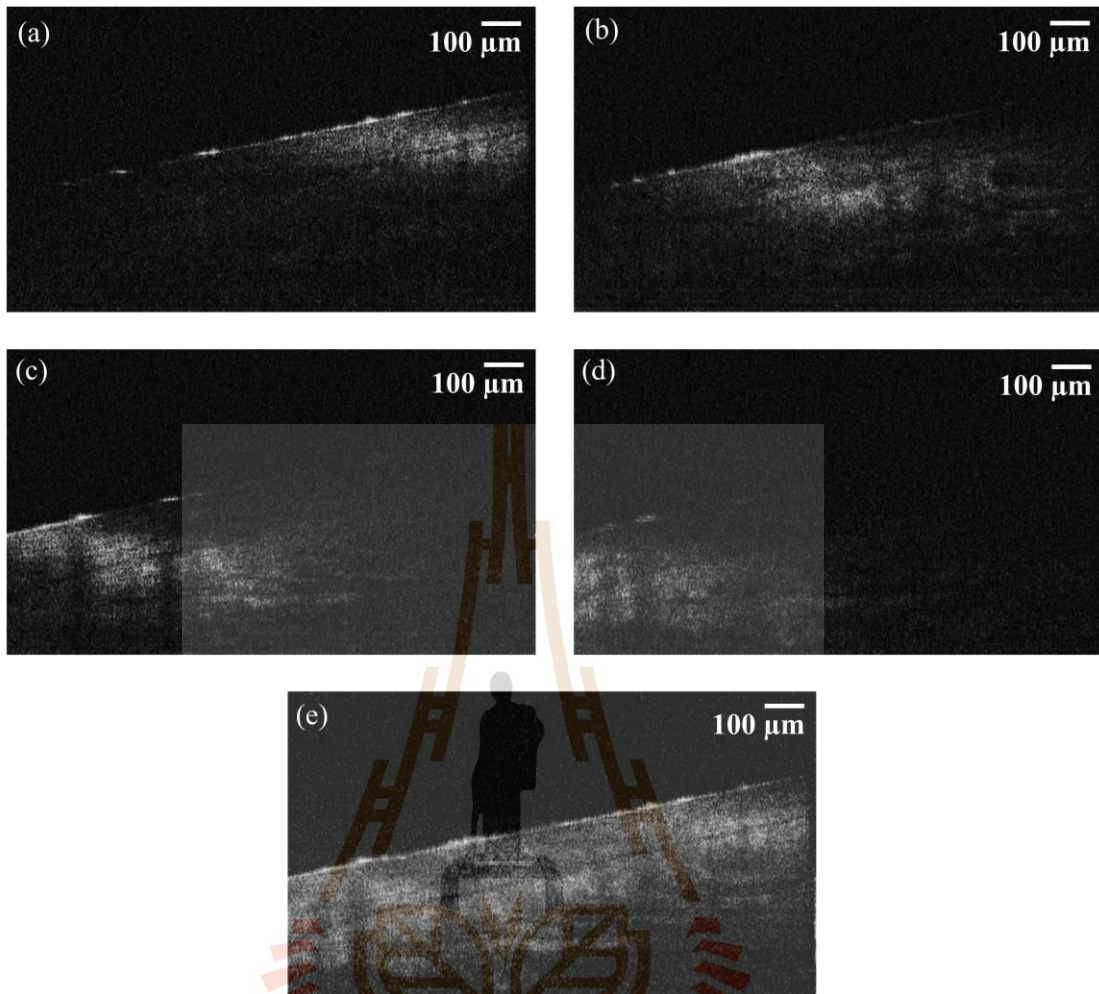


Figure 4.10 (a-d) An example of depth cross-sectional image of finger's nail fold at different focus positions, (e) the fused image of finger's nail fold from (a-d) that is performed by FPGA-based GD-OCM imaging.

Besides, we investigated the quality of the fused image with a different order of the filter. We used the pre-recorded tadpole dataset as an example. We found that the 10th, 8th, and 6th order filter can suppress out-of-focus spectra. In contrast, the 4th and 2nd order filter cannot suppress out-of-focus spectra as shown in Table 4.1. Furthermore, the quality image index of the fused image was used as a quality assessment with window size 128 (Z. Wang & Bovik, 2002). The quality image index value of 1 was

referred to as no difference between the perfect image and the test image while 0 represented the complete difference between the perfect image and the test image. We performed the CPU-based spectral fusing GD-OCM imaging of the tadpole sample with the same data type of the FPGA as the perfect image to be used as a reference as shown in Figure 4.11(a). The test images were obtained from the FPGA-based spectral fusing GD-OCM imaging with different order filters as shown in Figure 4.11(c-g). An image quality index of the fused image, throughput, and the resource usage of the FPGA were measured and reported as shown in Table 4.2. The 10th order filter provided the highest image quality index with the highest utilized resource of FPGA, while and the 6th order filter provided a lower image quality index with the lower utilized resource of FPGA that can still suppress out-of-focus spectra. The 10th, 8th, 6th, and 4th order filter provided the same throughput of 80 Msamples per second and the 2nd order filter gave throughput of 90 Msample per second. However, selecting an order of filters depends on the acceptable image quality index of the fused image and utilized resource of FPGA.

Table 4.1 Comparison of depth cross-sectional images of a tadpole at five different focus positions after performing different filters order of the digital bandpass filter.

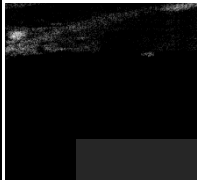
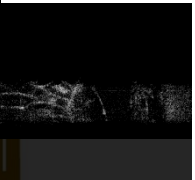
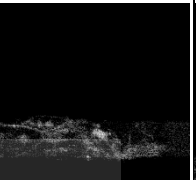
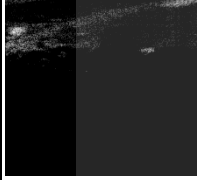
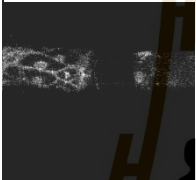
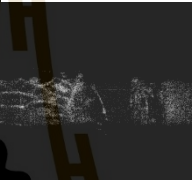
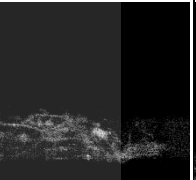
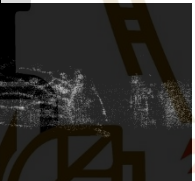
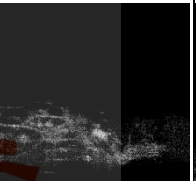
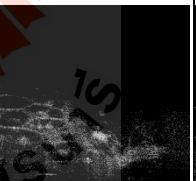
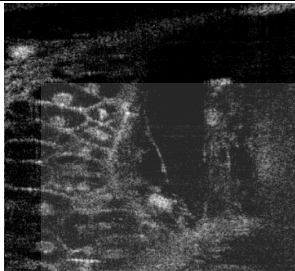
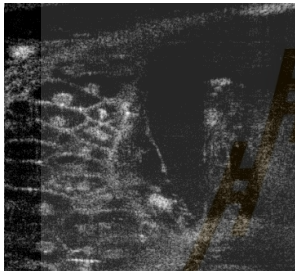
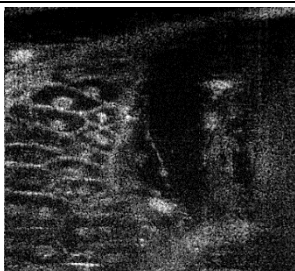
Order	Zone 1	Zone 2	Zone 3	Zone 4	Zone 5
10 th					
8 th					
6 th					
4 th					
2 nd					

Table 4.2 Comparison of an image quality index, throughput, and the resource usage of the FPGA of the fused image obtained by FPGA-based SF-GD-OCM with different filter orders.

Order	The fused image	Image quality index (window size 128)	Throughput and the resource usage
10 th		0.72	<p>Quick Device Utilization Estimate</p> <p>-----</p> <p>Slice Registers: 0.4% (414 out of 106400) Slice LUTs: 0.6% (309 out of 53200) DSP48s: 13.6% (30 out of 220) Block RAMs: 0.0% (0 out of 280)</p> <p>Quick Performance Estimate</p> <p>-----</p> <p>Clock rate (MHz): 83.06 Initiation interval (cycles): 1 Pipeline type: Fully pipelined Minimum latency: 9 Maximum latency: 9</p>
8 th		0.69	<p>Quick Device Utilization Estimate</p> <p>-----</p> <p>Slice Registers: 0.3% (330 out of 106400) Slice LUTs: 0.5% (251 out of 53200) DSP48s: 10.9% (24 out of 220) Block RAMs: 0.0% (0 out of 280)</p> <p>Quick Performance Estimate</p> <p>-----</p> <p>Clock rate (MHz): 83.06 Initiation interval (cycles): 1 Pipeline type: Fully pipelined Minimum latency: 7 Maximum latency: 7</p>
6 th		0.68	<p>Quick Device Utilization Estimate</p> <p>-----</p> <p>Slice Registers: 0.2% (248 out of 106400) Slice LUTs: 0.4% (193 out of 53200) DSP48s: 8.2% (18 out of 220) Block RAMs: 0.0% (0 out of 280)</p> <p>Quick Performance Estimate</p> <p>-----</p> <p>Clock rate (MHz): 83.06 Initiation interval (cycles): 1 Pipeline type: Fully pipelined Minimum latency: 5 Maximum latency: 5</p>
4 th		0.62	<p>Quick Device Utilization Estimate</p> <p>-----</p> <p>Slice Registers: 0.2% (162 out of 106400) Slice LUTs: 0.3% (135 out of 53200) DSP48s: 5.5% (12 out of 220) Block RAMs: 0.0% (0 out of 280)</p> <p>Quick Performance Estimate</p> <p>-----</p> <p>Clock rate (MHz): 83.06 Initiation interval (cycles): 1 Pipeline type: Fully pipelined Minimum latency: 3 Maximum latency: 3</p>
2 nd		0.52	<p>Quick Device Utilization Estimate</p> <p>-----</p> <p>Slice Registers: 0.1% (75 out of 106400) Slice LUTs: 0.1% (76 out of 53200) DSP48s: 2.7% (6 out of 220) Block RAMs: 0.0% (0 out of 280)</p> <p>Quick Performance Estimate</p> <p>-----</p> <p>Clock rate (MHz): 94.88 Initiation interval (cycles): 1 Pipeline type: Fully pipelined Minimum latency: 1 Maximum latency: 1</p>

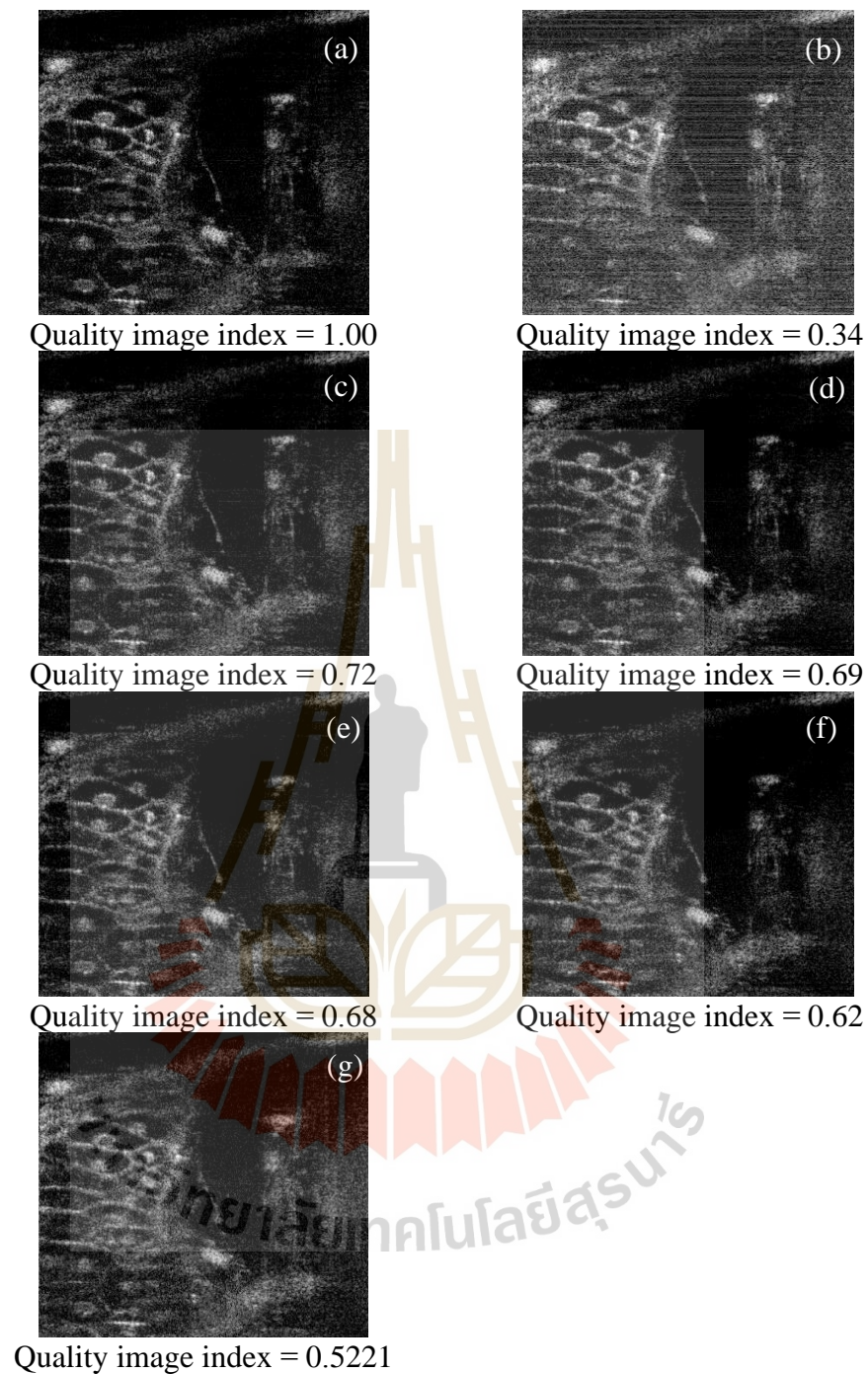


Figure 4.11 The image quality index of the fused image of a tadpole with (a) a perfect fused image, (b) the fused image without applying the digital bandpass filter, (c-g) the fused image after applying the digital bandpass filter of the 10th, 8th, 6th, 4th, and 2nd order, respectively.

4.4 Fast Fourier transform

FFT utilized the FPGA resources of 2566 CLBs, 8,839 flip-flops, 6,271 LUTs, 80 DSPs, and 48 block RAMs with a throughput of 89 Msamples per second. FFT required the largest number of FPGA resources for implementing complex algorithms. In our experiment, the processing time of FFT on the FPGA frame grabber device takes time longer than that of the CPU as reported in Table 4.3. Therefore, FFT performing in the FPGA frame grabber device can be considered optional for the FPGA-based SF-GD-OCM. One option is to transfer the fused spectrum to the CPU and then perform the FFT. Another option that was implemented in this study was performing FFT on the fused spectrum in the FPGA frame grabber device. The transformed signal was transferred to the host computer memory using direct access memory through the PCI express bus.

Table 4.3 Comparison of the processing times between FPGA-based SF-GD-OCM and CPU-based SF-GD-OCM in each process per spectrum.

Process	FPGA-based GD-OCM (μ s)		CPU-based GD-OCM (μ s)	
	Average	SD	Average	SD
Linear k interpolation	20.9	± 0.0	41.3	± 7.9
Spectral filtering (10 th order)	41.9	± 0.0	85.8	± 10.1
Spectral fusing	6.5	± 0.0	8.1	± 1.9
FFT (4096 points)	37.6	± 0.0	28.9	± 2.8
Total processing time	107.0	± 0.0	164.1	± 3.5

The throughput and the resource usage of the FPGA of each process of the FPGA-based SF-GD-OCM were reported in Table 4.4.

Table 4.4 Summary of the usage of FPGA resources in each process of the FPGA-based SF-GD-OCM.

Process	FPGA Resource Usage					Throughput (Msample/s)
	Total CLBs	Flip-Flops	LUTs	DSP Slices	Block RAMs	
Linear k interpolation	4,610	11,836	12,985	2	23	160
Spectral filtering	7,900	15,829	24,137	70	15	80
Spectral fusing	3,464	9,870	9,702	0	52	510
FFT	2,566	8,839	6,271	80	48	89

Nevertheless, it should be noted that the processing speed of CPU-based SF-GD-OCM may vary depending on the processing power of the host PC components, e.g., CPU, RAM, and GPU. Therefore, the purpose of the speed comparison experiment was only to verify that, under the same host PC, it is possible to perform several spectral processing algorithms in the FPGA frame grabber and achieve better processing speed performance. The processing speed of the FPGA-based SF-GD-OCM was determined by the number of clock cycles and therefore is governed by the internal clock speed of the FPGA device, which is independent of the processing power of the host computer. For verification, the virtual machine software was used to simulate a low resource

computer, i.e., the number of CPU cores and the amount of RAM were varied as shown in Table 4.5 and Table 4.6, respectively. We found that the processing speed of FPGA-based SF-GD-OCM was not dependent on the host PC performance. In contrary, the processing speed of CPU-based SF-GD-OCM was varied with the number of CPU cores on the host computer. In addition to the head-to-head speed improvement, the spectral processing in the FPGA greatly reduced hence the amount of data transfer between the frame grabber and the host computer and reduced the amount of data needed to be held by the host computer. This capability will allow the implementation of the FPGA-based SF-GD-OCM with lower specification and cost for the host computer

Table 4.5 Comparison of the processing times between FPGA-based SF-GD-OCM and vary the number of core processing of CPU-based SF-GD-OCM in each process per spectrum.

	Fixed ram to 2 GB, vary the number of CPU's cores				
	1 core	2 cores	4 cores	6 cores	8 cores
CPU-based SF-GD-OCM (μ s)	219.8	186.8	178.0	177.0	175.7
FPGA-based SF-GD-OCM (μ s)	107.0	107.0	107.0	107.0	107.0

Table 4.6 Comparison of the processing times between FPGA-based SF-GD-OCM and vary the amount of RAM of CPU-based SF-GD-OCM in each process per spectrum.

	Fixed CPU to 4 cores, vary the amount of RAM				
	2GB	4GB	6GB	8GB	10GB
CPU-based SF-GD-OCM (μ s)	178.0	177.3	173.9	177.0	176.3
FPGA-based SF-GD-OCM (μ s)	107.0	107.0	107.0	107.0	107.0

4.5 Performance of FPGA-based SF-GD-OCM system

The maximum imaging depth of OCT imaging is determined by the effect of the amplitude of an axial point spread function (PSF) is dropping about ten times as compared with the maximum amplitude. We applied voltage to the liquid lens driver to shift the focal plane in the range of 30V - 43V. We obtained the relation between the applied voltage to the liquid lens driver and the shifting zone. We measured the DOF at each applied voltage to the liquid lens driver as shown in Table 4.7. Moreover, each Gaussian fitting of each zone was reported in appendix III.

Table 4.7 The measured DOF of each focusing zone.

Zone	Gaussian equation = $a_1 e^{\left(\frac{x-b_1}{c_1}\right)^2}$			DOF (um)	Voltage*
	a1	b1	c1	= $2c_1\sqrt{\ln 2}$	
1	1	111	61.73	102.78	43.12
2	1	217.3	67.66	112.66	42.3
3	1	316.9	52.06	86.69	41.45
4	1	397.3	52.01	86.60	40.7
5	1	467.1	44.64	74.33	39.9
6	1	557.9	54.55	90.83	38.8
7	1	624.6	41.14	68.50	37.8
8	1	689.2	38.37	63.89	37
9	1	750.2	40.34	67.17	35.9
10	1	805.6	33.88	56.41	34.5
11	1	865.1	40.76	67.87	33.2
12	1	917	35.83	59.66	31.5
13	1	972.6	34.51	57.46	29.7

* Applied voltage to liquid lens driver

Furthermore, when the focal plane was shifted deeper in the sample. It causes degradation of the axial resolution as shown in Figure 4.12(c). Figure 4.12(c) shows the trend of the axial resolution becomes worse when the focal plane was shifted deeper in the sample. Therefore, we have developed a new method to reduce the broadening of

axial resolution throughout the sample. The coefficient of linear wavenumber interpolation was specifically pre-determined for each depth locations or zones. We refer to this method as “adaptive linear wavenumber interpolation”. The effectiveness of adaptive linear wavenumber interpolation is shown in Figure 4.13(c), where the axial resolution was maintained at about 8-9 μm . Comparison of the axial resolution without and with performing adaptive wavenumber interpolation is shown in Figure 4.14.

Besides, we measured the lateral resolution both in the x-direction and y-direction as shown in Figure 4.12(a-b) and Figure 4.13(a-b) for without and with performing adaptive wavenumber interpolation, respectively. Moreover, the DOF was measured without and with performing adaptive wavenumber interpolation as shown in 4.12(d) and Figure 4.13(d), respectively. Results show that performing adaptive wavenumber interpolation does not affect the lateral resolution and the DOF. The comparison of cross-sectional images of a stack of polymeric tapes without and with performing adaptive linear wavenumber interpolation is shown in Figure 4.15. The axial resolution of Figure 4.15(a) becomes worse when focusing deeper while the axial resolution of Figure 4.15(b) is approximately constant throughout the sample. An example of a biological sample at the cellular level cell with the field of view is 1 mm x 1 mm is shown in Figure 4.16.

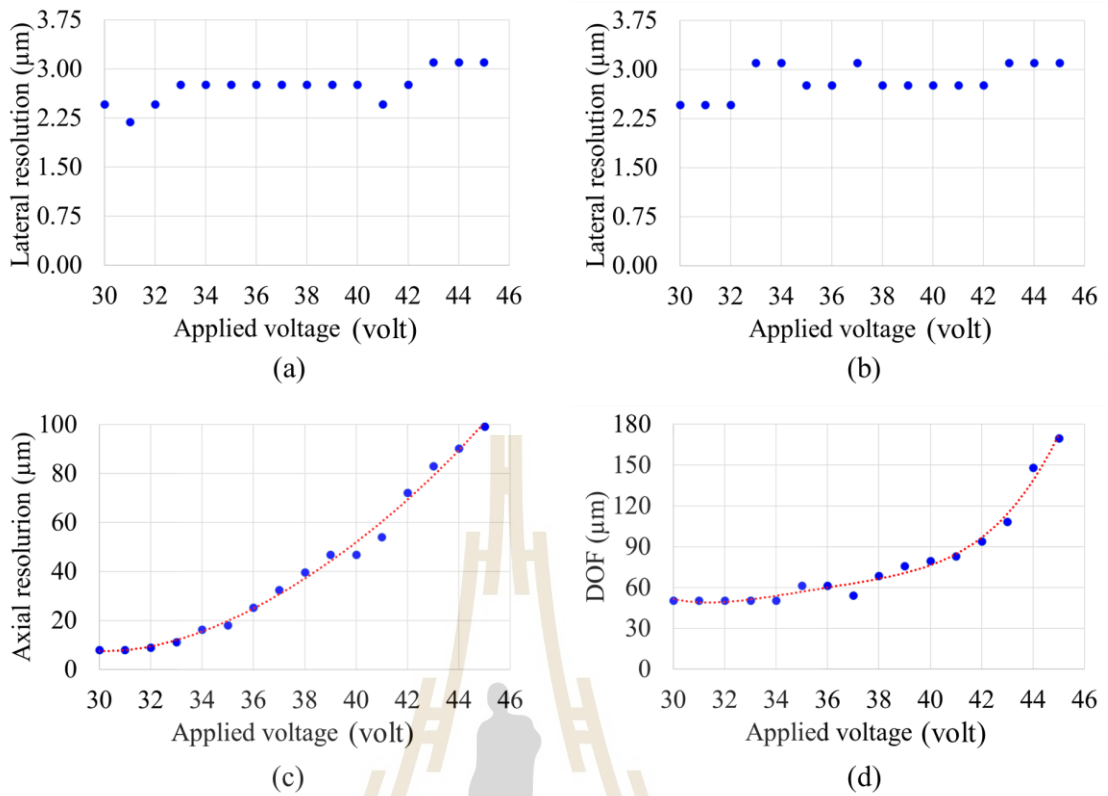


Figure 4.12 Plot of the lateral resolution in (a) x-direction, (b) y-direction, and (c) axial resolution, versus applied voltage. (d) A plot of the DOF measured at different focus depth locations when the applied voltage to the liquid lens driver was varied without performing adaptive linear wavenumber interpolation.

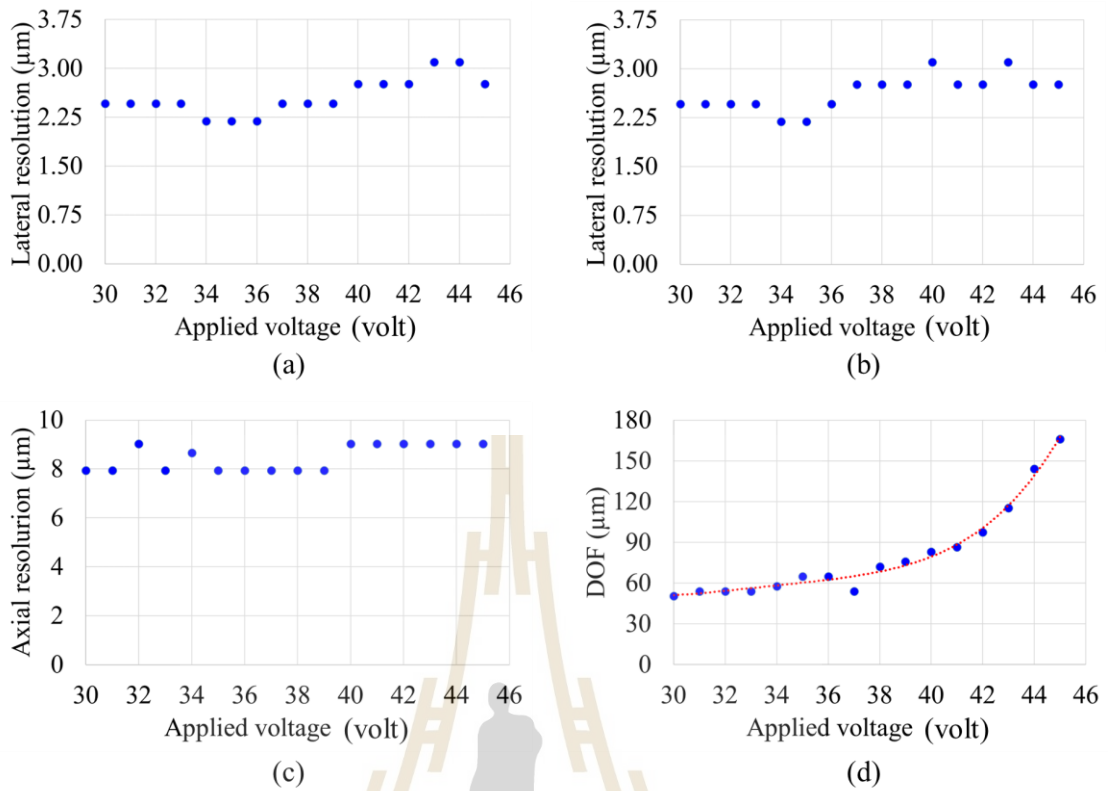


Figure 4.13 Plot of the lateral resolution in (a) x-direction, (b) y-direction, and (c) axial resolution, versus applied voltage. (d) A plot of the DOF measured at different focus depth locations when performing adaptive linear wavenumber interpolation.

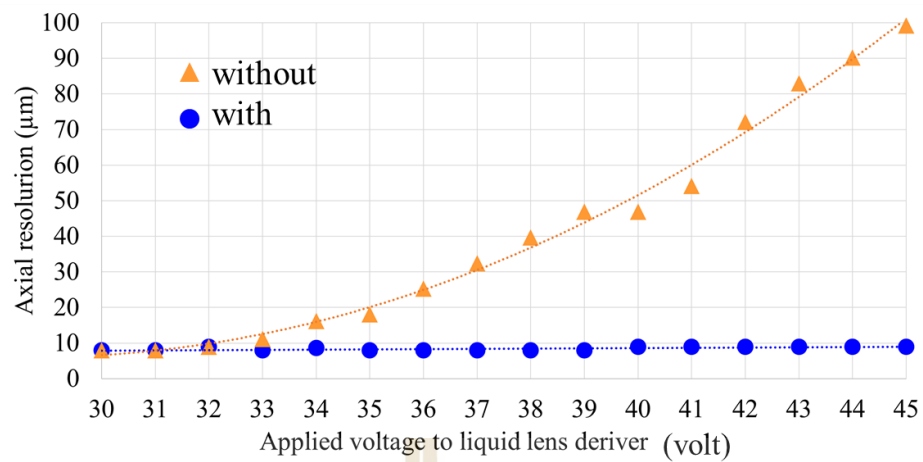


Figure 4.14 Comparison of the axial resolution of FPGA-based SF-GD-OCM without and with performing adaptive linear wavenumber interpolation.



Figure 4.15 FPGA-based SF-GD-OCM cross-sectional image of a stack of polymeric tapes (a) without and (b) with performing adaptive linear wavenumber interpolation.

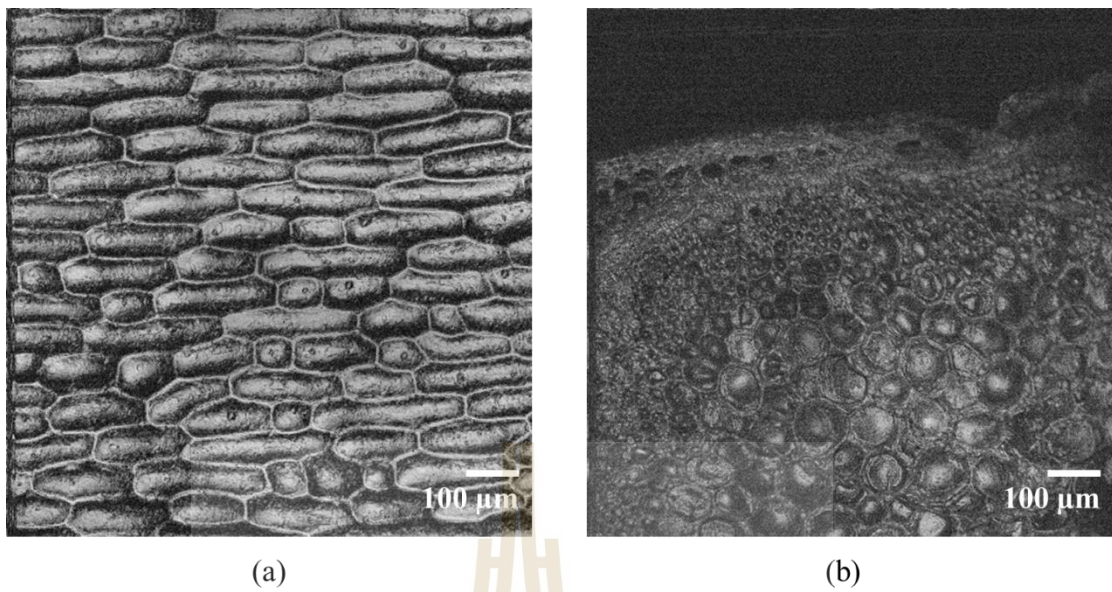


Figure 4.16 Example of FPGA-based SF-GD-OCM of a biological sample at the cellular level cell at the field of view is 1 mm x 1 mm of (a) onion cell and (b) trunk cell of *Peperomia pellucida*.

CHAPTER V

CONCLUSION

We have developed and experimentally implemented the spectral fusing algorithm of GD-OCM in an FPGA frame grabber device. The fusion image quality of the FPGA-based spectral fusing GD-OCM is comparable to the CPU-based spectral fusing GD-OCM, and the CPU-based spatial fusing GD-OCM, respectively. Four main processes of the spectral fusing GD-OCM algorithm: linear wave number interpolation, spectral filtering, spectral fusing, and FFT, were successfully implemented and verified.

The algorithm for the interpolation of the spectral interference signal from linear in wavelength to linear in wavenumber using a look-up table technique was successfully developed. Linear wavenumber interpolation is known to be mandatory for any implementation of frequency domain OCT and OCM to obtain the optimum depth resolution of the system. Furthermore, we have successfully developed a new method to correct the axial resolution of GD-OCM imaging throughout the sample by the implementation of linear wavenumber interpolation to fit with a different depth location or zone. Each set of coefficients of linear wavenumber interpolation was pre-determined to correspond with different depth locations or zone. We refer to this interpolated method as “adaptive linear wavenumber interpolation.”

For the algorithm for spectral filtering, in practice, the suppression of the out-of-focus spectral by the Gabor window alone cannot be sufficient when displaying the fused image on a logarithmic scale. This could lead to fusing artifacts, e.g., ghost images and nonuniform intensity at the transition. To address this issue, we applied a

digital bandpass filter on each acquired spectrum to further suppress the out-of-focus portions of the acquired interference signal. For the implementation of the spectral filtering, the Chebyshev IIR filter in the FPGA was successfully implemented to suppress the out-of-focus reflection. We found that the sixth order filter coefficient is the lowest order that can provide an adequate passed band for the DOF of 100 μm of the objective lens. However, the 10th order filter coefficient provides better fusion image quality and, hence, was implemented in the presented results. A higher-order will also work at the cost of longer processing times. The center and width of the passed band of each zone were manually determined so that the combination of the transition edge of two consecutive windows is a flat top response to prevent fusing artifacts.

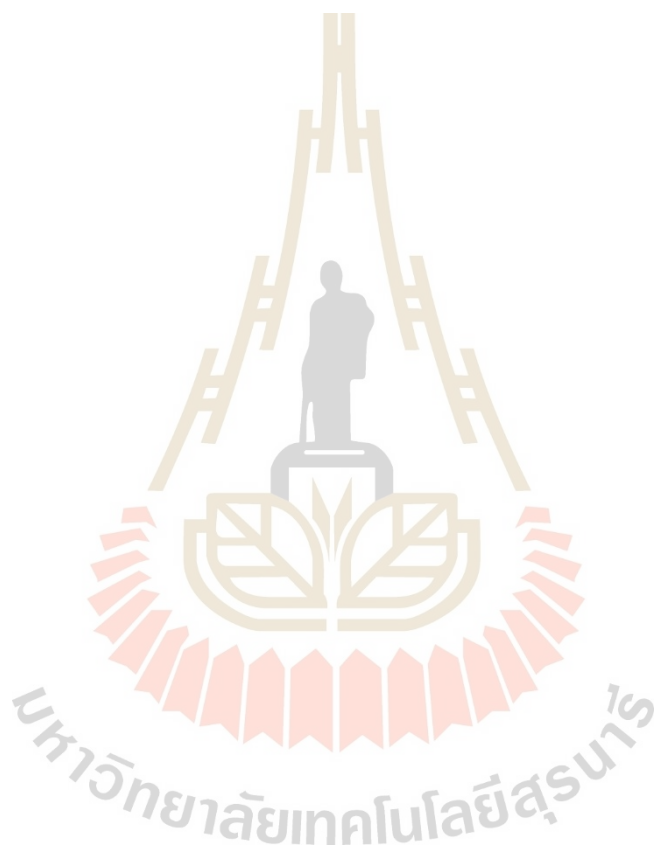
The resource usage of the FPGA was measured and reported, as shown in Table 4.4. The proposed technique of the FPGA-based spectral fusing GD-OCM shows an improved speed over that of the CPU-based spectral fusing GD-OCM. Furthermore, the hardware implementation of the processing algorithm using the FPGA-enabled frame grabber reduced the amount of data transfer to the host PC.

In comparison with GPU solution, GPU is suitable for post-processing such as that of the spatial fusing GD-OCM. The GPU-based processing of the spectral fusing GD-OCM is possible but not efficient since all raw spectra must be transferred to GPU memory, which will not address the bottleneck issue of data transfer speed between CPU and GPU. The true potential of the spectral fusing GD-OCM is the ability to perform focus extraction and fusing on raw spectra, which will reduce the amount of spectrum data that need to be transferred to the host computer and reduce the number of FFTs as compared with the spatial fusing GD-OCM that can be implemented on GPU.

In this work, the liquid lens was chosen for shifting the focal plane of the objective as shown in the diagram in Figure 3.1(a), which required about 200 ms to stabilize the focal shift position. Combining this with data capturing time per frame of the sensor, which was about 25 ms, the total time period for capturing one frame of data at each focus position was approximately 225 ms. From the results in Table 4.3, both the processing times of the CPU-based spectral fusing and the FPGA-based spectral fusing were faster than the data capturing a period of the implemented system. Therefore, to benefit from the speed improvement, the acquisition system of GD-OCM with a faster focus shifting technique needs to be implemented.

Furthermore, it should be pointed out that the implementation of FPGA-based spectral fusing GD-OCM on the specific hardware presented in this thesis, which is an off-the-shelf FPGA-enabled frame grabber, is only for early demonstration of the concept. For further optimized design, e.g., either for faster speed solution or lower-cost solution, a custom-developed FPGA frame grabber with more resources and faster clock speed should be implemented. In fact, the FPGA frame grabber device is just one possible hardware solution for the spectral fusing GD-OCM. The spectral fusing GD-OCM can also be implemented on swept-source-based GD-OCM by using FPGA enabled analog-to-digital device. Also, the processing speed of the FPGA-based SF-GD-OCM can be further improved by implementing the system that can acquire spectrum in linear wavenumber domain, e.g., a swept-source with linear-in-wavenumber output (H. Lee et al., 2020; Xi, Huo, Li, & Li, 2010) or linear-in-wavenumber spectrometer designs (Hu & Rollins, 2007; Lan & Li, 2017; Yoon, Bauer, Xu, Dorrer, & Rolland, 2019). Since the interference signal is linearity in the

wavenumber domain, linear wave number interpolation can be eliminated. Therefore, the FPGA-based SF-GD-OCM is promising for high-speed GD-OCM imaging.



REFERENCES

- Adie, S. G., Graf, B. W., Ahmad, A., Carney, P. S., & Boppart, S. A. (2012). Computational adaptive optics for broadband optical interferometric tomography of biological tissue. *Proceedings of the National Academy of Sciences*, *109*(19), 7175-7180.
- Aguirre, A., Hsiung, P., Ko, T., Hartl, I., & Fujimoto, J. (2003). High-resolution optical coherence microscopy for high-speed, in vivo cellular imaging. *Optics Letters*, *28*(21), 2064-2066.
- Barrett, H. H., & Myers, K. J. (2004). *Foundations of Image Science*: Wiley.
- Borkovkina, S., Camino, A., Janpongsri, W., Sarunic, M. V., & Jian, Y. (2020). Real-time retinal layer segmentation of OCT volumes with GPU accelerated inferencing using a compressed, low-latency neural network. *Biomedical optics express*, *11*(7), 3968-3984.
- Bouma, B. E., & Tearney, G. J. (2002). *Handbook of optical coherence tomography*: New York : Marcel Dekker.
- Canavesi, C., Cogliati, A., Mietus, A., Qi, Y., Schallek, J., Rolland, J. P., & Hindman, H. B. (2020). In vivo imaging of corneal nerves and cellular structures in mice with Gabor-domain optical coherence microscopy. *Biomedical optics express*, *11*(2), 711-724.
- Canavesi, C., & Rolland, J. (2019). Ten Years of Gabor-Domain Optical Coherence Microscopy. *Applied Sciences*, *9*, 2565. doi:10.3390/app9122565

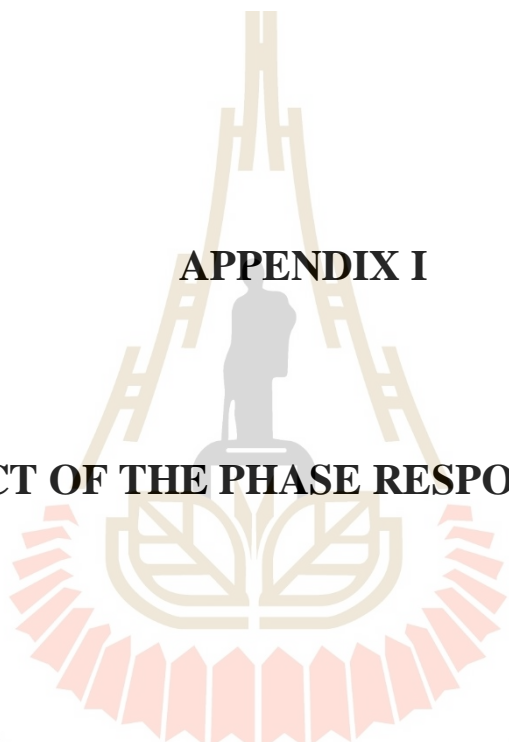
- Chugani, M. L., Samant, A. R., & Cerna, M. (1998). *LabVIEW signal processing*: Pearson Education.
- Cogliati, A., Canavesi, C., Hayes, A., Tankam, P., Duma, V.-F., Santhanam, A., . . . Rolland, J. P. (2016). MEMS-based handheld scanning probe with pre-shaped input signals for distortion-free images in Gabor-domain optical coherence microscopy. *Optics Express*, *24*(12), 13365-13374.
- Cua, M., Lee, S., Miao, D., Ju, M. J., Mackenzie, P. J., Jian, Y., & Sarunic, M. V. (2016). Retinal optical coherence tomography at 1 μm with dynamic focus control and axial motion tracking. *Journal of biomedical optics*, *21*(2), 026007.
- de Boer, J. F., Cense, B., Park, B. H., Pierce, M. C., Tearney, G. J., & Bouma, B. E. (2003). Improved signal-to-noise ratio in spectral-domain compared with time-domain optical coherence tomography. *Optics Letters*, *28*(21), 2067-2069. doi:10.1364/OL.28.002067
- Drexler, W., Liu, M., Kumar, A., Kamali, T., Unterhuber, A., & Leitgeb, R. A. (2014). Optical coherence tomography today: speed, contrast, and multimodality. *Journal of biomedical optics*, *19*(7), 071412.
- Fouquet, C., Gilles, J.-F., Heck, N., Dos Santos, M., Schwartzmann, R., Cannaya, V., . . . Bolte, S. (2015). Improving axial resolution in confocal microscopy with new high refractive index mounting media. *PloS one*, *10*(3), e0121096-e0121096. doi:10.1371/journal.pone.0121096
- Francis, M. (2009). Infinite impulse response filter structures in xilinx FPGAs. *Xilinx White Paper*.
- Hu, Z., & Rollins, A. M. (2007). Fourier domain optical coherence tomography with a linear-in-wavenumber spectrometer. *Optics Letters*, *32*(24), 3525-3527.

- Huang, D., Swanson, E., Lin, C., Schuman, J., Stinson, W., Chang, W., . . . et, a. (1991). Optical coherence tomography. *Science*, 254(5035), 1178-1181. doi:10.1126/science.1957169
- Huber, R., Wojtkowski, M., Fujimoto, J. G., Jiang, J., & Cable, A. (2005). Three-dimensional and C-mode OCT imaging with a compact, frequency swept laser source at 1300 nm. *Optics Express*, 13(26), 10523-10538.
- Izatt, J. A., Hee, M. R., Owen, G. M., Swanson, E. A., & Fujimoto, J. G. (1994). Optical coherence microscopy in scattering media. *Optics Letters*, 19(8), 590-592. doi:10.1364/OL.19.000590
- Kehtarnavaz, N., & Mahotra, S. (2010). *Digital Signal Processing Laboratory: LabVIEW-Based FPGA Implementation*: BrownWalker Press.
- Lan, G., & Li, G. (2017). Design of ak-space spectrometer for ultra-broad waveband spectral domain optical coherence tomography. *Scientific reports*, 7(1), 1-8.
- Lee, H., Kim, G. H., Villiger, M., Jang, H., Bouma, B. E., & Kim, C.-S. (2020). Linear-in-wavenumber actively-mode-locked wavelength-swept laser. *Optics Letters*, 45(19), 5327-5330.
- Lee, K.-S., Thompson, K. P., Meemon, P., & Rolland, J. P. (2011). Cellular resolution optical coherence microscopy with high acquisition speed for in-vivo human skin volumetric imaging. *Optics Letters*, 36(12), 2221-2223.
- Leitgeb, R., Hitzenberger, C. K., & Fercher, A. F. (2003). Performance of fourier domain vs. time domain optical coherence tomography. *Optics Express*, 11(8), 889-894. doi:10.1364/OE.11.000889
- Lenaphet, Y., & Meemon, P. (2020, 4-6 March 2020). *The implementation of digital filter on FPGA for the spectral fusing Gabor domain optical coherence*

- microscopy*. Paper presented at the 2020 8th International Electrical Engineering Congress (iEECON).
- Li, J., Sarunic, M. V., & Shannon, L. (2011). *Scalable, high performance Fourier domain optical coherence tomography: Why FPGAs and not GPGPUs*. Paper presented at the 2011 IEEE 19th Annual International Symposium on Field-Programmable Custom Computing Machines.
- Mahotra, S. (2010). *Digital Signal Processing Laboratory LabVIEW-Based FPGA Implementation*.
- Mathworks. (2016). Curve fitting toolbox: user's guide (R2016a).
- Meemon, P., Lenaphet, Y., & Saetiew, J. (2020). *FPGA implementation of spectral fusing Gabor domain optical coherence microscopy*. Paper presented at the Three-Dimensional and Multidimensional Microscopy: Image Acquisition and Processing XXVII.
- Meemon, P., Murali, S., Lee, K.-s., & Rolland, J. P. (2008, 2008/10/19). *Gabor Domain Optical Coherence Microscopy*. Paper presented at the Frontiers in Optics 2008/Laser Science XXIV/Plasmonics and Metamaterials/Optical Fabrication and Testing, Rochester, New York.
- Meemon, P., Palawong, K., & Pongchalee, P. (2014). *Simplified methods of design, implementation, and characterization of a spectrometer-based FD-OCT* (Vol. 8949): SPIE.
- Meemon, P., Widjaja, J., & Rolland, J. P. (2016). Spectral fusing Gabor domain optical coherence microscopy. *Optics Letters*, *41*(3), 508-511.

- Murali, S., Lee, K. S., & Rolland, J. P. (2007). Invariant resolution dynamic focus OCM based on liquid crystal lens. *Optics Express*, 15(24), 15854-15862. doi:10.1364/OE.15.015854
- Qi, B., Himmer, A. P., Gordon, L. M., Yang, X. V., Dickensheets, L. D., & Vitkin, I. A. (2004). Dynamic focus control in high-speed optical coherence tomography based on a microelectromechanical mirror. *Optics Communications*, 232(1-6), 123-128.
- Ralston, T. S., Marks, D. L., Carney, P. S., & Boppart, S. A. (2007). Interferometric synthetic aperture microscopy. *Nature Physics*, 3(2), 129-134.
- Rolland, J., Meemon, P., Murali, S., Thompson, K., & Lee, K. (2010). *Gabor domain optical coherence microscopy* (Vol. 7556): SPIE.
- Rolland, J. P., Meemon, P., Murali, S., Kaya, I., Papp, N., Thompson, K. P., Bouma, B. (2009, 2009/06/14). *Gabor Domain Optical Coherence Microscopy*. Paper presented at the Optical Coherence Tomography and Coherence Techniques IV, Munich.
- Rolland, J. P., Meemon, P., Murali, S., Thompson, K. P., & Lee, K.-s. (2010). Gabor-based fusion technique for Optical Coherence Microscopy. *Optics Express*, 18(4), 3632-3642. doi:10.1364/OE.18.003632
- Sundararajan, P. (2010). High Performance Computing Using FPGAs.
- Tankam, P., He, Z., Chu, Y.-J., Won, J., Canavesi, C., Lepine, T., . Thuret, G. (2015). Assessing microstructures of the cornea with Gabor-domain optical coherence microscopy: pathway for corneal physiology and diseases. *Optics Letters*, 40(6), 1113-1116.

- Ustun, T. E., Iftimia, N. V., Ferguson, R. D., & Hammer, D. X. (2008). Real-time processing for Fourier domain optical coherence tomography using a field programmable gate array. *Review of Scientific Instruments*, 79(11), 114301.
- Van de Vegte, J. (2008). *Fundamentals of Digital Signal Processing*: Pearson Education Taiwan.
- Wang, L., & Wu, H. I. (2007). *Biomedical Optics: Principles and Imaging*.
- Wang, Z., & Bovik, A. C. (2002). A universal image quality index. *IEEE signal processing letters*, 9(3), 81-84.
- Watanabe, Y., Maeno, S., Aoshima, K., Hasegawa, H., & Koseki, H. (2010). Real-time processing for full-range Fourier-domain optical-coherence tomography with zero-filling interpolation using multiple graphic processing units. *Applied Optics*, 49(25), 4756-4762. doi:10.1364/AO.49.004756
- Xi, J., Huo, L., Li, J., & Li, X. (2010). Generic real-time uniform K-space sampling method for high-speed swept-Source optical coherence tomography. *Optics Express*, 18(9), 9511-9517.
- Yoon, C., Bauer, A., Xu, D., Dorrer, C., & Rolland, J. P. (2019). Absolute linear-in-k spectrometer designs enabled by freeform optics. *Optics Express*, 27(24), 34593-34602.



APPENDIX I

THE EFFECT OF THE PHASE RESPONSE OF FILTER

มหาวิทยาลัยเทคโนโลยีสุรนารี

The effect of the phase response of filter

To verify the effect of the phase of filter, a mirror was used as a sample to obtain only one peak of amplitude, which allowed for observation of the phase of the spectral interference signal after performing FFT. The spectral interference signal after performing FFT was a complex number, which can be represented in a simple form as

$$\hat{Z} = Ae^{j\theta} , \quad (6.1)$$

where \hat{Z} is the complex number, A is an amplitude of the complex number, and θ is the phase of the complex number. Alternatively, the complex number can be expressed as

$$\hat{Z} = a + bj , \quad (6.2)$$

where a is a real part of the complex number, and b is an imaginary part of the complex number. Here, an amplitude, phase, and a real part of the spectral interference signal after performing FFT versus frequency are shown in Figure 6.1(a), Figure 6.1(b), and Figure 6.1(c), respectively.

As observed from Figure 6.1(a), the AC noise was about in the range of lower than 0.4 MHz and higher than 0.7 MHz. The filter designing to suppress the noise of the spectral interference signal of a mirror was shown in Table 6. The frequency response, phase response, and complex plane of the filter design are shown in Figure 6.2(a), Figure 6.2(b), and Figure 6.2(c), respectively.

The result shows that an amplitude of the interference signal was not modified by the bandpass filter as shown in Figure 6.3(a). Moreover, the noise signal was

suppressed as observed from an orange line in Figure 6.3(a). The phase of interference signal was shifted by the filter as shown in Figure 6.3(b). A real part of FFT of the spectral interference signal was altered by the phase response of filter as shown in Figure 6.3(c). Nevertheless, the FPGA-based SF-GD-OCM imaging used only the amplitude of the spectral interference signal to reconstruct the image. Thus, the phase alteration of the spectral interference signal after performing FFT has not affected the structural image of FPGA-based SF-GD-OCM.

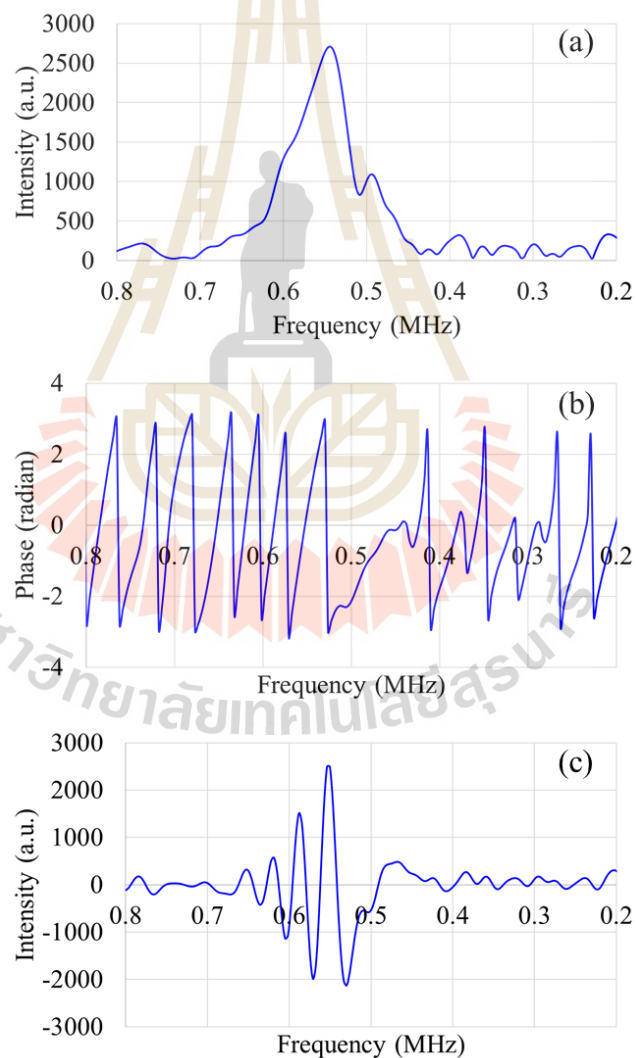


Figure 6.1 (a) An amplitude, (b) a phase, and (c) a real part of the interference signal of a mirror versus frequency after performing FFT.

Table 6 The filter specification to suppress the noise of the interference signal by using a plane mirror as a sample.

Filter type	Bandpass filter
Design method	IIR with Chebyshev Type I
Sampling frequency	70 MHz
High cut-off frequency	0.7 MHz
Low cut-off frequency	0.4 MHz
Order	10
Bandpass ripple	0.1 dB
Filter structure	Cascaded second-order section form II

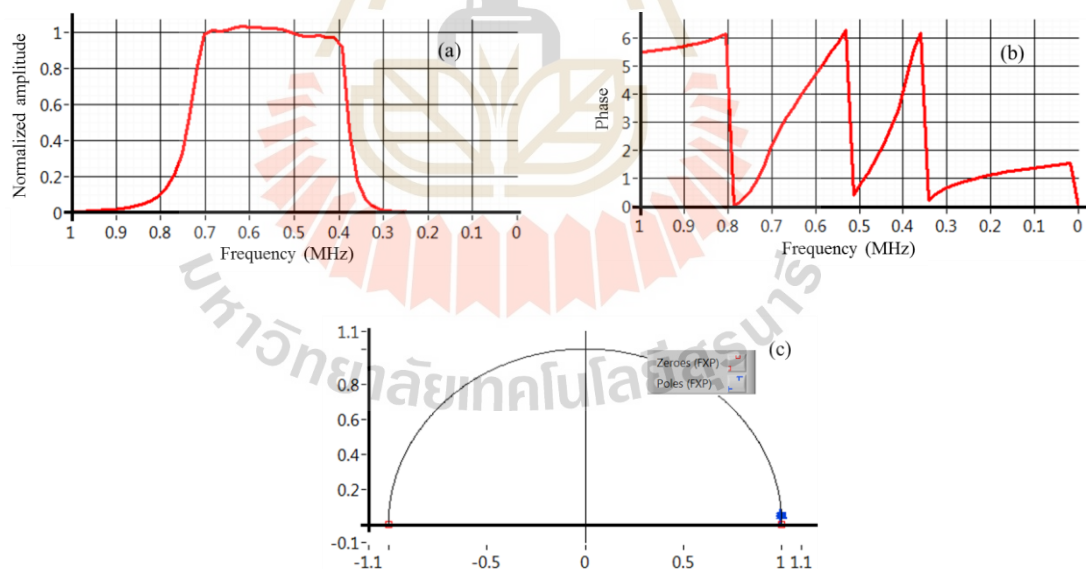


Figure 6.2 (a) is the frequency response, (b) is phase response, and (c) z-plane of filter design to suppress the noise of the spectral interference signal of a mirror.

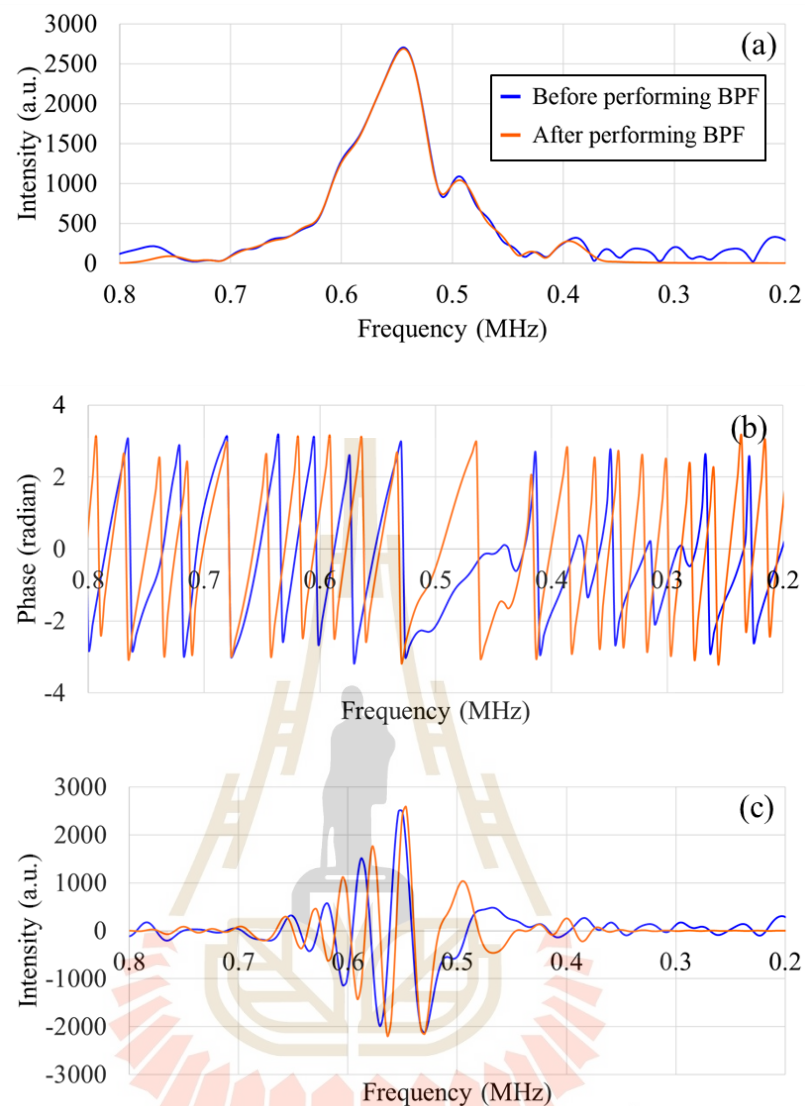
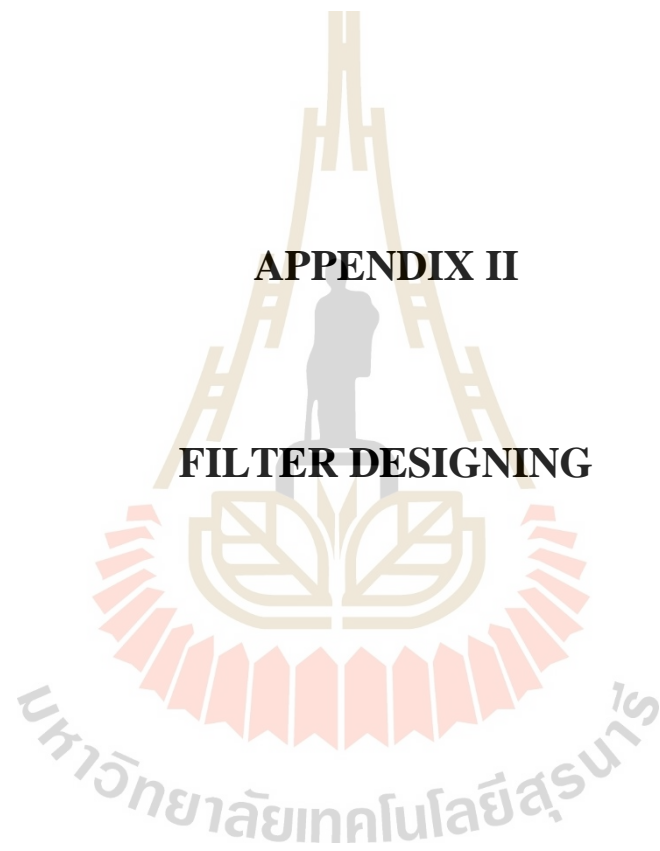


Figure 6.3 (a) An amplitude, (b) the phase, and (c) a real part of FFT of the spectral interference signal of a mirror as overlaid plots between before and after performing the digital bandpass filter as designated by a blue line and orange line, respectively. BPF = the digital bandpass filter.

APPENDIX II

FILTER DESIGNING



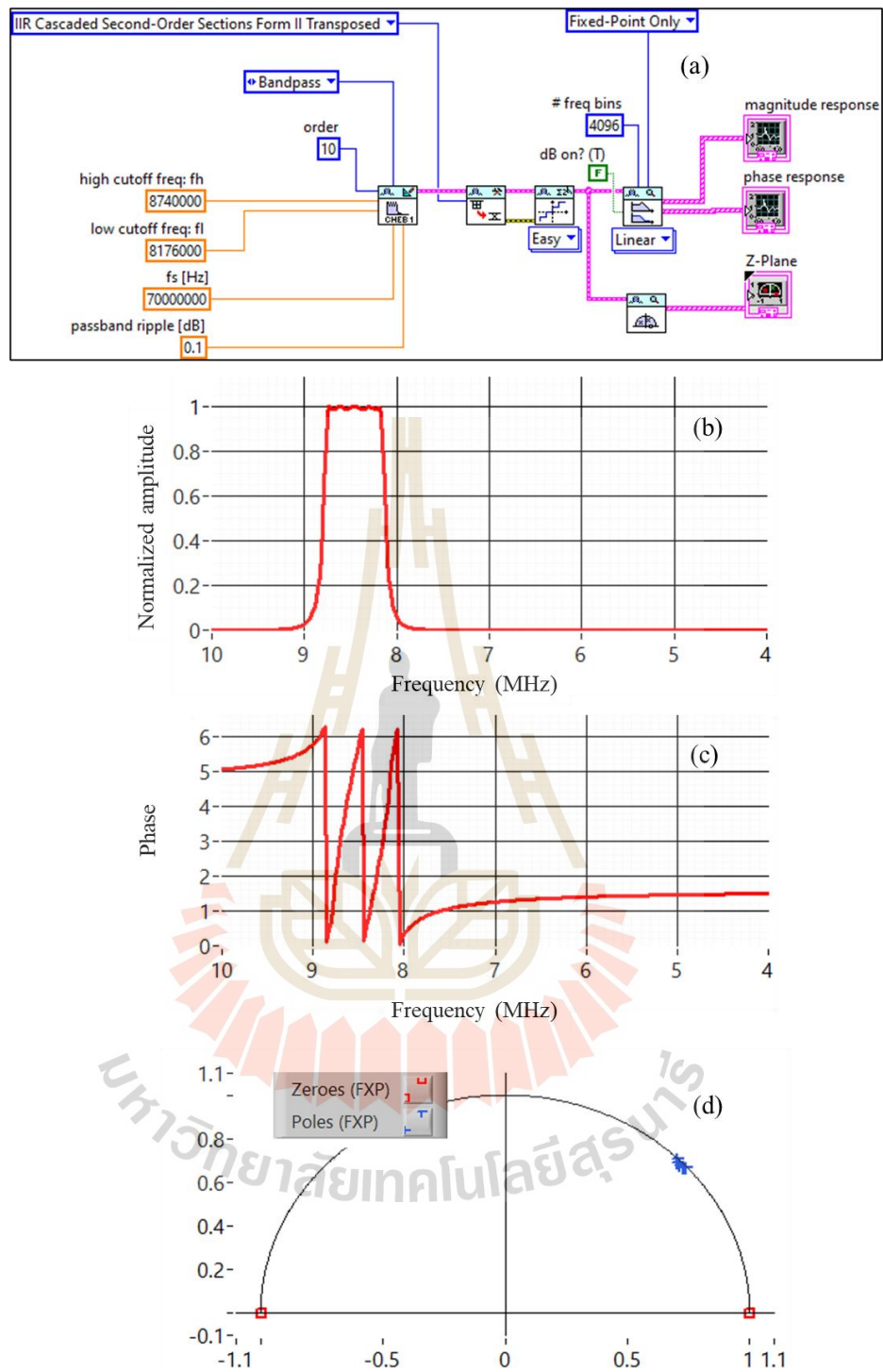


Figure 6.4 (a) is filter programming, (b) is magnitude response, (c) is phase response, and (d) is the z-plane of filter designing for zone 1.

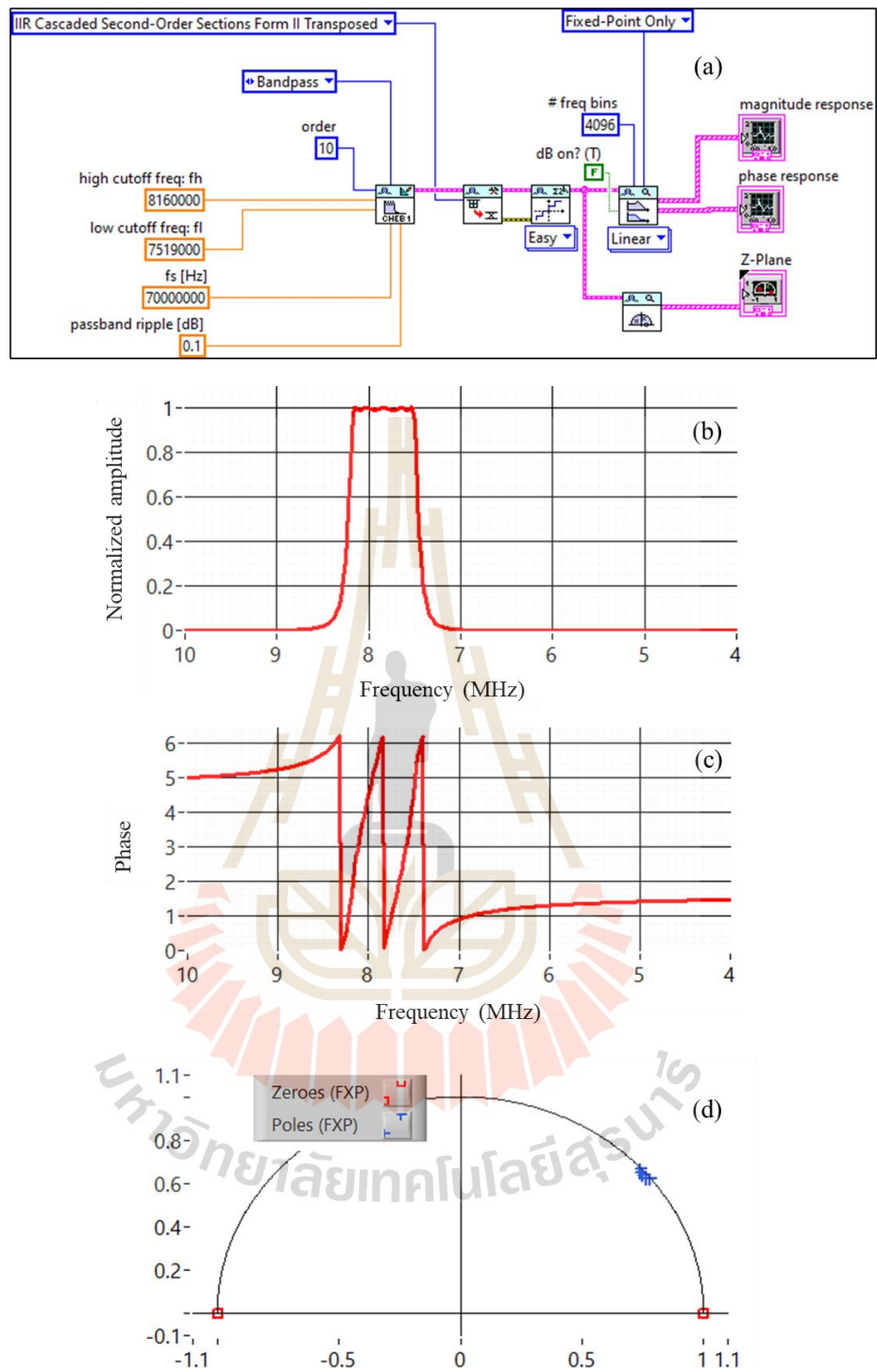


Figure 6.5 (a) is filter programming, (b) is magnitude response, (c) is phase response, and (d) is the z-plane of filter designing for zone 2.

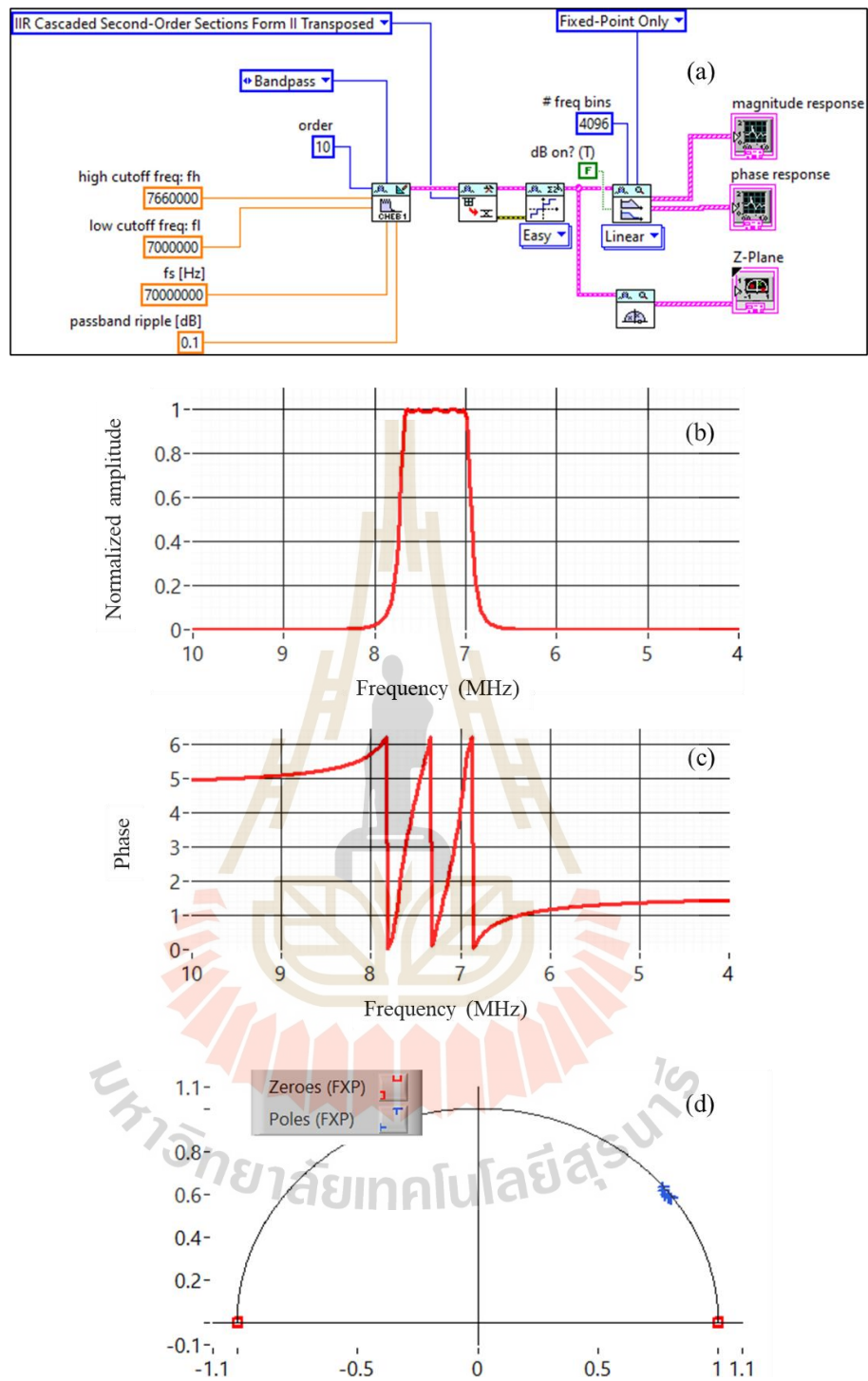


Figure 6.6 (a) is filter programming, (b) is magnitude response, (c) is phase response, and (d) is the z-plane of filter designing for zone 3.

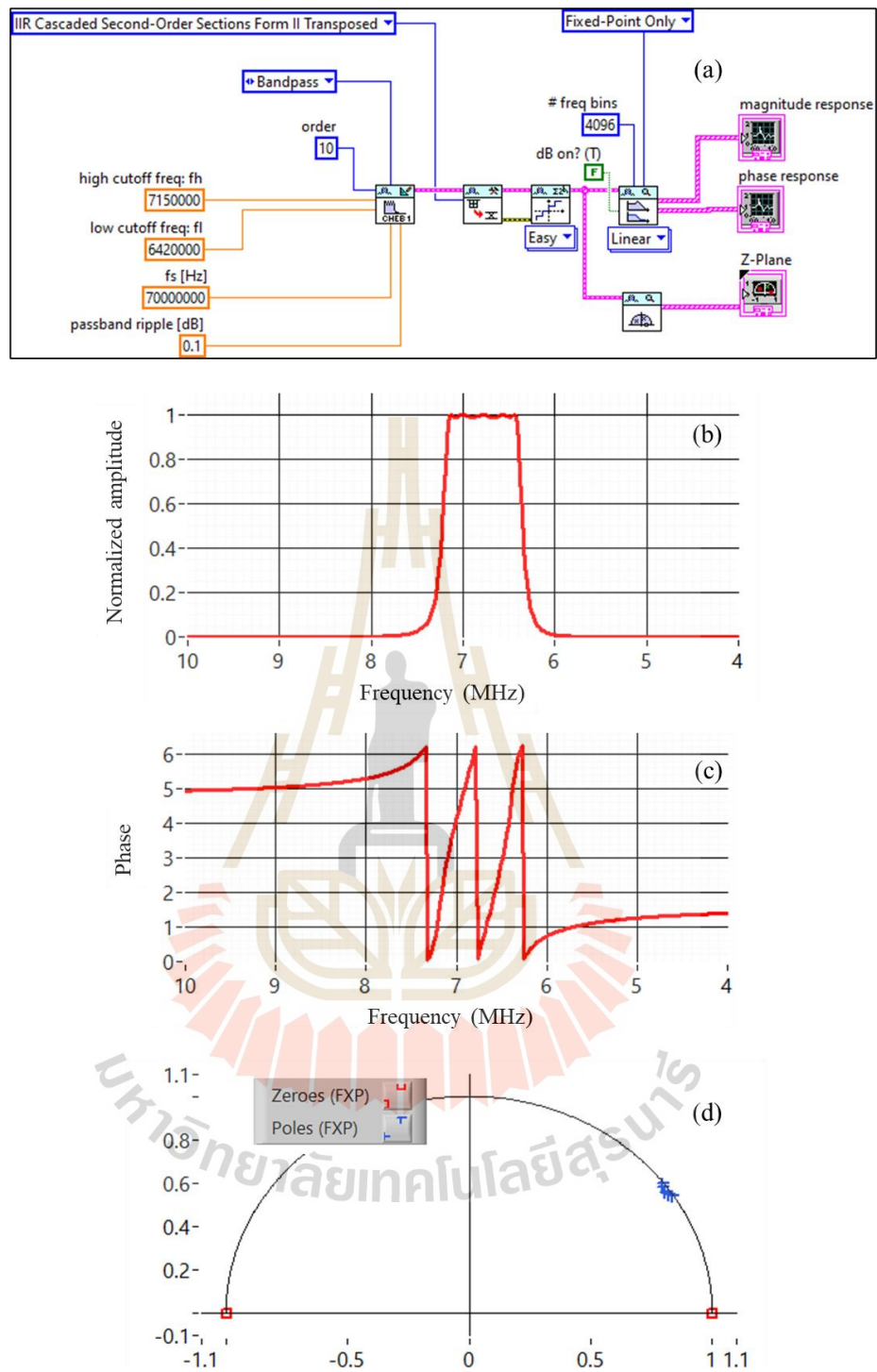


Figure 6.7 (a) is filter programming, (b) is magnitude response, (c) is phase response, and (d) is the z-plane of filter designing for zone 4.

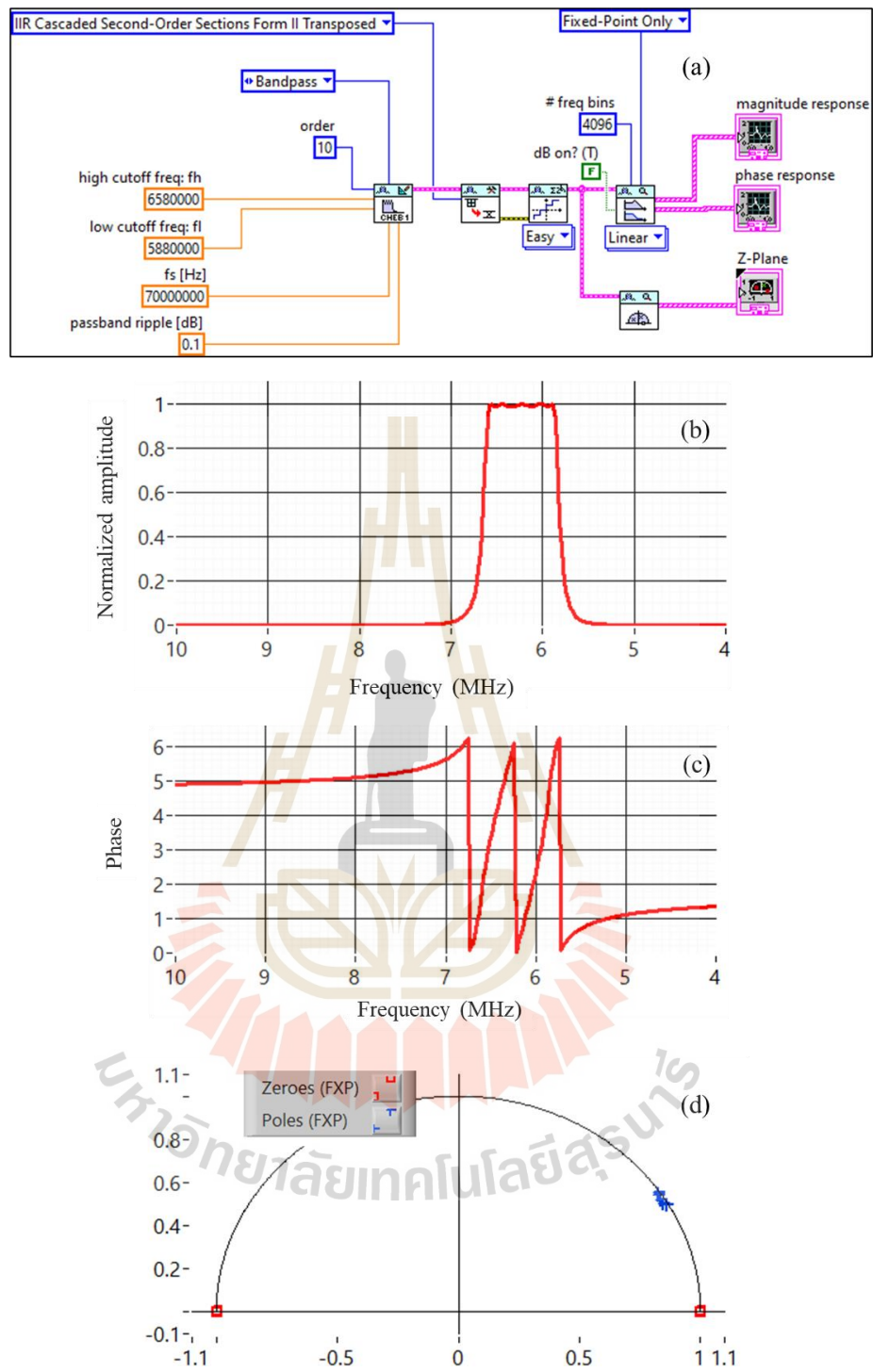


Figure 6.8 (a) is filter programming, (b) is magnitude response, (c) is phase response, and (d) is the z-plane of filter designing for zone 5.

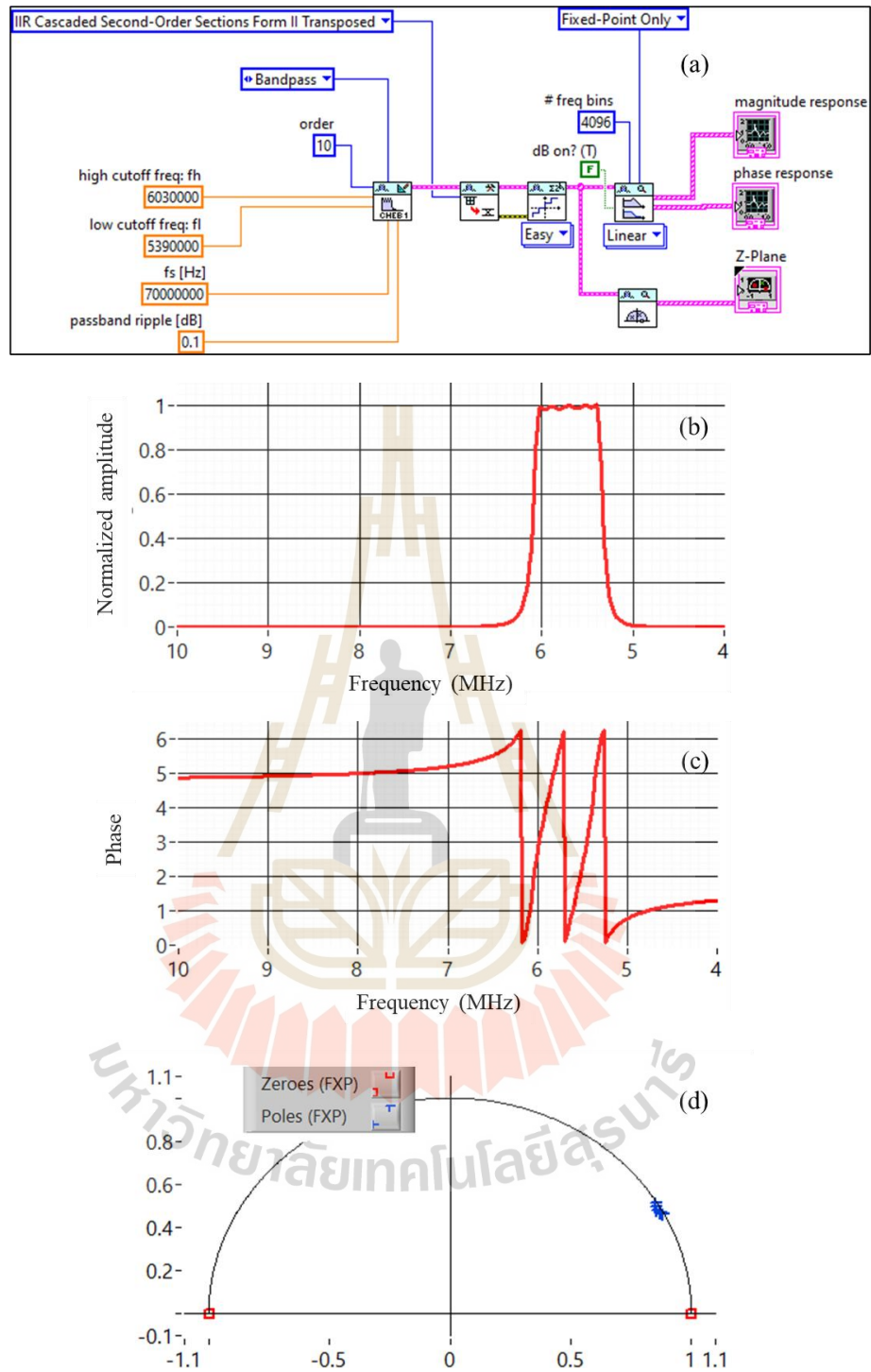


Figure 6.9 (a) is filter programming, (b) is magnitude response, (c) is phase response, and (d) is the z-plane of filter designing for zone 6.

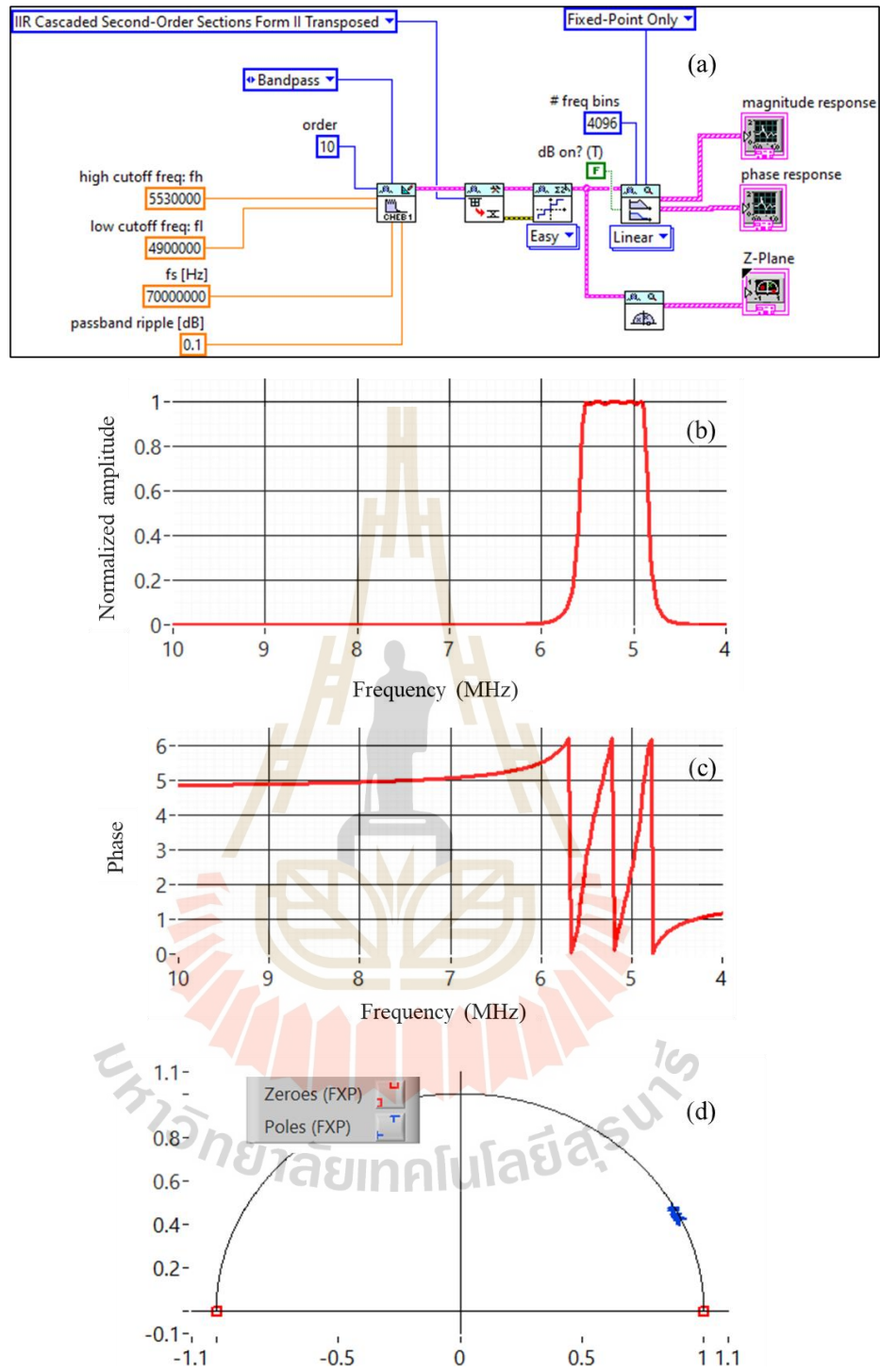
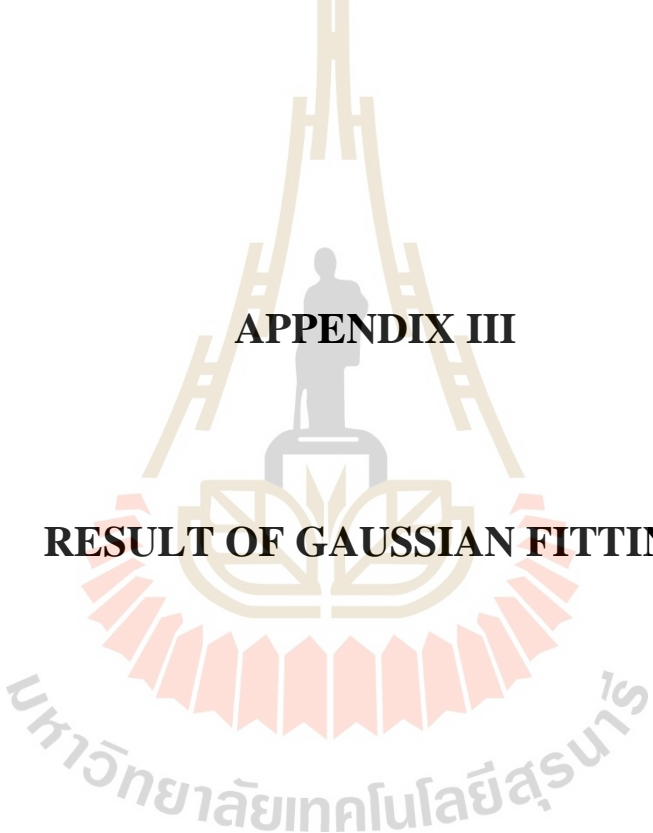


Figure 6.10 (a) is filter programming, (b) is magnitude response, (c) is phase response, and (d) is the z-plane of filter designing for zone 7.



APPENDIX III

RESULT OF GAUSSIAN FITTING

มหาวิทยาลัยเทคโนโลยีสุรนารี

Zone 1

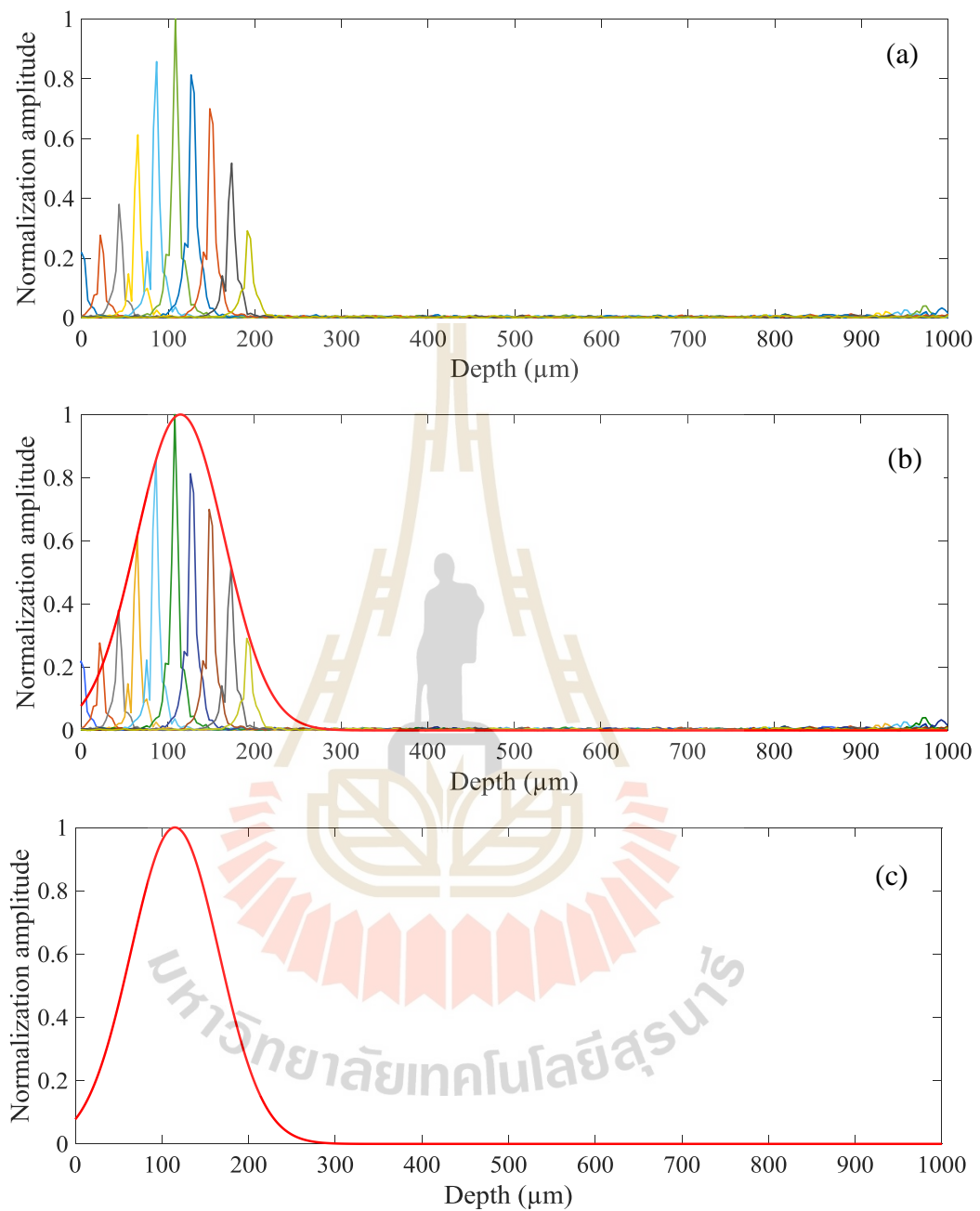


Figure 6.11 (a) Superposition of multiple depth profiles obtained at different positions in the air of the sample in micrometer. (b) Result of Gaussian fitting plotted over (a). (c) Gabor windows at the normal focal plane that corresponding to the center and width of DOF of zone 1.

Zone 2

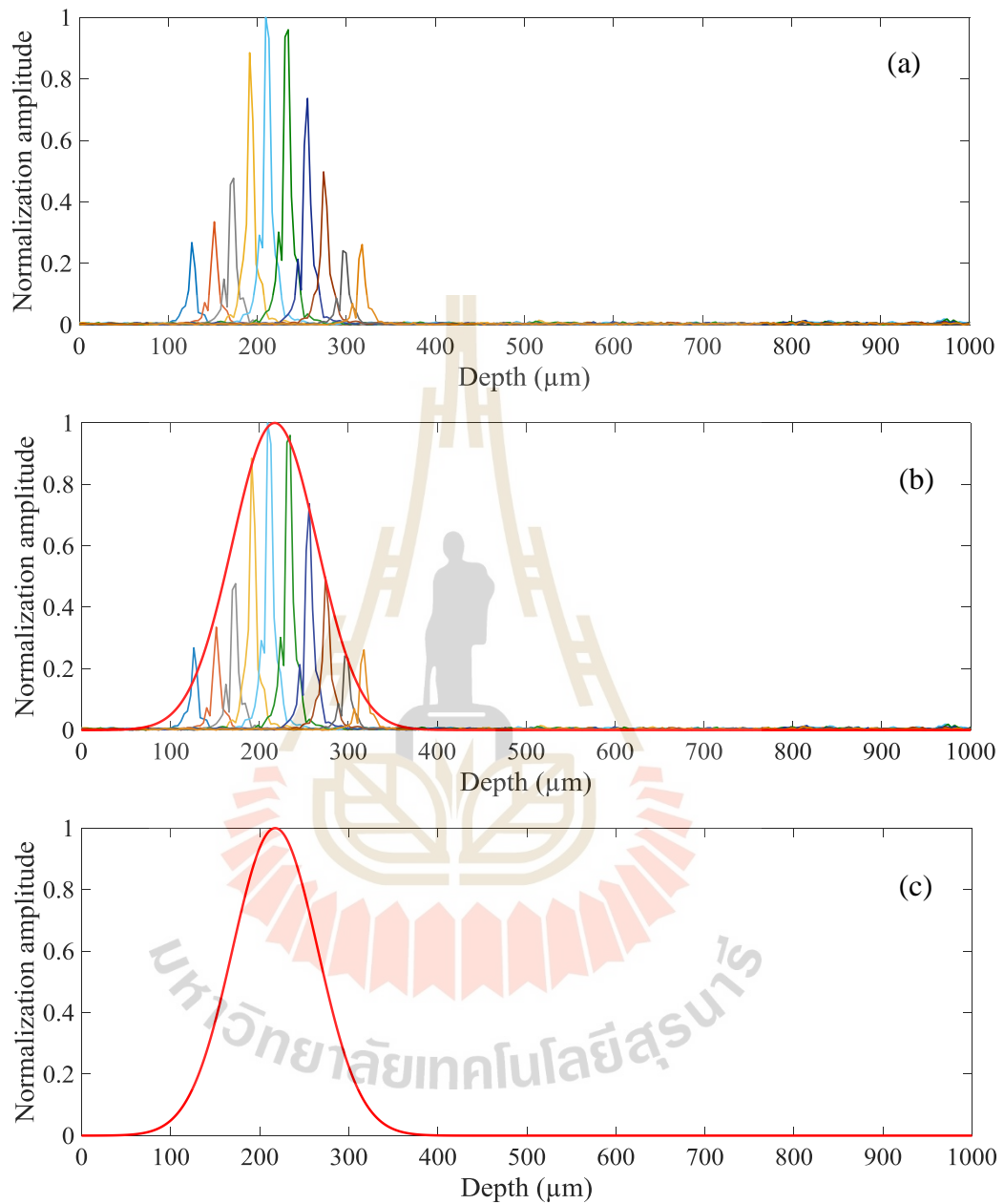


Figure 6.12 (a) Superposition of multiple depth profiles obtained at different positions in the air of the sample in micrometer. (b) Result of Gaussian fitting plotted over (a). (c) Gabor windows at the shifted focal plane that corresponding to the center and width of DOF of zone 2.

Zone 3

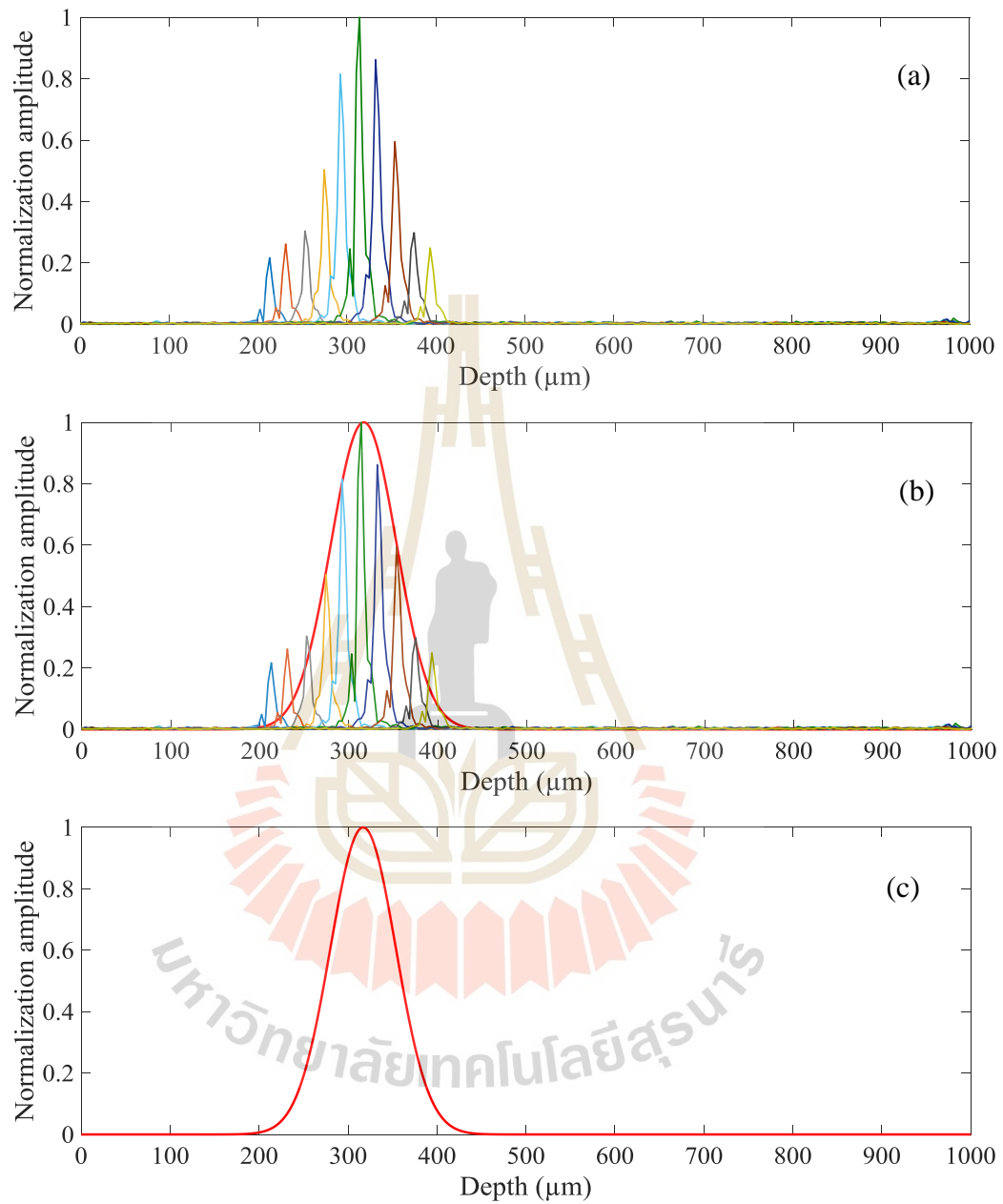


Figure 6.13 (a) Superposition of multiple depth profiles obtained at different positions in the air of the sample in micrometer. (b) Result of Gaussian fitting plotted over (a). (c) Gabor windows at the shifted focal plane that corresponding to the center and width of DOF of zone 3.

Zone 4

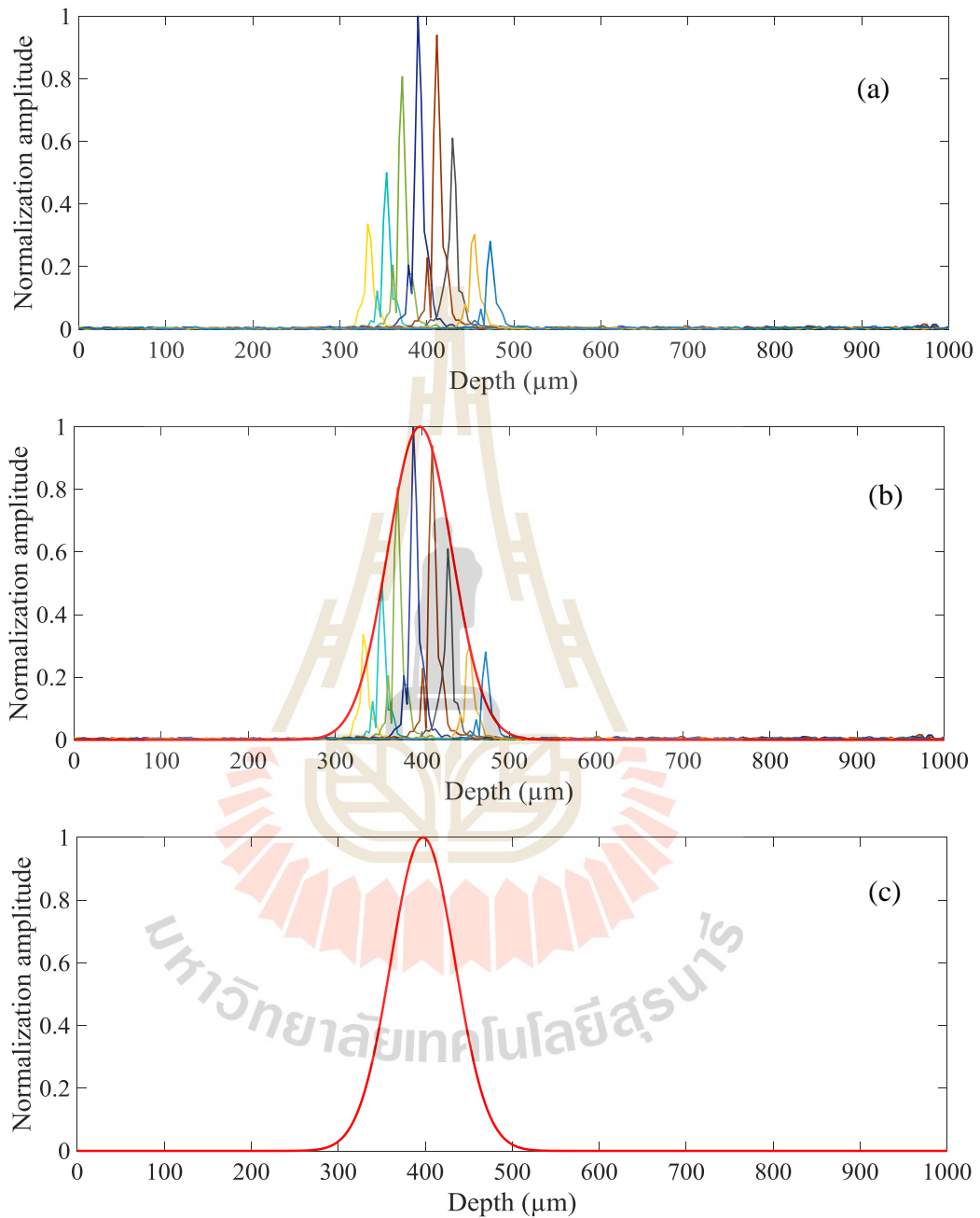


Figure 6.14 (a) Superposition of multiple depth profiles obtained at different positions in the air of the sample in micrometer. (b) Result of Gaussian fitting plotted over (a). (c) Gabor windows at the shifted focal plane that corresponding to the center and width of DOF of zone 4.

Zone 5

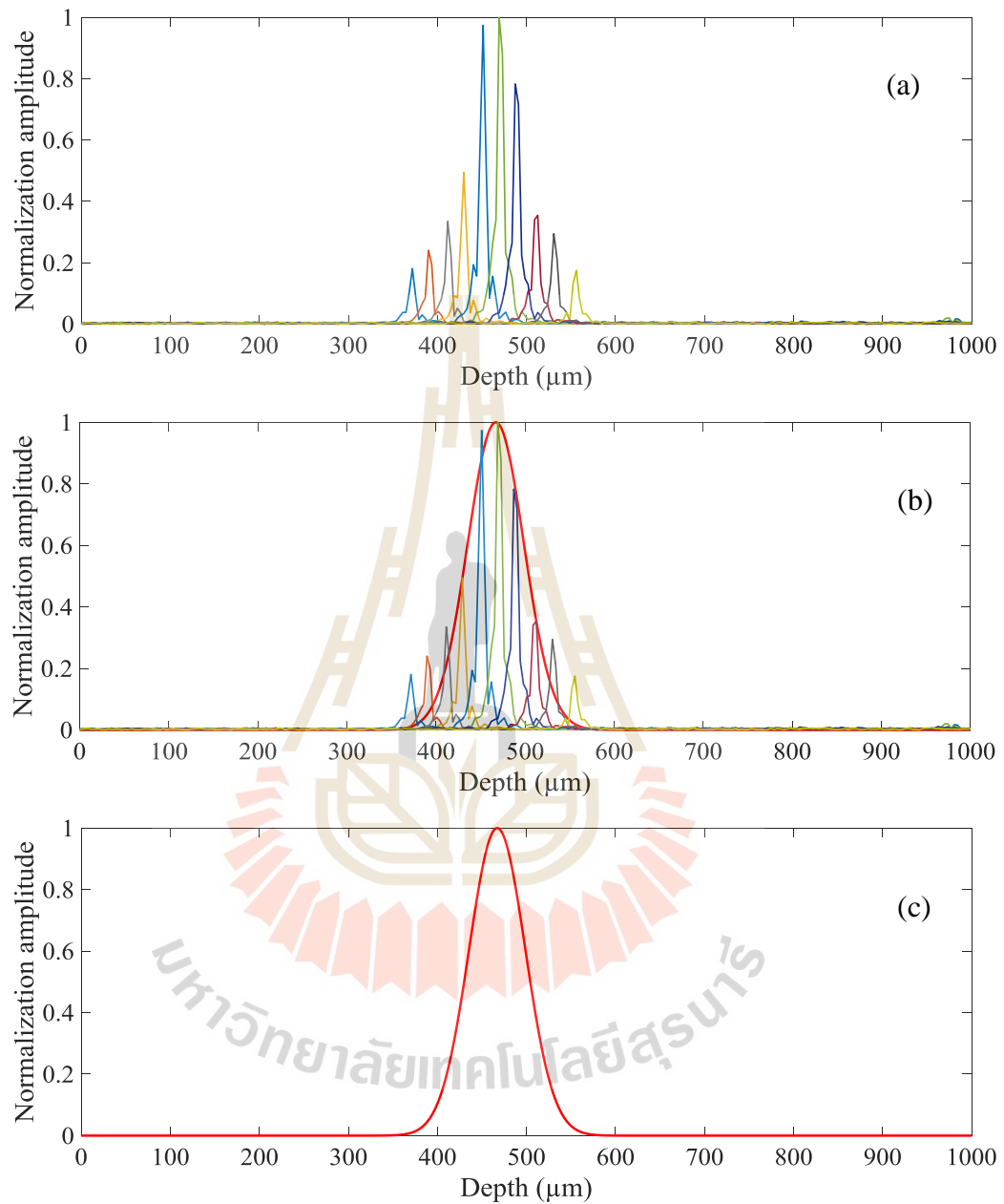


Figure 6.15 (a) Superposition of multiple depth profiles obtained at different positions in the air of the sample in micrometer. (b) Result of Gaussian fitting plotted over (a). (c) Gabor windows at the shifted focal plane that corresponding to the center and width of DOF of zone 5.

Zone 6

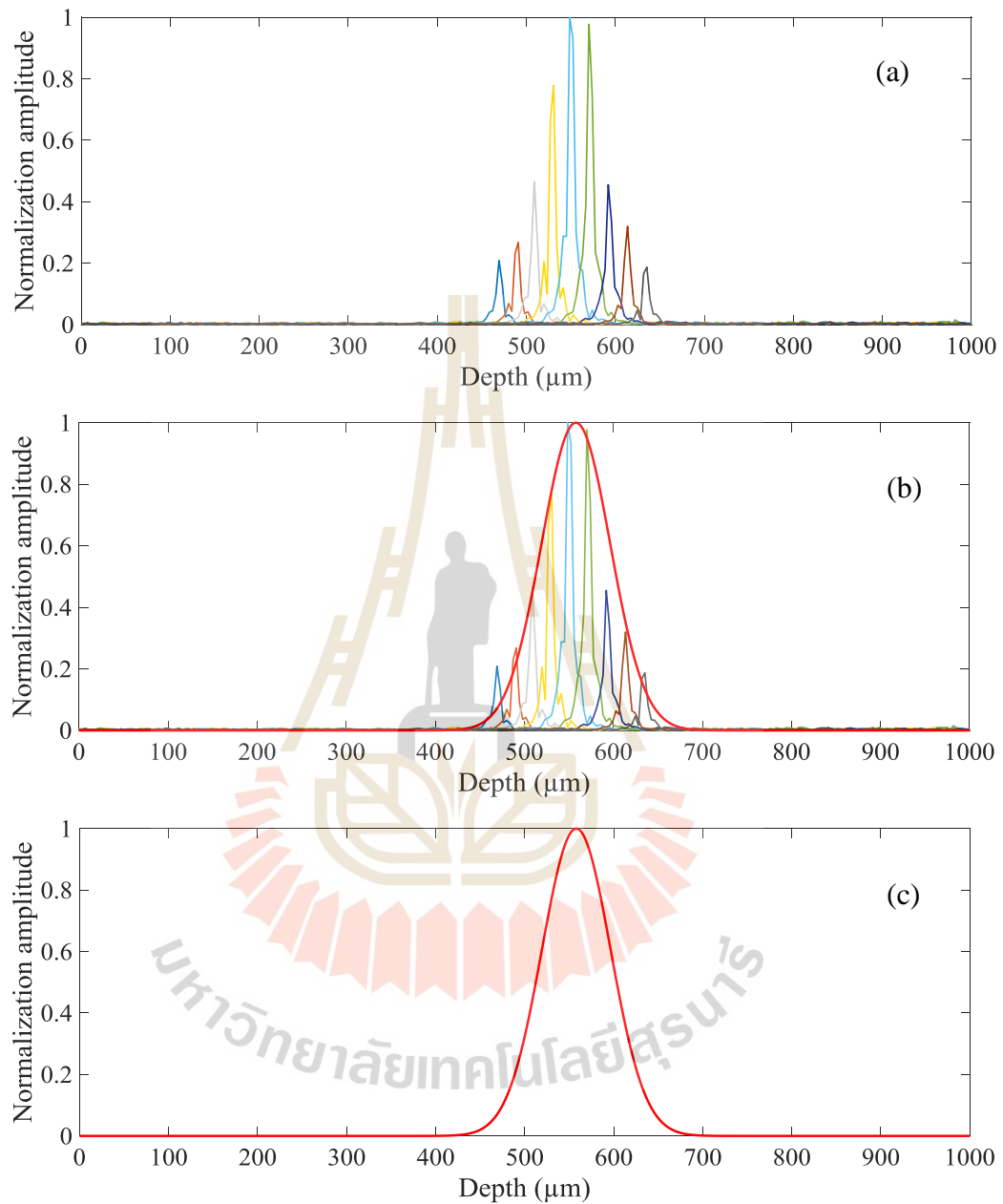


Figure 6.16 (a) Superposition of multiple depth profiles obtained at different positions in the air of the sample in micrometer. (b) Result of Gaussian fitting plotted over (a). (c) Gabor windows at the shifted focal plane that corresponding to the center and width of DOF of zone 6.

Zone 7

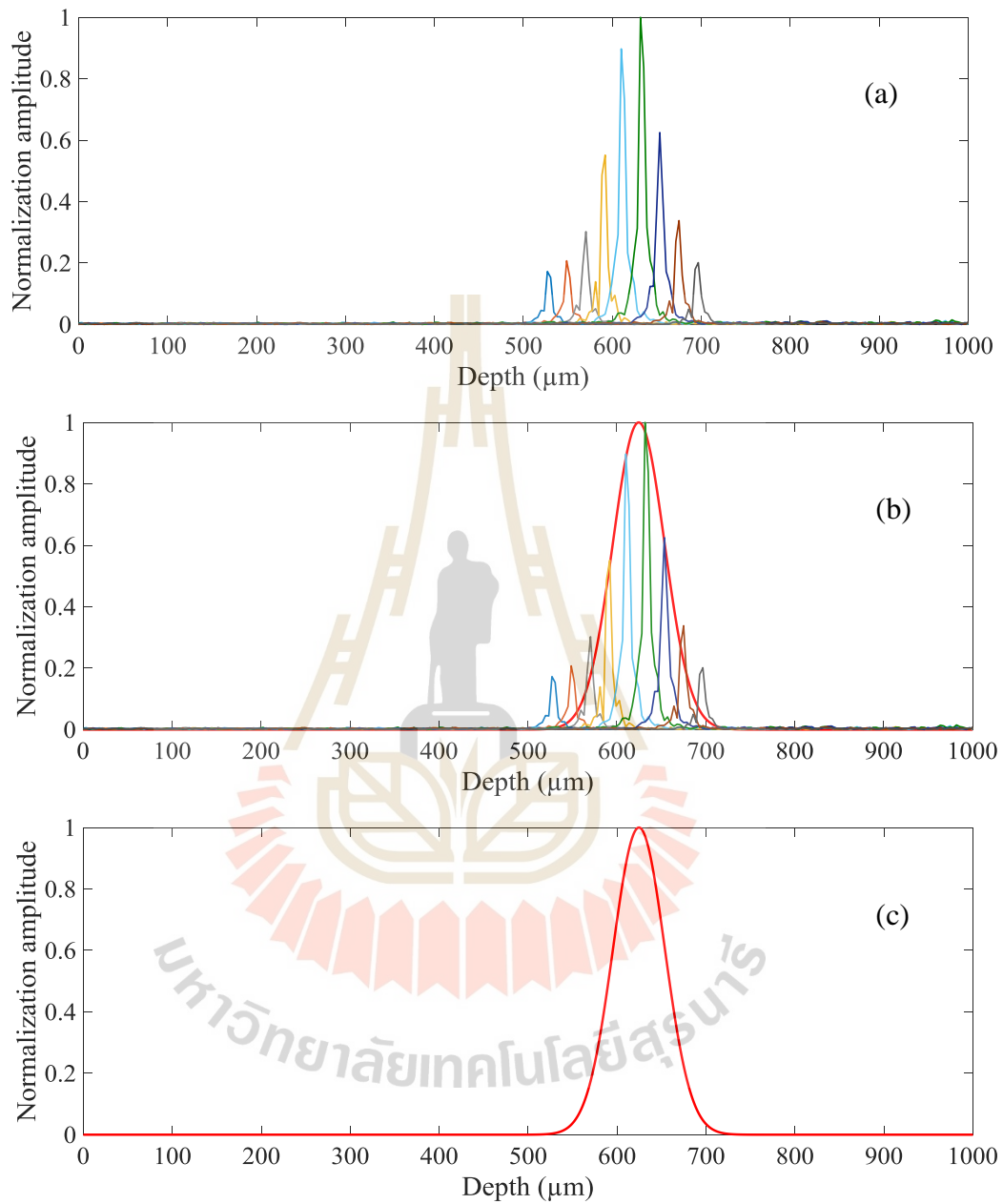


Figure 6.17 (a) Superposition of multiple depth profiles obtained at different positions in the air of the sample in micrometer. (b) Result of Gaussian fitting plotted over (a). (c) Gabor windows at the shifted focal plane that corresponding to the center and width of DOF of zone 7.

Zone 8

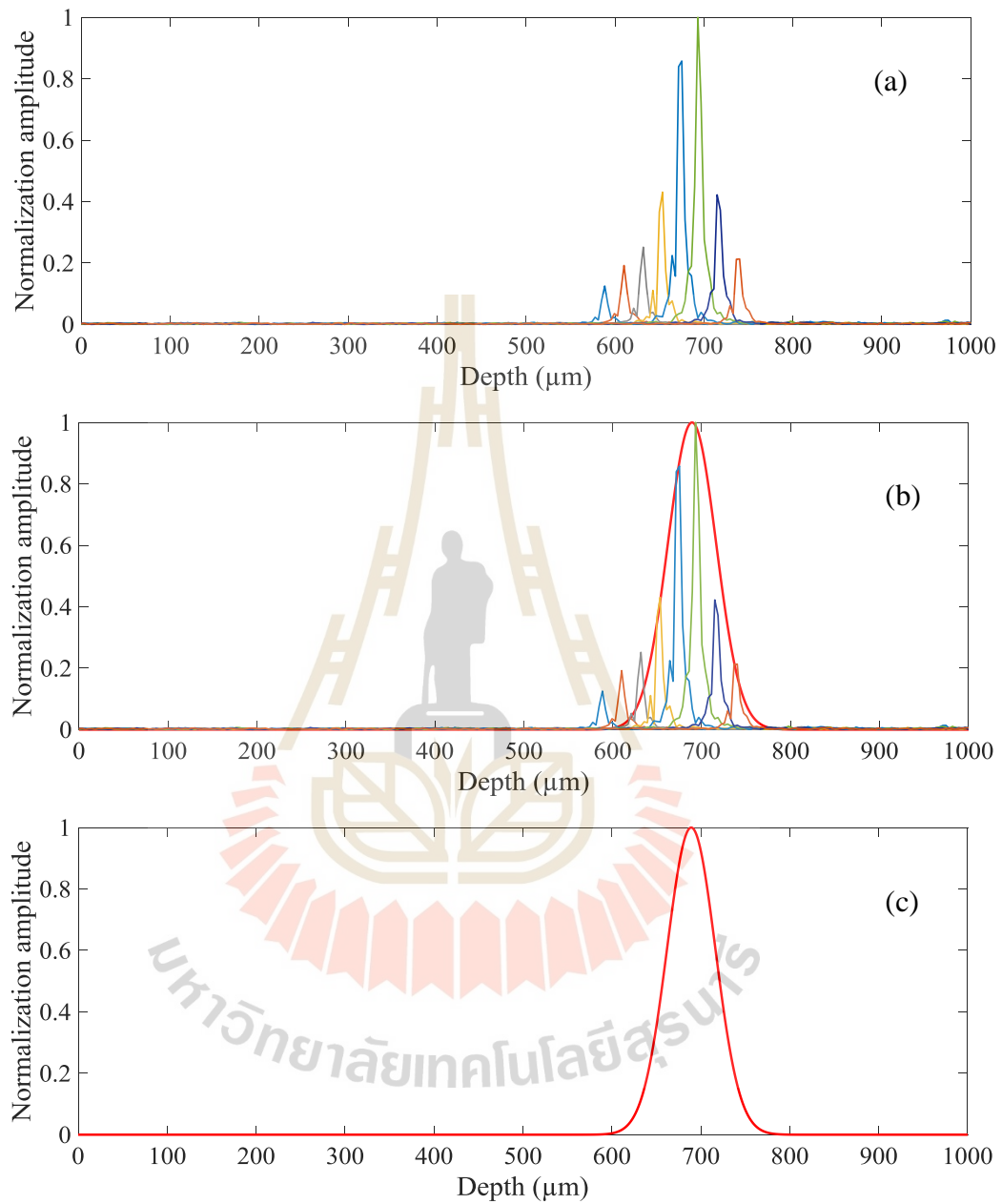


Figure 6.18 (a) Superposition of multiple depth profiles obtained at different positions in the air of the sample in micrometer. (b) Result of Gaussian fitting plotted over (a). (c) Gabor windows at the shifted focal plane that corresponding to the center and width of DOF of zone 8.

Zone 9

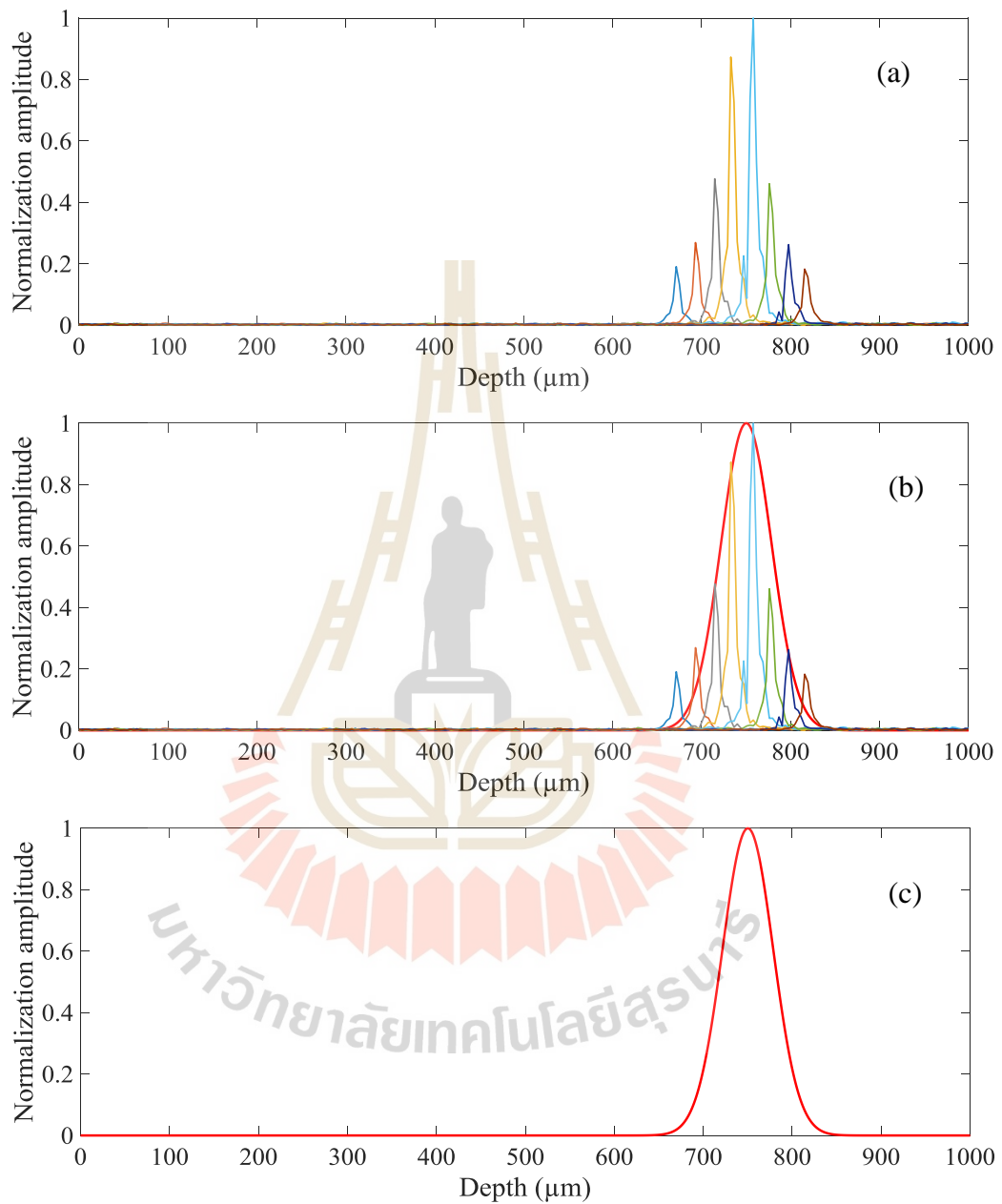


Figure 6.19 (a) Superposition of multiple depth profiles obtained at different positions in the air of the sample in micrometer. (b) Result of Gaussian fitting plotted over (a). (c) Gabor windows at the shifted focal plane that corresponding to the center and width of DOF of zone 9.

Zone 10

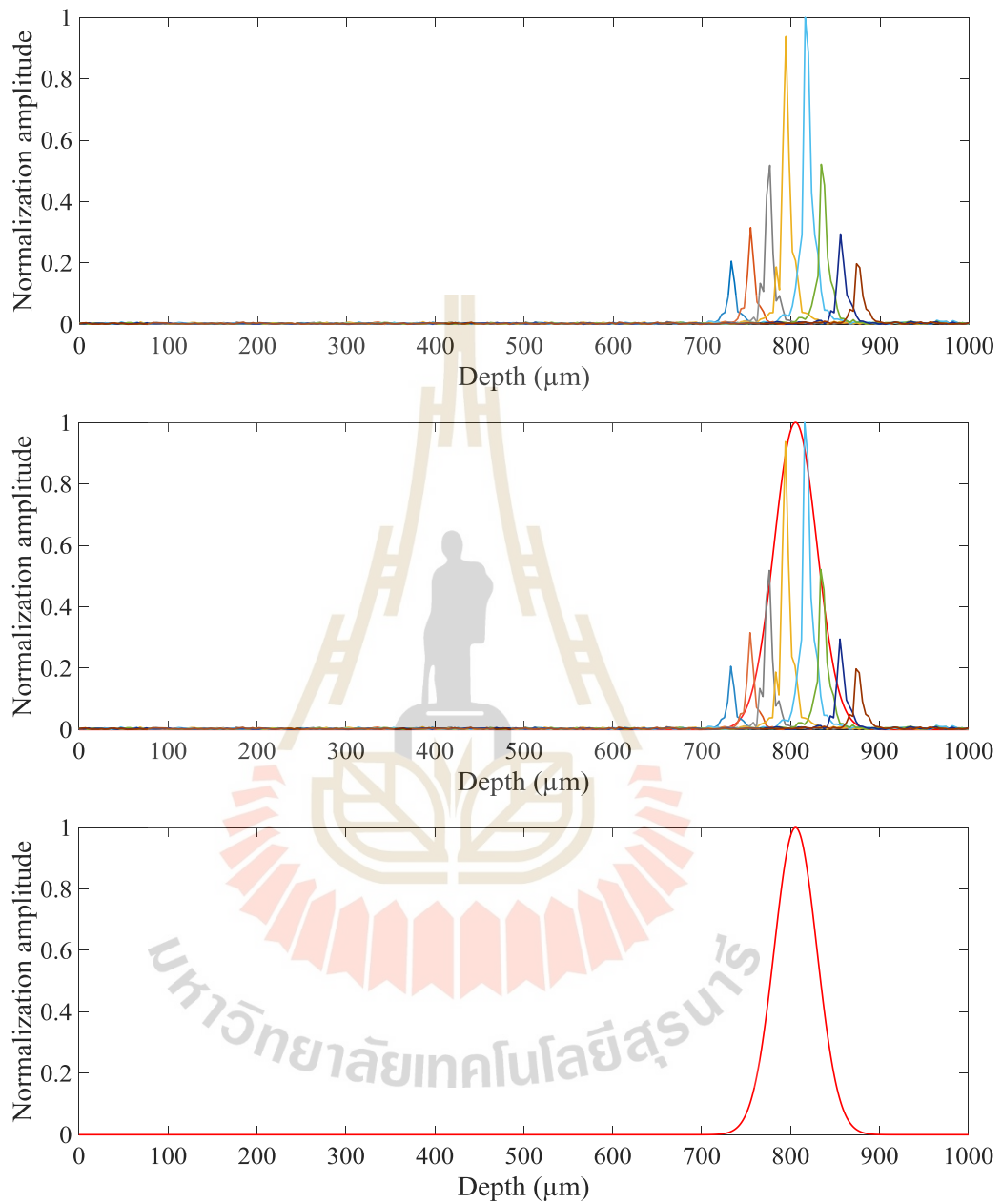


Figure 6.20 (a) Superposition of multiple depth profiles obtained at different positions in the air of the sample in micrometer. (b) Result of Gaussian fitting plotted over (a). (c) Gabor windows at the shifted focal plane that corresponding to the center and width of DOF of zone 10.

Zone 11

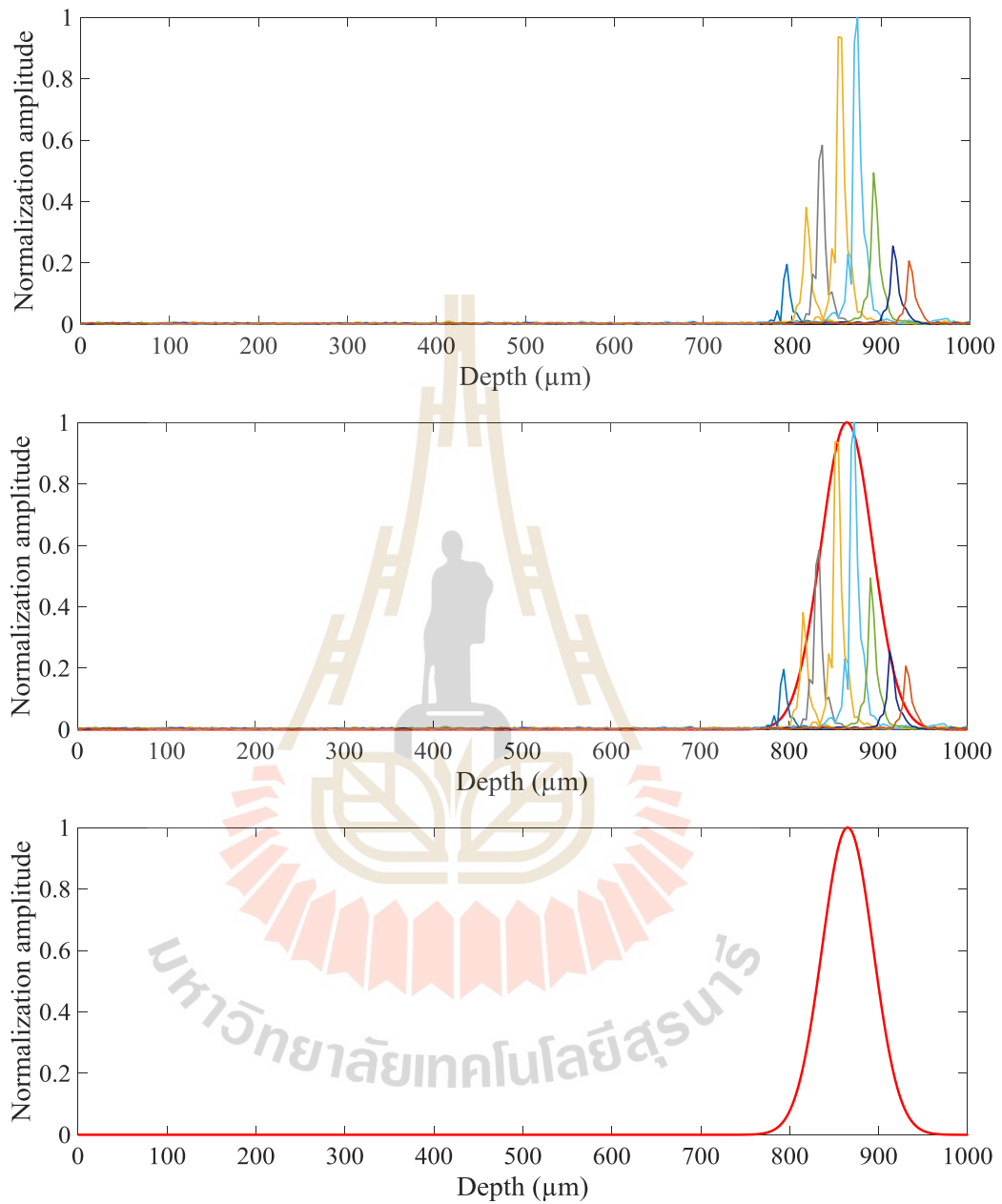


Figure 6.21 (a) Superposition of multiple depth profiles obtained at different positions in the air of the sample in micrometer. (b) Result of Gaussian fitting plotted over (a). (c) Gabor windows at the shifted focal plane that corresponding to the center and width of DOF of zone 11.

Zone 12

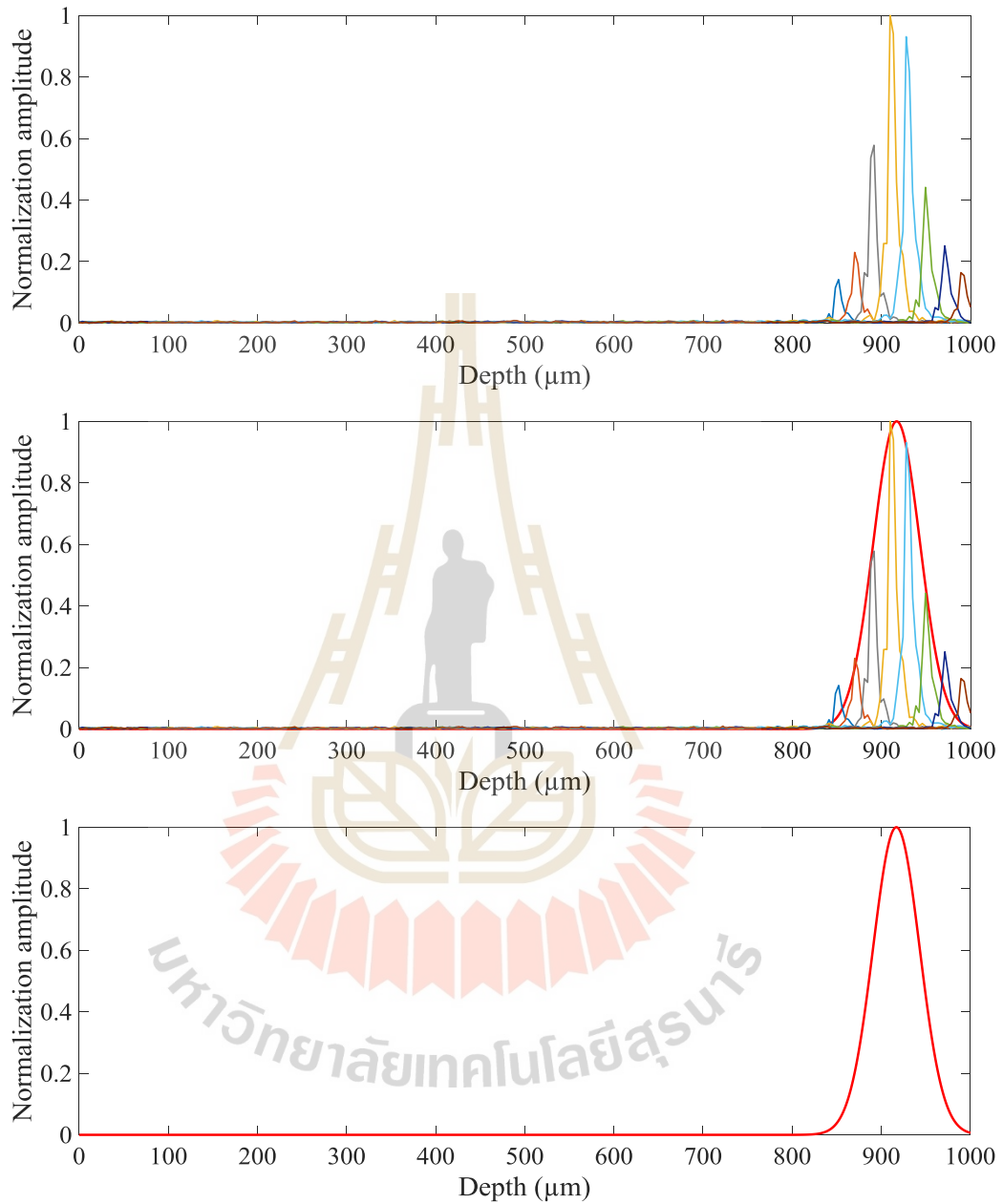


Figure 6.22 (a) Superposition of multiple depth profiles obtained at different positions in the air of the sample in micrometer. (b) Result of Gaussian fitting plotted over (a). (c) Gabor windows at the shifted focal plane that corresponding to the center and width of DOF of zone 12.

Zone 13

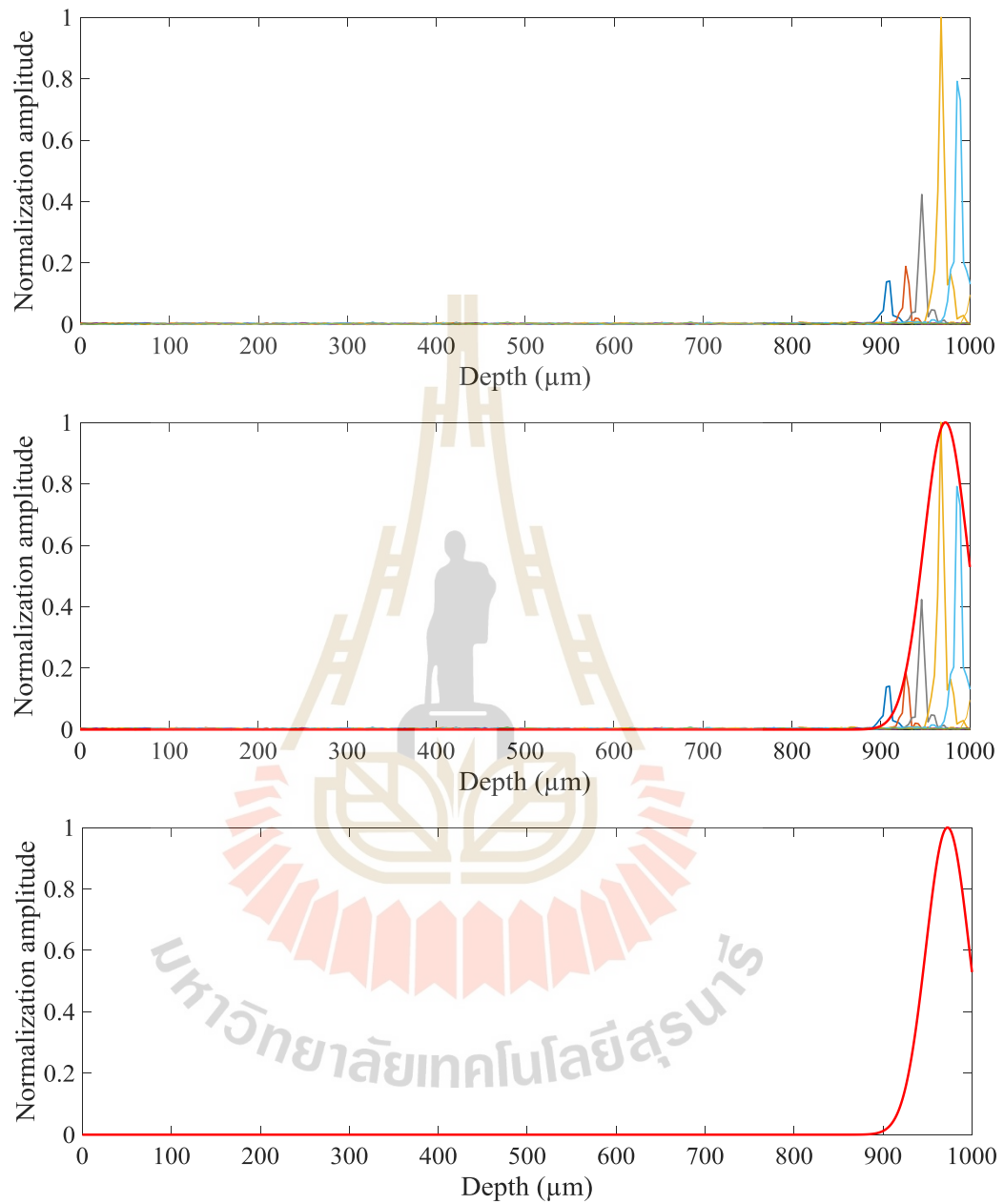


Figure 6.23 (a) Superposition of multiple depth profiles obtained at different positions in the air of the sample in micrometer. (b) Result of Gaussian fitting plotted over (a). (c) Gabor windows at the shifted focal plane that corresponding to the center and width of DOF of zone 13.

BIOGRAPHY

Name Mr. Yutana Lenaphet

Date of Birth 13 August 1991

Place of Birth Nongkhai, Thailand

Education

- 26 December 2013, Bachelor Degree of Electrical Engineering in Engineering, Suranaree university of technology.

Publications

- Meemon, P., Lenaphet, Y., & Widjaja, J. (2021). Spectral fusing Gabor domain optical coherence microscopy based on FPGA processing. *Applied Optics*, 60(7), 2069-2076.
- Lenaphet, Y., and P. Meemon. 2020. "The implementation of digital filter on FPGA for the spectral fusing Gabor domain optical coherence microscopy." In *2020 8th International Electrical Engineering Congress (iEECON)*, 1-4.

Awards

- Panomsak Meemon, Kunakorn Palawong, Jadsada Saetiew, Jiraporn Saenjae, Yutana Lenaphet. Handheld optical coherence tomography. 2nd runner-up Award, Innovation and Technology Exposition 2020.